University of Trento
Department of Physics

Equilibrium and out-of-equilibrium physics of Bose gases at finite temperature

Doctoral Thesis
submitted to the
Doctoral School of Physics – XXXIV Cycle
by

Louise Wolswijk

for the degree of
Doctor of Philosophy – Dottore di Ricerca

Supervisor: Gabriele Ferrari
Co-Supervisor: Giacomo Lamporesi
Referees: Jérôme Beugnon
David Clément

June 2022

Louise Wolswijk

Equilibrium and out-of-equilibrium physics of Bose gases at finite temperature

PH.D. THESIS IN PHYSICS

UNIVERSITY OF TRENTO
June 2022

To science,
To art, music, and dances,
To the mountains and lakes,
To the BEC laboratory,
To my supervisors,
To my friends,
To my delocalized family,
To my love,
To everyone who taught me something
and accompanied me in this journey,
To you, who are reading this.

Contents

Introduction

The physics of ultracold quantum gases has been the subject of a long-lasting and intense research activity, which started almost a century ago with purely theoretical studies, with the prediction in 1924 by Bose and Einstein of the existence of a novel phase of matter, the Bose-Einstein condensate (BEC). The field had a fluorishing experimental development after the implementation of laser and evaporative cooling techniques that led to the first realization of a BEC in 1995 [1, 2].

In recent years, ultracold atoms have acquired an increasing relevance for their use as platforms for quantum technologies, exploiting the macroscopic occupation, in the BEC, of a single quantum state, and taking advantage of the high degree of control that can be achieved, with the possibility of finely tuning most of the parameters that characterize the system. These features make ultracold atoms an ideal platform for the study, in a clean and well controlled environment, of physical phenomena analogous to those occurring in other, more complicated or even inaccessible systems, for instance in the field of condensed matter or high energy physics. This concept is at the heart of quantum simulation.

In the context of quantum technologies, an in-depth understanding of the state of the quantum many-body systems that are involved becomes of fundamental importance. Not only the final equilibrium target state of the system needs to be well known, but also the processes needed to reach such state. These processes often involve the crossing of second order phase transitions, which bring the system strongly out-of-equilibrium, making the control more challenging. It becomes therefore crucial to better understand the out-of-equilibrium dynamics occurring in the vicinity of a phase transition, as well as the relaxation processes taking place during the re-equilibration of the system towards the desired equilibrium condition.

In this thesis I present the results of the research activity that I performed during my PhD at the BEC1 laboratory of the BEC center in Trento, working on ultracold gases of ^{23}Na atoms confined in an elongated harmonic trap. This work was focused on two main goals: the first regarded the study of the thermodynamic properties of an equilibrium Bose gas at finite temperature, while the second was the investigation of the out-of-equilibrium dynamics taking place when a Bose Einstein condensate is prepared by cooling a thermal cloud at finite rate across the BEC phase transition.

The aim of the first project was the experimental determination of the Equation of State (EoS) describing the thermodynamic behavior of the weakly interacting uniform Bose gas at finite temperature. A measurement of such an EoS was obtained already in the grand canonical formulation [3], but not yet in the canonical formulation, where the pressure is expressed in terms of the volume and temperature $p(v, T)$. We also aimed at investigating the behavior of the chemical potential as a function of temperature, in the vicinity of the critical point. Here a peak in the chemical potential is predicted to be present as a consequence of superfluidity, but was not yet observed in the Bose gas.

From the density distribution of an atomic cloud, confined in an external potential, it is possible to extract the EoS of the corresponding uniform system using the Local Density Approximation (LDA), which consists in treating the confined system as a series of locally homogeneous samples in thermodynamic equilibrium. Applying this idea to a partially condensed Bose gas, confined in a harmonic trap, one can determine the thermodynamic behavior across the critical point. It becomes therefore crucial to accurately measure the *in situ* density profile of the trapped cloud. In a partially condensed cloud it is particularly challenging to resolve with enough detail the region at the boundary between the BEC and the thermal cloud, where the atomic density rapidly drops in a narrow spatial region.

This motivated an upgrade of the experimental setup, with the implementation of a higher resolution imaging system and a partial rebuilding of the experimental setup used for cooling the atoms. This created the occasion for an optimization of the whole apparatus in order to obtain more stable working conditions. Concurrently I also realized and included in the experiment an optical setup for the use of a Digital Micromirror Device (DMD) to project time-dependent arbitrary light patterns on the atoms, creating optical potentials that can be controlled at will. The use of this device opens up exciting future perspectives, offering the possibility, for instance, to rapidly modify the trapping potential in a well controlled way, independently in different parts of the gas, or to create repulsive obstacles moving through the atomic cloud at tunable velocities.

Regarding again the measurement of the EoS, another challenge in imaging the *in situ* density distribution is determined by the fact that the optical density (OD) in the center of the BEC exceeds by several orders of magnitude the low OD in the thermal tails, requiring the use of an *ad-hoc* measuring method. Combining the principles of partial transfer imaging (PTAI) and of high-dynamic range (HDR) photography, we developed a method [4] to accurately measure optical densities in a high dynamic range, obtaining a reliable estimation of the optical density of the whole atomic cloud. From the measured optical density we extracted, by means of the inverse Abel transform, the 3D density profile, as well as the pressure, exploiting the LDA and general thermodynamic relations. Together with an independent measurement of the temperature, this allowed us to obtain the equation of state of the Bose gas in the canonical formulation $p(v, T)$. We found an excellent agreement between the experimental data and the Hartree-Fock model [5], which highlights the importance of interactions in the thermodynamic behavior of the gas. We were also able to observe, for the first time in a Bose gas, the presence of a peak in the chemical potential at the critical temperature T_c.

The second part of this thesis work is devoted to the study of the dynamical processes that occur during the formation of the BEC order parameter within a thermal cloud. The cooling at finite rate across the Bose-Einstein condensation transition brings the system in a strongly out-of-equilibrium state, which is worth investigating, together with the subsequent relaxation towards an equilibrium state. This is of interest also in view of achieving a better understanding of second order phase transitions in general, since such phenomena are ubiquitous in nature and relevant also in other platforms for quantum technologies.

A milestone result in the study of second order phase transitions is given by the Kibble-Zurek mechanism [6, 7], which provides a simple model capturing important aspects of the evolution of a system that crosses a second-order phase transition at finite rate. It is based on the principle that in an extended system the symmetry breaking associated with a continuous phase transition can take place only locally. This causes the formation of causally disconnected domains of the order parameter, at the boundaries of which topological defects can form, whose number and size scale with the rate at which the transition is crossed, following a universal power law. It was originally developed in the context of cosmology, but was later successfully tested in a variety of systems, including superfluid helium [8], superconductors [9, 10] and trapped ions [11, 12].

The BEC phase transition represents in this context a paradigmatic test-bench, given the high degree of control at which this second-order phase transition can be crossed by means of cooling ramps at different rates. Already early experiments investigated the formation of the BEC order parameter within a thermal cloud after quasi-instantaneous temperature quenches or very slow evaporative cooling [13, 14, 15]. In the framework of directly testing the Kibble-Zurek mechanism, further experiments were performed, both in 2D and 3D systems, focusing on the emergence of coherence and on the statistics of the spontaneously generated topological defects as a function of the cooling rate [16, 17, 18, 16, 19, 20, 21].

The Kibble-Zurek mechanism, however, does not fully describe the out-of-equilibrium dynamics of the system at the transition, nor the post-quench interaction mechanisms between domains that lead to coarse-graining. Most theoretical models are based on a direct linear variation of a single control parameter, e.g. the temperature, across the transition. In real experiments, the cooling process is controlled by the tuning of other experimental parameters and a global temperature might not even be well defined, in a thermodynamic sense, during the whole process. Moreover, the temperature variation is usually accompanied by the variation of other quantities, such as the number of atoms and the collisional rate, making it difficult to accurately describe the system and predict the post-quench properties. Recent works included effects going beyond the Kibble-Zurek mechanism, such as the inhomogeneity introduced by the trapping potential, the role of atom number losses [22, 23] and the saturation of the number of defects for high cooling rates[24, 25, 26]. Such works motivate further studies, in particular of the dynamics taking place at early times, close to the crossing of the critical point.

The aim of the work presented in this thesis is to further investigate the timescales associated to the formation and evolution of the BEC order parameter and its spatial fluctuations, as a function of the rate at which the transition point is crossed. We performed experiments producing BECs by means of standard cooling protocols, involving evaporative cooling in a magnetic trap. We explored a wide range of cooling rates across the transition and found a universal scaling for the growth of the BEC order parameter with the cooling rate and a finite delay in its formation, which was already observed in earlier works [14, 13]. The evolution of the fluctuations of the order parameter was also investigated, with an analysis of the timescale of their decay during the relaxation of the system, from an initial strongly out-of-equilibrium condition to a final equilibrium state.

This thesis is structured as follows:

- The first chapter presents the theoretical background, starting with a brief introduction to the concept of Bose Einstein condensation and a presentation of different models describing the thermodynamics of an equilibrium Bose gas. The second part of this chapter then deals with the out-of-equilibrium dynamics that is inevitably

involved in the crossing of a second-order phase transition such as the one for Bose-Einstein condensation. The Kibble-Zurek mechanism is briefly reviewed and beyond KZ effects are pointed out, motivating a more detailed investigation of the timescales involved in the BEC formation.
- In the second chapter, I describe the experimental apparatus that we use to cool and confine the atoms. Particular detail is dedicated to the parts that have been upgraded during my PhD, such as the imaging system.
- In the third chapter I show our experimental results on the measurement of the equation of state of the weakly interacting uniform Bose gas at finite temperature.
- In the fourth chapter I present our results on the out-of-equilibrium dynamics in the formation of the condensate order parameter and its spatial fluctuations, as a function of different cooling rates.

The main experimental results presented in this thesis are published in Refs. [4, 5, 27].

Chapter 1

Theoretical background

1.1 Ultracold Bose gas in thermal equilibrium

Bose-Einstein condensation can be considered as the transition from a classical to a quantum regime for a gas of bosons, i.e., indistinguishable atoms of integer spin obeying Bose-Einstein statistics. In this quantum regime, that is achieved in conditions of very low temperature, the particles macroscopically occupy a single quantum state, the Bose-Einstein condensate (BEC) state and the system presents long-range order. In the following, I first introduce the concept of Bose-Einstein condensation in the simplified case of a non-interacting uniform Bose gas. I then consider the case of a weakly interacting Bose gas at zero temperature, in the presence of a trapping potential, described by the Gross-Pitaevskii equation. Then I move on to the Hartree-Fock formalism, which provides a theoretical description for interacting Bose gases at finite temperature. In particular, the relations describing the thermodynamic behavior of the uniform Bose gas are derived, both in the ideal and in the interacting case. Then I introduce the local-density approximation (LDA), that allows, under certain conditions, to treat an inhomogeneous system as locally uniform. Finally, the effect of interactions on the critical temperature for Bose-Einstein condensation is considered.

1.1.1 Ideal Bose gas

Uniform Ideal Bose gas

To introduce the concept of Bose-Einstein condensation, I first present the simplified picture of the Ideal Bose Gas (IBG): a dilute gas of non-interacting bosons is considered, in a box of volume V, in the absence of external potentials. Figure 1.1, from Ketterle's popular paper [28], gives an intuitive view of the phenomenon of Bose-Einstein condensation. Each particle can be viewed as a quantum wave packet with a characteristic extent of the order of the thermal de Broglie wavelength, which is defined as:

$$\lambda_T = \sqrt{\frac{2\pi\hbar^2}{mk_BT}} \tag{1.1}$$

where T is the gas temperature, m the atomic mass, k_B the Boltzmann's constant and $\hbar$ the reduced Planck constant. At high temperatures, λ_T is small with respect to the average interatomic distances ($d \sim 1/n^{1/3}$, where n is the atomic density), and the particles behave like classical objects (“billiard-balls”) moving around independently. Decreasing the temperature, λ_T increases and the quantum nature of the atoms starts to become important. When λ_T becomes of the order of the interatomic distance d, the Bose-Einstein condensation transition occurs, with the accumulation of a macroscopic number of particles in the same coherent quantum state at lowest energy.

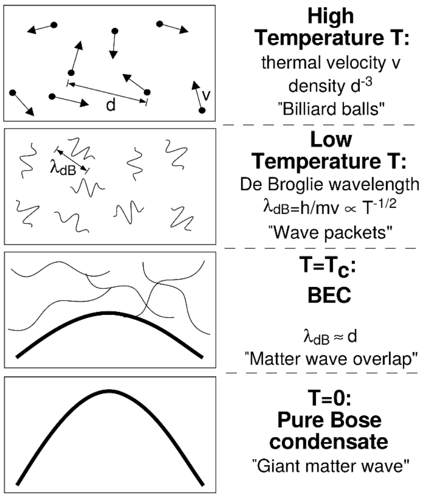

Figure 1.1: Cartoon sketch of the phenomenon of Bose-Einstein condensation, from [28].

Bose-Einstein condensation occurs when the quantity $n\lambda_T^3$, often referred to as Phase-Space Density (PSD), becomes of the order on unity. For the IBG, the condition for Bose-Einstein condensation is given by [29]:

$$n\lambda_T^3 = g_{3/2}(1), \tag{1.2}$$

where $g_{3/2}(z)$ is defined as[1]:

$$g_{3/2}(z) = \frac{2}{\sqrt{\pi}} \int_0^\infty x^{1/2} \frac{1}{z^{-1}e^x - 1} dx, \tag{1.4}$$

and $g_{3/2}(z = 1) = \zeta(3/2) = 2.612$. The condition of Eq. 1.2 corresponds to a critical temperature:

$$T_c = \frac{2\pi\hbar^2}{k_B m} \left(\frac{n}{g_{3/2}(1)} \right)^{2/3} . \tag{1.5}$$

For temperatures $T > T_c$, the gas is fully thermal and has a negative chemical potential μ, following the relation:

$$g_{3/2}\left(e^{\beta\mu}\right) = n\lambda_T \tag{1.6}$$

---

[1] $g_{3/2}(z)$ is a special case of the more general class of Bose functions:

$$g_p(z) = \frac{1}{\Gamma(p)} \int_0^\infty x^{p-1} \frac{1}{z^{-1}e^x - 1} dx = \sum_{l=1}^{\infty} \frac{z^l}{l^p}, \tag{1.3}$$

where $z = \exp(\beta\mu)$ is the so-called fugacity (with μ the chemical potential and $\beta = 1/k_B$) and $\Gamma(p)$ is the factorial function $(p-1)!$. The Bose function evaluated in $\zeta = 1$ coincides with the Riemann function: $\zeta(n) = g_n(1)$.

For $T < T_c$, in the IBG, the chemical potential is, instead, $\mu = 0$ and a finite fraction of the total number of atoms N is in the condensate, while the rest in the thermal component. In particular, the number of atoms in the thermal part is given by:

$$N_T(T) = \frac{V}{\lambda_T} g_{3/2}(1) = N \left(\frac{T}{T_c}\right)^{3/2} \tag{1.7}$$

while the number of atoms in the condensate is:

$$N_0(T) = N \left[1 - \left(\frac{T}{T_c}\right)^{3/2}\right]. \tag{1.8}$$

As the temperature approaches zero, the number of atoms in the thermal part becomes negligible. Equations 1.7, 1.8 reflect the saturation property of the Bose-Einstein condensed gas: if more particles are added to the system, keeping the temperature constant, there will be an increase of N_0, but not of N_T. Fig. 1.2 shows (in blue) the condensate fraction N_0/N as a function of the reduced temperature T/T_c for a uniform ideal Bose gas.

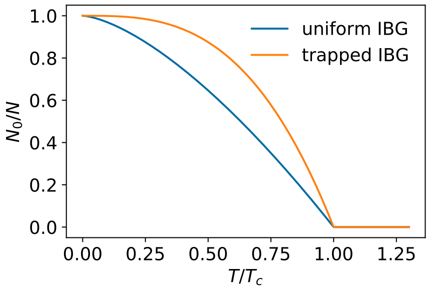

Figure 1.2: Condensate fraction as a function of the reduced temperature in the uniform IBG (blue), according to equation Eq. 1.2, and in the trapped IBG (orange), see Eq. 1.13.

Trapped Ideal Bose gas

The above holds for the uniform non interacting Bose gas. Below, I report also the equations valid for a dilute, non-interacting Bose gas, confined in a harmonic external potential V_{ext}, which is the most common scenario in experiments. For a derivation see [29]. The external potential can, in general, be written as:

$$V_{ext}(x, y, z) = \frac{1}{2} m(\omega_x^2 x^2 + \omega_y^2 y^2 + \omega_z^2 z^2), \tag{1.9}$$

where $\omega_{x,y,z}/(2\pi)$ are the so-called *trapping frequencies*, which determine the size of the atomic cloud along the three orthogonal directions x, y, z:

$$a_{ho,i} = \sqrt{\frac{\hbar}{m\omega_i}}, \text{ for } i = x, y, z. \tag{1.10}$$

The system's characteristic lengthscale is the harmonic oscillator length:

$$a_{ho} = \sqrt{\frac{\hbar}{m\omega_{ho}}}, \tag{1.11}$$

determined by the geometric average of the trapping frequencies $\omega_{ho} = (\omega_x \omega_y \omega_z)^{1/3}$.

For an ideal Bose gas confined in such a potential, the critical temperature is given by:

$$T_c^0 = \frac{\hbar\omega_{ho}}{k_B}\left(\frac{N}{\zeta(3)}\right)^{1/3}. \tag{1.12}$$

The condensate fraction N_0/N as a function of T/T_c is instead:

$$\frac{N_0}{N} = 1 - \left(\frac{T}{T_c^0}\right)^3. \tag{1.13}$$

It is worth noticing the different exponent with respect to the uniform case (Eq. 1.5), as highlighted in Fig. 1.2.

1.1.2 Gross-Pitaevskii equation: trapped interacting Bose gas at $T = 0$

To obtain a more realistic description of an interacting Bose gas confined in an external potential, one has to go beyond the IBG model. At zero temperature, the physics of a condensate of interacting particles in an external potential V_{ext} is well described by the Gross-Pitaevskii equation (GPE), which was independently derived by L. P. Pitaevskii [30] and E. P. Gross [31] in 1961, providing a generalization of Bogoliubov's theory to nonuniform systems [29].

The Hamiltonian $\hat{H}$ for a dilute system of weakly interacting bosonic particles of mass m in an external potential V_{ext}, can be written in second quantization as:

$$\hat{H} = \int \left[\hat{\Psi}^\dagger \left(-\frac{\hbar^2\nabla^2}{2m} + V_{ext}\right)\hat{\Psi} + \frac{g}{2}\hat{\Psi}^\dagger\hat{\Psi}^\dagger\hat{\Psi}\hat{\Psi}\right] d^3r. \tag{1.14}$$

We consider only two-body interactions between the particles and express their strength via the coupling constant g, which at low temperature is determined by the *s-wave* scattering length a via:

$$g = \frac{4\pi\hbar^2}{m}a. \tag{1.15}$$

The interaction term in Eq. 1.14 can be written in this simple form only when the diluteness condition $na^3 \ll 1$ is satisfied, being n the atomic density.
At $T = 0$, the condensate state is macroscopically occupied. This allows to replace the quantum field operator $\hat{\Psi}(\vec{r}, t)$, describing the particle distribution, with a classical complex function, the condensate wave function $\Psi(\vec{r}, t) = |\Psi(\vec{r}, t)|e^{i\varphi(\vec{r},t)}$, the modulus of which is determined by the local density $|\Psi(\vec{r}, t)|^2 = n(\vec{r}, t)$, while the phase factor φ has a crucial role in the coherence and long-range order properties of the BEC. These assumptions lead to the GPE:

$$i\hbar\frac{\partial}{\partial t}\Psi(\vec{r}, t) = \left(-\frac{\hbar^2\nabla^2}{2m} + V_{ext}(\vec{r}, t) + g|\Psi(\vec{r}, t)|^2\right)\Psi(\vec{r}, t). \tag{1.16}$$

This equation is the main theoretical tool to investigate nonuniform Bose gases at low temperature in the mean-field (MF) formalism.

The ground-state of the condensate can be obtained as the lowest-energy stationary solution of the GPE. Writing the condensate wavefunction as $\Psi(\vec{r},t) = \phi(\vec{r})e^{-i\mu t/\hbar}$ and substituting this expression in Eq. 1.16, one obtains the stationary GP equation:

$$\mu\phi(\vec{r}) = \left(-\frac{\hbar^2\nabla^2}{2m} + V_{ext}(\vec{r}) + g\phi^2(\vec{r})\right)\phi(\vec{r}), \tag{1.17}$$

where μ is the chemical potential of the many-body system, related to the number of atoms N by the normalization condition for the wavefunction:

$$N = \int |\Psi|^2 d^3r. \tag{1.18}$$

We now consider the case of a harmonic potential V_{ext}, as the one defined in Eq. 1.9, where the charcateristic length-scale of the trap is the harmonic oscillator length a_{ho} (Eq. 1.11). Even though the diluteness condition is satisfied, the interactions between the particles play an important role in the physics of such a trapped system. Repulsive interactions ($a > 0$), indeed, cause the gas to expand, making the size of the cloud larger than in the non-interacting ideal case. The mean-field interactions become the predominant term in Eq. 1.17 when the parameter Na/a_{ho}, describing their strength, becomes $\gg 1$. Since a/a_{ho} has typical values of $\sim 10^{-3}$, this occurs frequently, and is certainly the case for numbers of atoms of the order of $N \sim 10^6$. In this case, the kinetic energy term, also called *quantum pressure*, can be neglected, leading to what is known as Thomas-Fermi approximation, valid at very low temperature and for large numbers of atoms in the condensate. In this case the stationary GPE becomes:

$$\mu\phi(\vec{r}) = \left(V_{ext}(\vec{r}) + g\phi^2(\vec{r})\right)\phi(\vec{r}) \tag{1.19}$$

from which the ground-state density profile of the trapped BEC can be extracted:

$$n_{TF}(\vec{r}) = |\phi(\vec{r})|^2 = \frac{\mu - V_{ext}(\vec{r})}{g}. \tag{1.20}$$

The chemical potential, calculated using Eq. 1.18, is given by:

$$\mu = \frac{\hbar\omega_{ho}}{2}\left(15\frac{Na}{a_{ho}}\right)^{2/5}. \tag{1.21}$$

Equation 1.20 shows that the shape of the condensate density distribution is determined by that of the external potential. For V_{ext} given by Eq. 1.9, the BEC shape is a truncated inverted parabola, with radii given by:

$$R_i = \sqrt{\frac{2\mu}{m\omega_i}}, \text{ for } i = x, y, z. \tag{1.22}$$

This allows to rewrite the density as:

$$n_{TF}(x,y,z) = \max\left[n_0\left(1 - \frac{x^2}{R_x^2} - \frac{y^2}{R_y^2} - \frac{z^2}{R_z^2}\right), 0\right]. \tag{1.23}$$

At zero temperature, the equilibrium ground state of the condensate can be described by a wavefunction $\Psi = |\Psi_0|e^{i\phi}$, where the amplitude is determined by the density $|\Psi_0(\vec{r})|^2 = n(\vec{r})$, having a smooth profile shaped by the confining potential. The phase factor ϕ is uniform over the whole system, reflecting the long-range order associated with Bose-Einstein condensation, which allows to consider the BEC as a giant matter wave as sketched in Fig. 1.1. The wavefunction Ψ has the role of order parameter in the BEC transition: we will come back to this aspect in Sec. 1.2.

1.1.3 Hartree-Fock theory: weakly interacting Bose gas at $T \neq 0$

To compare the experimental results on the thermodynamics of a Bose gas with a theoretical model, we need a theory that treats a finite temperature Bose gas and takes interactions into account. The simplest model satisfying these requirements is the Hartree-Fock (HF) theory, which self-consistently accounts for the modification of the BEC density due to thermal depletion and for interaction effects between the BEC and the thermal component [29]. A good starting-point to derive the HF equations is the Hamiltonian of Eq. 1.14, writing the field operator $\hat{\Psi}(\vec{r})$ as:

$$\hat{\Psi}(\vec{r}) = \sum_i \phi_i(\vec{r})\hat{a}_i, \tag{1.24}$$

where $\phi_i(\vec{r})$ are single-particle wavefunctions normalized to unity, and $\hat{a}_i$ ($\hat{a}_i^\dagger$) are the corresponding annihilation (creation) operators. The HF approximation consists in assuming that at equilibrium the system can be described as a gas of statistically independent single-particle states, with average occupation number:

$$n_i = \langle \hat{a}_i^\dagger \hat{a}_i \rangle. \tag{1.25}$$

The total energy $E = \langle H \rangle$ is evaluated by retaining only the terms containing at most two particle operators, with the following rules:

$$\langle \hat{a}_i^\dagger \hat{a}_k \rangle = n_i \delta_{ik}, \tag{1.26}$$

$$\langle \hat{a}_i^\dagger \hat{a}_j^\dagger \hat{a}_k \hat{a}_l \rangle = n_i n_j, (\delta_{ik}\delta_{jl} + \delta_{il}\delta_{jk}), \text{ for } i \neq j, \tag{1.27}$$

$$\langle \hat{a}_i^\dagger \hat{a}_i^\dagger \hat{a}_i \hat{a}_i \rangle = n_i(n_i - 1). \tag{1.28}$$

Separating the contribution of the condensate ($i = 0$, with occupation number $N_0 = n_{i=0}$) from the other states, the energy of the system results to be:

$$\begin{aligned} E = \int \Bigg[& \frac{\hbar^2}{2m} N_0 |\nabla\phi_0|^2 + \sum_{i\neq 0} \frac{\hbar^2}{2m} n_i |\nabla\phi_i|^2 + V_{ext}(\vec{r})(n_0(\vec{r}) + n_T(\vec{r})) + \\ & + \frac{g}{2} n_0^2(\vec{r}) + 2g n_0(\vec{r}) n_T(\vec{r}) + g n_T^2(\vec{r}) \Bigg] d^3r, \end{aligned} \tag{1.29}$$

where

$$n_0(\vec{r}) = N_0 |\phi_0(\vec{r})|^2 = |\Psi_0(\vec{r})|^2 \tag{1.30}$$

is the condensate density, fixed by the order parameter $\Psi_0 = \sqrt{N_0}\phi_0$, and

$$n_T(\vec{r}) = \sum_{i\neq 0} n_i |\phi_i(\vec{r})|^2 \tag{1.31}$$

is the thermal density.

The single-particle state occupation numbers n_i and the wavefunctions ϕ_i are determined by the minimization of the grand canonical potential $\Omega = E - TS - \mu N$, where $N = \sum_i n_i$ and, consistently with the assumption of statistically independent single-particle excitations, the entropy S is calculated using the ideal Bose gas expression [29]:

$$S = k_B \sum_i \left[(1 + n_i) \ln(1 + n_i) - n_i \ln n_i \right]. \tag{1.32}$$

From the minimization of the grand canonical potential (setting $\partial(E-TS-\mu N)/\partial n_i = 0$), the occupation numbers are found:

$$n_i = \frac{1}{\exp\left[\beta(\epsilon_i - \mu)\right] - 1}, \tag{1.33}$$

which corresponds to the standard result for Bose statistics. The energy ϵ_i of the ith single-particle level is related to the total energy by the expression:

$$\epsilon_i = \frac{\partial E}{\partial n_i}. \tag{1.34}$$

Bose-Einstein condensation starts when μ approaches the energy ϵ_0 of the lowest-energy single-particle state. Since S depends only on the occupation numbers n_i, as shown by Eq. 1.32, one can find the single-particle wavefunctions ϕ_i by minimizing the energy 1.29 at constant S and N, with the normalization condition $\int dr|\phi_i|^2 = 1, \forall i$. This yields the following equations, for the condensate wave function Ψ_0:

$$\left(-\frac{\hbar^2\nabla^2}{2m} + V_{ext}(\vec{r}) + g[n_0(\vec{r}) + 2n_T(\vec{r})]\right)\Psi_0 = \mu\Psi_0, \tag{1.35}$$

and for the excited particle states:

$$\left(-\frac{\hbar^2\nabla^2}{2m} + V_{ext}(\vec{r}) + 2gn(\vec{r})\right)\phi_i(\vec{r}) = \epsilon_i\phi_i(\vec{r}). \tag{1.36}$$

Together with the normalization relation

$$N = \int n(\vec{r})d^3r = \int (n_0(\vec{r}) + n_T(\vec{r}))d^3r, \tag{1.37}$$

the above equations are known as Hartree Fock equations. Solving them self-consistently, one obtains the density profiles for the condensate and the thermal component.

It is worth noticing that, at $T = 0$, Eq. 1.35 corresponds to the GPE 1.16, which can thus be considered as the HF equation for the ground-state of the system. At finite temperatures, besides the interactions among the particles of the BEC, the HF model includes also the interaction with the thermal component, through the term $2gn_T$ in Eq. 1.35, where the factor of 2 is due to exchange effects.

1.1.4 HF model for the uniform system

In a uniform system of bosons confined in a volume V, for $V_{ext} = 0$, the solution of the HF equations is rather simple. Above the critical point, when no single-particle state is macroscopically occupied, each wave function can be written as a plane wave $\phi_k = e^{ikr}/\sqrt{V}$, labeled by the wavevector k. The particle density becomes

$$n = \sum_k n_k/V, \tag{1.38}$$

and the energy of the system

$$E = \sum_k \frac{\hbar^2k^2}{2m}n_k + gn^2V. \tag{1.39}$$

The single-particle energies are then

$$\epsilon_k = \frac{\partial E}{\partial n_k} = \frac{\hbar^2 k^2}{2m} + 2gn, \tag{1.40}$$

corresponding to the single-particle kinetic energy shifted by the contribution of the interactions, described by the mean-field energy $2gn$. In the thermodynamic limit[2], the density can be explicitly calculated replacing the sum in Eq. 1.38 with an integral over the wavevectors k, which yields the expression:

$$n = \frac{1}{\lambda_T^3} g_{3/2}\left(e^{(\mu-2gn)/(k_B T)}\right). \tag{1.41}$$

This is valid above the critical temperature T_c. If the temperature of the system decreases at fixed density, the phase space density $PSD = n\lambda_T^3$ increases, which, according to Eq. 1.41, means that also μ must increase. Bose-Einstein condensation occurs when μ reaches the energy of the lowest-lying single-particle state, which is the one at $k = 0$, with $\epsilon_0 = 2gn$. From this we find again the expression for the critical temperature:

$$T_c = \frac{2\pi\hbar^2}{mk_B}\left(\frac{n}{\zeta(3/2)}\right)^{2/3} \tag{1.42}$$

which corresponds to the IBG expression 1.5, but in this case with the density given by the HF theory.

Below T_c a macroscopic number of atoms occupies the lowest-energy state, whose contribution must be separated from the other states. The wave function of the system becomes:

$$\hat{\Psi}(\vec{r}) = \sqrt{n_0} + \sum_{k\neq 0} \frac{e^{ikr}}{\sqrt{V}} a_k, \tag{1.43}$$

and the total energy of Eq. 1.29 takes the form:

$$E = \sum_{k\neq 0} \frac{\hbar^2 k^2}{2m} n_k + V\left(\frac{1}{2} g n_0^2 + 2g n_T n_0 + g n_T^2\right) \tag{1.44}$$

The chemical potential μ and the energy ϵ_k of the excitation states with $k \neq 0$ are found using Eq. 1.34:

$$\mu = \frac{\partial E}{\partial n_0} = g n_0 + 2g n_T, \tag{1.45}$$

$$\epsilon_k = \frac{\partial E}{\partial n_k} = \frac{\hbar^2 k^2}{2m} + 2g(n_0 + n_T). \tag{1.46}$$

The thermal density is again defined as

$$n_T = \sum_{k\neq 0} n_k / V = \frac{1}{\lambda_T^3} g_{3/2}\left(e^{(\mu-2gn)/(k_B T)}\right), \tag{1.47}$$

while the total density is now given by:

$$n = n_0 + n_T. \tag{1.48}$$

Combining Eqs.1.45 and 1.47, the condensate density is obtained:

$$n_0 = \mu/g - 2n_T. \tag{1.49}$$

---

[2] The thermodynamic limit is obtained when $V \to \infty$, keeping the density n constant

1.1.5 Thermodynamics of uniform Bose gas

The thermodynamic behavior of the uniform ideal Bose gas and of the weakly interacting Bose gas, described by the HF model, are predicted to display important differences, especially in the condensed phase.

Chemical potential In the case of the IBG, the chemical potential is $\mu = 0$ for any $T \leq T_c$ and given by Eq. 1.6 for $T > T_c$. On the contrary, the chemical potential predicted by the HF model (Eq. 1.45) is equal to gn at $T = 0$, when $n_0 = n$, and increases with temperature in the condensed phase, reaching a maximum at the critical point, where $\mu = 2gn$ due to exchange effects. Above T_c the contribution of the condensate ceases to be relevant and the chemical potential becomes $\mu_{HF} = \mu_{IBG} + 2gn$, where μ_{IBG} is given by Eq. 1.6.

Pressure Also the pressure of the uniform Bose gas shows important differences between the non-interacting IBG case and the HF model. For the IBG, the pressure can be found using the thermodynamic relation $p = 2/3E/V$, where E is the total energy and V the volume occupied by the gas. Since:

$$E = \frac{3}{2}k_B T \frac{V}{\lambda_T^3} g_{5/2}(1), \text{ for } T \leq T_c \tag{1.50}$$

$$E = \frac{3}{2}k_B T \frac{V}{\lambda_T^3} g_{5/2}(z), \text{ for } T > T_c, \tag{1.51}$$

where $z = \exp(\mu/k_B T)$ is the fugacity, one finds that the pressure is

$$p = p_c = \frac{k_B T}{\lambda_T^3} g_{5/2}(1), \text{ for } T \leq T_c \tag{1.52}$$

and

$$p = \frac{k_B T}{\lambda_T^3} g_{5/2}(z), \text{ for } T > T_c. \tag{1.53}$$

Within the HF model, the equation for the pressure p in the uniform Bose gas can be found from the grand-canonical potential $\Omega = -pV$, and results to be:

$$p = gn^2 - \frac{1}{2}gn_0^2 + \frac{k_B T}{\lambda_T^3} g_{5/2}\left(e^{(\mu - 2gn)/(k_B T)}\right) \tag{1.54}$$

Isothermal compressibility The isothermal compressibility is defined as the relative variation of density of the gas in response to a pressure variation, at constant temperature:

$$k = \left(\frac{1}{n}\right) \frac{\partial n}{\partial p}\bigg|_T \tag{1.55}$$

Since in the IBG the pressure is constant in the superfluid phase, the compressibility is infinite for $T \leq T_c$. Also the HF model predicts a divergence at the critical point, but a finite compressibility below T_c [29]. The divergence of the compressibility at the transition in the uniform Bose gas is a direct consequence of the second-order nature of the BEC phase transition [32].

In Figs. 3.10, 3.8 and 3.9 of Chapter 3, we compare the theoretical predictions for the behavior of the above thermodynamic quantities to the experimental results obtained in our laboratory.

1.1.6 Non-uniform Bose gas and Local Density Approximation

In presence of an external potential V_{ext}, the HF equations describing the system are Eqs. 1.35 and 1.36, which should be solved self-consistently, together with the normalization condition 1.37, to find the thermal and BEC density profiles.

If the system is sufficiently large and V_{ext} varies smoothly in space, the so-called Local Density Approximation (LDA) can be applied. In this framework, the trapped, inhomogeneous system can be viewed as an ensemble of locally homogeneous systems. The gas occupying a small volume at a certain position $\vec{r}$ is supposed to be in thermal and chemical equilibrium. This allows to write the global chemical potential μ_0 for the whole system as the sum of the local value of the chemical potential and of the external potential V_{ext}:

$$\mu_0 = \mu(n(\vec{r}), T) + V_{ext}(\vec{r}) \tag{1.56}$$

In the case of the harmonic trapping potential of Eq. 1.9, μ_0 corresponds to the value of the chemical potential at the center of the trap, where $V_{ext}(\vec{r} = 0) = 0$. The above Eq. 1.56 is an implicit equation for the density profile $n(\vec{r}, T)$ of the trapped gas at a temperature T, and allows to relate the properties of the trapped system to those of the corresponding (local) uniform system, by performing the substitution:

$$\mu \rightarrow \mu_0 - V_{ext} \tag{1.57}$$

in the equations for the uniform system.

If one applies the substitution of Eq. 1.56 to the weakly interacting Bose gas at $T = 0$, where $\mu = gn$, one immediately retrieves the Thomas-Fermi result $n(\vec{r}) = (\mu_0 - V_{ext}(\vec{r}))/g$ (Eq. 1.20).

For the weakly interacting Bose gas, in a potential V_{ext}, the HF equation for the density of thermal atoms becomes, in LDA:

$$n_T(\vec{r}) = \frac{1}{\lambda_T^3} g_{3/2}\left(e^{(\mu_0 - V_{ext} - 2gn(\vec{r}))/k_B T}\right). \tag{1.58}$$

One can obtain the same result by directly solving the HF equations in a semiclassical approximation, approximating the $k \neq 0$ single-particle wavefunctions with plane waves [29], which requires similar assumptions as those underlying the LDA. In the same approximation the local condensate density is found making the substitution of Eq. 1.57 in Eq. 1.49:

$$n_0(\vec{r}) = \frac{\mu_0 - V_{ext}}{g} - 2n_T, \text{ with } n(\vec{r}) = n_0(\vec{r}) + n_T(\vec{r}). \tag{1.59}$$

The LDA is a reliable approximation as long as gradient terms and finite-size effects in the density profile are negligible. For this reason, the system needs to be sufficiently large, and the potential smooth enough on the lengthscales typical of the atomic system. The LDA is not guaranteed to hold in presence of sharp local variations of the density profile, as in the critical region at the boundary between the condensate and the thermal cloud.

Besides being useful to find a good approximation of the theoretical density profile in a given potential, from an experimental point of view the LDA is a powerful tool also because it allows to extract general properties of uniform matter by performing measurements on trapped samples, which are easier to obtain experimentally. We used the LDA in our study of the thermodynamic properties of the uniform Bose gas, the results of which are in Chapter 3.

1.1.7 Corrections to critical temperature and condensate fraction

Besides modifying the density profile of a trapped gas, interactions also have an effect on its critical temperature and on the condensate fraction as a function of T/T_c. The critical temperature of an ideal Bose gas in a harmonic trap is given by Eq. 1.12. Since at the onset of condensation the system is still rather dilute, interactions are not expected to cause large variations of the transition temperature. Their effect can be quantified treating the interaction in the mean-field approximation, using the HF theory. We consider the expression for the density of thermal atoms given by Eq. 1.58. Bose-Einstein condensation occurs at the temperature T_c where n_T satisfies the following normalization condition for the total number of atoms N:

$$N = \int n_T(\vec{r}, T_c, \mu_c) d^3\vec{r}, \tag{1.60}$$

where μ_c is the chemical potential corresponding to the lowest single-particle energy ϵ_k in Eq. 1.36. For systems with a large number of particles, the kinetic energy term in the Hamiltonian governing Eq. 1.36 can be neglected with respect to the interaction term, and $\mu_c = 2gn(0)$, where $n(0)$ is the density at the center of the cloud. Expanding Eq. 1.60 around the IBG critical point (where $T_c = T_c^0$ and $\mu_c = 0$), one finds that interactions cause a shift of the critical temperature $\delta T_c = T_c - T_c^0$ (see [29] and [33] for the derivation), given by:

$$\frac{\delta T_c}{T_c^0} = -1.32 \frac{a}{a_{ho}} N^{1/6}, \tag{1.61}$$

where a is the scattering length and a_{ho} the harmonic oscillator length defined in Eq. 1.11. For repulsive interactions ($a > 0$) this shift is negative, meaning that the critical temperature is lower than that of an ideal (non interacting) Bose gas in the same trap . The shift is linear in the scattering length, while it has a weak dependence on the total number of atoms.

Also other corrections to T_c are worth to be mentioned, such as the shift due to finite-size effects, which are relevant in the case of systems with small numbers of atoms N (while before we have considered N to be large). This shift can be quantified by (see Sec. C of Ref.[34]):

$$\frac{\delta T_c^0}{T_c^0} = -0.73 \frac{\bar{\omega}}{\omega_{ho}} N^{-1/3}, \tag{1.62}$$

where $\bar{\omega} = (\omega_x + \omega_y + \omega_z)/3$ and $\omega_{ho} = (\omega_x \omega_y \omega_z)^{1/3}$. In the case of systems with a large number of atoms, as in our case, this finite-size correction can be neglected being much smaller than the shift caused by interactions.

The Hartree-Fock model, taking the interactions between the particles into account, also predicts a behavior of the condensate fraction with the relative temperature T/T_c that is different from that of a non interacting Bose gas. In the approximation where the contribution to the density given by thermal atoms can be neglected in the region occupied by the BEC, one can write the condensate fraction as (see Eq. 13.40 in [29]):

$$\frac{N_0}{N} = 1 - \left(\frac{T}{T_c^0}\right)^3 - \frac{\zeta(2)}{\zeta(3)} \eta \left(\frac{T}{T_c^0}\right)^2 \left[1 - \left(\frac{T}{T_c^0}\right)^3\right]^{2/5}, \tag{1.63}$$

where $\zeta(n)$ is the Riemann function and $\eta = \mu(T=0)/(k_B T_c^0)$.
These expressions will be used in Chap. 4.

1.2 Bose-Einstein condensation: out-of-equilibrium processes

1.2.1 Continuous phase transitions

In this section we consider the out-of-equilibrium processes that are intrinsically related with the crossing at finite rate of the Bose-Einstein condensation phase transition.

A phase transition consists, in general, in the transformation of the equilibrium state of a system from an initial phase to another one, having significantly different physical properties. Phase transitions are traditionally divided in two classes, depending on the thermodynamic behavior during the transition [35]:

- *First order* phase transitions exhibit a discontinuity in the first derivative of the free energy with respect to some thermodynamic variable. Examples are the liquid to gas or liquid to solid transitions occurring in water, where this discontinuity manifests itself as latent heat.
- For *second order* or *continuous* phase transitions, instead, the first partial derivatives of the free energy are continuous during the transition. Examples are the paramagnetic to ferromagnetic and the normal to superfluid phase transitions. Second order phase transitions involve a spontaneous symmetry breaking, with the transformation from a disordered phase to an ordered one. An *order parameter* can be defined, which is zero on one side of the transition and acquires a finite value when the transition is crossed. The parameter whose variation causes the phase transition is usually called *control parameter*. The value of the control parameter at which the transition is crossed is defined *critical point*.

Bose-Einstein condensation can be classified as a second order phase transition. The control parameter is the temperature T, whose decrease causes a transformation from an initially disordered, uncorrelated thermal phase into the BEC phase, where the formation of an order parameter takes place, corresponding to the condensate complex wavefunction $\Psi = |\Psi|e^{i\varphi}$. The squared amplitude of Ψ represents the condensate density, while the phase becomes the same in the whole system, a signature of the long-range order characterizing the lowest energy state of an equilibrium BEC. This phase is chosen randomly when the transition is crossed, determining a spontaneous symmetry breaking.

In general for a second order phase transition, one can define a dimensionless parameter expressing the distance of the control parameter T to the critical point T_c:

$$\epsilon = \frac{T_c - T}{T_c}. \tag{1.64}$$

Statistical fluctuations of the order parameter play an important role in the crossing of the transition. The spatial scale over which such fluctuations are correlated is called *correlation length* ξ. At the transition the equilibrium correlation length exhibits a power-law divergence:

$$\xi = \frac{\xi_0}{|\epsilon|^{\nu}}, \tag{1.65}$$

Also the *relaxation time* τ, needed by the system to establish such diverging correlations, diverges at the transition:

$$\tau = \frac{\tau_0}{|\epsilon|^{z\nu}}, \tag{1.66}$$

where ξ_0 and τ_0 depend on the microscopic physical properties of the actual system, while ν and z are exponents depending only on the universality class of the phase transition, known as equilibrium correlation length critical exponent and dynamical critical exponent, respectively [36, 37, 23].

The divergence of the relaxation time expresses the fact that the system requires an increasingly long time to adapt even to small fluctuations of the control parameter. This is a consequence of the general phenomenon of *critical slowing down* of the dynamics in the vicinity of critical points, which is not limited to second order phase transitions only, but extends in general to critical phenomena in complex systems. An accurate observation of signs of this slowing down could be used, for instance, to determine the vicinity to "no-return" tipping points, where a small fluctuation in the conditions can lead to a large change in the state of the system, which could help to make predictions on the thresholds for catastrophic climate change events, population collapse in ecosystems, and financial markets collapse [38, 39, 40, 41, 42].

As a consequence of the divergence of the relaxation time, second order phase transitions are always crossed in a *non-adiabatic* regime: the system is inevitably *out of equilibrium* when the control parameter is in the vicinity of the critical point. In an extended system, moreover, the information about the choice of the order parameter can propagate only at a finite speed, determined by the causality principle. As a consequence, the order parameter takes up different values in distant regions of the system, with the formation of independent domains. Topological defects may then originate when the domain boundaries merge in the relaxation of the system after the crossing of the transition.

1.2.2 Kibble-Zurek mechanism

The concept explained above is at the basis of the Kibble-Zurek mechanism (KZM) [6, 7], a milestone result for the general description of systems crossing a second order phase transition. The idea was originally developed by T. W. B. Kibble [6, 43] to explain the formation of cosmical anisotropies in the early universe, in the assumption of an original unification of all fundamental interactions. Kibble proposed that the rapid cooling and expansion of the universe after the Big Bang could have led to a spontaneous breaking of the related gauge symmetry, with the formation of local domains of the order parameter and the generation of topological defects such as monopoles, cosmic strings, and domain walls, possible precursors of later cosmological structures. Kibble also pointed out an analogy between this mechanism and the behavior of a ferromagnetic material cooled below the Curie point, where independent magnetization domains can form as a consequence of symmetry breaking. The extension of this idea to continuous phase transitions, taking place in other condensed matter systems, was further developed by W. H. Zurek with a paper titled "Cosmological experiments in superfluid Helium?" [7]. With this analogy, an important background was provided for testing cosmological critical phenomena in a variety of experimentally accessible platforms. Zurek also determined general scaling laws relating the typical domain size and defect density to the rate at which the transition is crossed [44]. Several reviews explain the Kibble-Zurek mechanism, for instance [36].

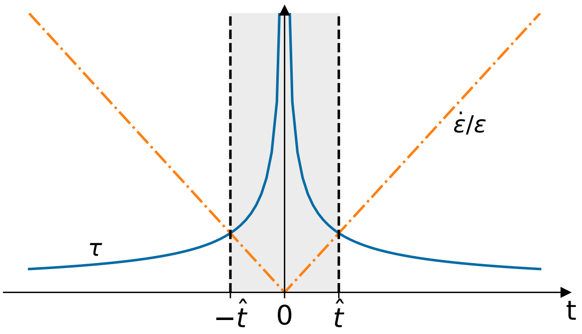

Figure 1.3: Cartoon picture of the freeze-out condition represented in the adiabatic-frozen-adiabatic approximation. During a linear quench, the variation of the reduced control parameter $\epsilon = t/\tau_Q$ causes the system to cross the transition point from the high symmetry, disordered, phase ($t < 0$) to the low symmetry, ordered, phase ($t > 0$). The dashed orange line represents the time needed for the control parameter to reach the critical point $t = \dot{\epsilon}/\epsilon$, while the blue solid line the qualitative behavior of the equilibrium relaxation time τ, diverging at the transition in $t = 0$. The freeze-out time $\hat{t}$ is defined as the times at which τ becomes equal to the time elapsed after crossing the transition. In this schematic picture, the dynamics is frozen in the time interval $[-\hat{t}, +\hat{t}]$ (gray region), and adiabatic outside.

A simplified scenario is generally considered, in which the temperature, representing the control parameter, is lowered in a linear way across the transition. The reduced control parameter of Eq. 1.64 can then be rewritten as:

$$\epsilon(t) = \frac{t}{\tau_Q}, \tag{1.67}$$

where $\tau_Q = 1/\dot{\epsilon}$ is the characteristic timescale of the temperature ramp (or *quench*) across the transition. One obtains, then, for the equilibrium correlation length:

$$\xi = \frac{\xi_0 \tau_Q^{\nu}}{|t|^{\nu}}, \tag{1.68}$$

and for the relaxation time:

$$\tau = \frac{\tau_0 \tau_Q^{z\nu}}{|t|^{z\nu}}. \tag{1.69}$$

Figure 1.3 qualitatively clarifies the interplay between the finite quench rate and the divergence of the relaxation time at the transition. Far away from the critical point (i.e., for $|\epsilon| \gg 0$), the equilibrium relaxation time is small with respect to the time required to reach the transition: the system has in this case enough time to adapt to the externally imposed variation of the control parameter, with an almost adiabatic dynamics. In the vicinity of $\epsilon(t) = 0$, instead, the dynamics becomes essentially frozen, due to the critical slowing down. The system would, indeed, require an infinitely long time to adapt to the temperature variation and becomes unable to follow the finite rate quench. On the basis of this intuition, the dynamics is divided in three stages, as shown in Fig. 1.3: *adiabatic*, *frozen* and *adiabatic* again, as the control parameter is varied from $\epsilon(t) < 0$ to $\epsilon(t) > 0$, crossing the transition at $t = 0$. This simplification is often referred to as *adiabatic-impulse* approximation and captures the essence of the inevitable nonequilibrium dynamics involved in crossing the transition at finite rate. The boundary between the adiabatic and frozen stages is given by the so-called *freeze-out* time $\hat{t}$, occurring when the equilibrium relaxation time τ becomes equal to the time required by the control parameter to reach the transition:

$$\tau(\hat{t}) = \hat{t}. \tag{1.70}$$

Using Eq. 1.69, one finds then:

$$\hat{t} = \left(\tau_0 \tau_Q^{z\nu}\right)^{\frac{1}{1+z\nu}}. \tag{1.71}$$

As a consequence of the critical slowing down, the order parameter cannot keep up with the change of $\epsilon(t)$, and the correlation length remains frozen to the value $\hat{\xi}$ at the freeze-out time $-\hat{t}$, for the whole duration of the frozen period.[3] This length-scale determines the average size of the domains of the order parameter that form upon crossing the transition:

$$\hat{\xi} = \xi(-\hat{t}) = \xi_0 \left(\frac{\tau_Q}{\tau_0}\right)^{\frac{\nu}{1+z\nu}}. \tag{1.72}$$

Equation 1.72 predicts a universal power-law scaling of the average domain size with the quench time τ_Q, with an exponent $-\nu/(1+z\nu)$ that depends only on the values of the critical exponents describing the system's equilibrium state. After the freeze-out, defects can form due to the merging of the boundaries of independent domains. The average density of defects n_d in the system can be determined, using Eq. 1.72, as the ratio between the size of the defects $\hat{\xi}^d$ and the size of the domains $\hat{\xi}^D$ [24]:

$$n_d \sim \frac{\hat{\xi}^d}{\hat{\xi}^D} = \frac{1}{\xi_0^{D-d}} \left(\frac{\tau_0}{\tau_Q}\right)^{(D-d)\frac{\nu}{1+z\nu}}, \tag{1.73}$$

where D is the dimensionality of the system and d that of the defects. The higher the rate at which the transition is crossed, the shorter becomes the characteristic quench time τ_Q, with the correlation length also *freezing out* at a smaller value $\hat{\xi}$, which leads to the formation of a larger density of defects. This power-law dependence of the defect density on the characteristic quench time $n \propto \tau_Q^{-\alpha}$ is one of the main predictions of the KZM.

The above described adiabatic-frozen-adiabatic scenario is of course a simplification of the actual dynamics, since the actual evolution of the system does not completely stop at the freeze-out time, as pointed out in [45, 36, 22, 23, 46]. At the microscopic level, the state of the system continues indeed to evolve, and local thermodynamic equilibrium may even be maintained. Even the order parameter does not completely cease to evolve, but in the frozen region it cannot follow its equilibrium value, that would be dictated by the instantaneous change of the control parameter, catching up with it only locally after the critical point has been passed, with a delay of the order of $\hat{t}$. Below we will further consider this aspect when considering the specific case of a trapped Bose gas. Another limitation to the simplified scenario described above is given by the fact that the KZM does not capture the coarse-graining processes leading to the merging of the initial small domains, nor the later interaction dynamics that can take place between defects.

Because of the above points, the actual density of defects is often smaller by a factor $f \sim 5-10$ than the one predicted by Eq. 1.73, which provides only an order-of-magnitude estimation, depending also on the system-specific quantities ξ_0 and τ_0. The main prediction of the KZM remains then the fact that independent order parameter domains indeed form upon crossing the transition, leading to the spontaneous formation of defects, the

---

[3] The freeze-out dynamics, in this simplified picture, is considered to be symmetric, with the frozen region extending from $-\hat{t}$ to $+\hat{t}$ and the correlation length at $-\hat{t}$ being equal to the value at $\hat{t}$.

number of which is determined by the average domain size and exhibits a power-law scaling with the quench rate, with universal exponents dependent on the universality class of the transition.

1.2.3 Experiments testing the Kibble-Zurek mechanism

Experiments testing the KZM, like the ones directly proposed by Zurek [7, 44], were soon performed in a variety of different systems, demonstrating the universality of the mechanism. The first of these experiments were performed in nematic liquid crystals [47, 48], fluids composed of rod-shaped molecules, which are randomly oriented at high temperatures or low concentrations (isotropic phase), and aligned along a common direction at low temperatures or high concentrations (nematic phase). Rapid temperature and pressure quenches were shown to cause the formation of domains due to a local choice of the alignment direction, with an average domain size in fair agreement with the KZ predictions [48], and the generation of various types of topological defects [47]. Notably, the considered phase transition is of first order, suggesting a more general validity of the hypothesis at the basis of the KZM.

Following Zurek's proposal, experiments on superfluid Helium were performed, showing the generation of quantized vortices caused by quenches across the normal to superfluid transition [49, 8, 50].

Other systems in which the Kibble-Zurek mechanism has been observed, upon crossing a second order phase transition at finite rate, are superconducting films [9], annular Josephson junctions [51, 52], ion chains [12, 53, 11], as well as ultracold atoms.

Kibble-Zurek mechanism in ultracold atom systems

Ultracold atomic gases were soon considered as ideal candidates to test the KZM [54], thanks to the high degree of experimentally achievable control and tunability of the system's characteristic parameters, such as the temperature, density, interaction strength and geometry of the system, which allow for the study of out-of-equilibrium processes in a very clean environment.

Experiments testing the KZM have been performed in a variety of ultracold atom systems, in different geometries and dimensionalities. In particular, the effect of the finite-rate crossing of the BEC phase transition has been explored in 3D harmonically confined Bose gases [55, 19, 56, 24, 25, 26], as well as in homogeneous Bose gases: in a 3D box potential [18], in an annular geometry, investigating the superfluid flow winding number as in Zurek's initial proposals [44, 20], and in a quasi-2D uniform potential [21]. These studies focused on the statistics of topological defect formation as a function of the cooling rate [19, 21, 24, 25], and on the emergence of coherence [18], investigating the evolution of the system's correlation length [17]. The relation between the defect density and the quench time was investigated, finding a good agreement with the predicted scaling law behavior, at least for slow enough cooling rates, allowing for a determination of the combination of critical exponents $\nu/(1+\nu z)$ (see Eq. 1.73) [37].

The Kibble-Zurek mechanism was also generalized to quantum phase transitions at zero temperature, that can be crossed by varying the interaction parameters, such as, for instance, the transition from the Mott insulator to the superfluid phase in a gas in an optical lattice [57, 58, 59]. The effects of rapidly crossing a quantum phase transition have been explored also in multi-component Bose-Einstein condensates, studying the effect of quenches in the ferromagnetic phase of a spinor BEC, with the formation of spin-domains and the occurrence of phase separation [16, 60, 61, 62, 63, 64, 65, 66]. The KZM has been investigated also in fermionic systems [67, 68].

1.2.4 BEC formation in a trapped Bose gas: KZ and beyond

Several studies have been performed concerning the cooling, at variable rate, across the BEC phase transition of a Bose gas confined in a harmonic external potential. The spontaneous formation of quantized vortices, compatible with the KZM predictions, was first observed in 2008 in the experiment of Ref.[55], in a 3D trapped Bose gas in an oblate (pancake) geometry.

In 2013 in Trento, in the same experimental setup of this thesis work, the KZM was investigated, cooling a 3D Bose gas in a prolate (cigar-shaped) harmonic magnetic trap at variable rates across the critical temperature for BEC formation [19, 24, 69, 70]. Topological defects, identified as solitons and solitonic vortices [56], were observed to be left in the system after the quench, as a consequence of the generation of different axial phase domains due to the crossing of the phase transition at finite rate. A power-law scaling of the number of detected topological defects, in agreement with the KZ predictions, was obtained for low enough cooling rates.

For high cooling rates (fast quenches), instead, a saturation of the detected number of defects to a maximum value was observed, with a possible explanation consisting in the post-quench pair-annihilation and interaction dynamics taking place between multiple vortices [71, 24].

Such effects are not included in the simplified KZ model introduced above, which considers an infinitely long cooling ramp and does not take into account the microscopic details of the defect formation process, nor of the condensate order parameter onset and growth after the quench. The investigation of beyond KZ effects has motivated further studies, both theoretical and experimental.

Saturation of the defect density for rapid cooling ramps was recently observed also in another experiment, performed on oblate quasi 2D Bose gases confined in an optical trap [25, 26]. The observed saturation was in this case attributed to a coarsening of the dynamics at early times after the crossing of the critical point, which was verified by changing in an independent way the cooling rate at the transition and after the expected freeze-out regime [26].

In Ref. [72], the early-time coarsening after the crossing of the critical region was theoretically investigated and found to have a fundamental role in the dynamics after the crossing of any second order phase transition, especially when considering fast cooling ramps of finite duration. In particular, the authors show that after the system leaves the freeze-out region, the evolution is initially nonadiabatic, with a finite delay time being required before a well-defined condensate appears, during which the correlation length increases due to parametric coarsening. This provides a motivation for the breakdown of the KZM for fast quenches, for which the condensate formation is predicted to become insensitive to the rate at which the transition is crossed, explaining the experimentally observed saturation of the number of defects [24, 25, 26]. A delay in the formation of the order parameter, dependent on the quench time and constant for fast quenches, was predicted also in Ref [73]. Recently, beyond KZ scenarios were investigated in [74], where it was shown that, for quench rates above a critical value, the defect density as well as the freeze-out time become independent of the quench rate. In particular, the authors point out that the freeze-out time $\hat{t}$, for a realistic cooling ramp ending at a finite time t_f, should be given by the maximum between the value of the relaxation time estimated from Eq. 1.70 and the relaxation time evaluated at t_f. This has the consequence that the freeze-out time becomes independent of the quench time for rapid quenches, leading to saturation of the defect density and to a universal post-quench dynamics.

In the regime of slow cooling ramps, where experiments have shown a good agreement with KZ predictions, new simulations, based on a linearized stochastic Gross-Pitaevskii equation were recently performed for an elongated trapped Bose gas [23], like the one of our experiment, studying the effect of the different cooling rates on the condensation dynamics. In order to more precisely model the processes occurring in typical experiments, besides a linear temperature decrease also a variation of the chemical potential was included in the simulations, to account for the decrease of the number of atoms that occurs in experiments, where the temperature is lowered by means of evaporative cooling (see Sec. 2.6.3). For slow enough ramps, a universal scaling of the condensate order parameter growth was found. In the early stage after crossing the transition, the condensate growth is predicted to occur on a timescale dependent on $\hat{t} \propto \tau_Q^{\frac{z\nu}{1+z\nu}}$, with the value of the exponent being compatible both with the mean-field prediction of 1/2, as well as with the value of 0.57, which takes into account beyond-mean-field corrections. At later times, instead, the condensate growth is shown to take place on timescales directly following the quench time τ_Q. The simulations also predict a delay in the onset of condensation with respect to the time at which the critical point is crossed, caused by the freezing-out of the dynamics in the vicinity of the critical point. This leads to an overall shift of the condensate growth curves, dependent on the quench time. The duration of this delay is predicted to be proportional to the freeze-out time $\hat{t}$, with a nonuniversal proportionality factor depending on the system's parameters.

An experimental observation of this delay in the condensate growth curve could provide a direct measurement of the freeze-out time, which is still lacking. The measurement, in the same experiment, of the power-law scaling of the defect density and of the freeze-out time would be of high interest, since the two quantities have a different dependence on the critical exponents ν and z ($\hat{t} \propto \tau_Q^{\frac{z\nu}{1+z\nu}}$, while $\hat{\xi} \propto \tau_Q^{\frac{\nu}{1+z\nu}}$, see Eqs. 1.71, 1.72), that characterize the universality class of the transition and could in this way be determined independently [36, 37].

In actual experiments, however, the temperature is not directly controlled, but changed acting on other external parameters, such as the depth of the confining optical potential or the frequency of an outcoupling radio-frequency field (see Sec. 2.6.3). This makes also other timescales relevant for the characterization of the dynamics of the system in response to the variation of the external parameter. A quantity that is particularly relevant is the atomic system collisional time, which is involved in the determination of the timescales of thermalization and equilibration. It can be classically estimated as $\tau_{\text{coll}} = (\bar{n}\sigma v)^{-1}$, with $\bar{n}$ being the average density, σ the scattering cross-section and v the average atomic velocity [75]. In early works, before the KZ formalism was applied to the study of cold atom systems, this finite collisional time was suggested to be the cause of a finite delay in the onset of condensation after rapid temperature quenches [14, 13, 76].

The interplay of the above mentioned phenomena (critical slowing down and KZM, coarsening dynamics after the transition, finite collisional time) causes Bose-Einstein condensation to be a highly non-trivial process, especially when considering a wide range of cooling rates, from almost adiabatic slow ramps to quasi-instantaneous quenches, with important details still requiring further investigation. The need, in particular, of achieving a better understanding on the different timescales involved in the condensation process, motivates the experimental work reported in Chapter 4, where I present a systematic investigation on the formation dynamics of the BEC order parameter as a function of the rate at which the critical point is crossed.

Chapter 2

Experimental apparatus

The aim of this chapter is to give a virtual tour of the laboratory, providing a description of the experimental tools and procedures that allow us to cool, confine and image atomic clouds and that are used in the experiments described in Chapters 3 and 4.

The atomic species used in our experiment is sodium ^{23}Na, which has been one of the first atomic elements for which Bose-Einstein condensation was obtained [1]. Thanks to the favourable combination of its scattering cross-section ($a = 54.54 a_{\mathrm{B}}$, where a_{B} is the Bohr radius) and low three-body recombination rate, it is particularly suitable for the production of large BECs, since, in comparison to other elements, the evaporative cooling process towards degeneracy is particularly efficient [77].

Most experimental setups for ultracold atoms have a series of elements in common, that are required for the production and manipulation of ultracold atomic clouds. These are:

- a vacuum system, used to separate the ultracold gas from the external environment;
- a laser system, used for cooling, manipulating and probing the atoms. The specific frequencies of the laser light are chosen depending on the level structure of the atomic species that is used;
- a system to confine the atoms: this can be done using optical, magnetic or hybrid traps. In the experiments described in this thesis, a purely magnetic trap is used;
- radiofrequency and microwave signal generators and antennas for further manipulation of the internal state of the atoms;
- an imaging system with ccd cameras to capture images of the atomic distribution;
- an electronic control system, that interfaces the various instruments, allowing to tune their parameters and to control the sequence of actions required to perform an experiment.

In the following, I briefly describe all these parts of our experimental apparatus, focusing on the upgrades that were performed during my PhD thesis work. These upgrades mainly regarded the imaging system, that was rebuilt to gain a better resolution, and other technical improvements aimed at achieving an enhanced stability and a higher degree of control on the experiment. One of my contributions was also the development and implementation of the optical setup for the use of a Digital Micromirror Device (DMD), that allows to project arbitrary light patterns, providing enhanced possibilities in the manipulation of the cold atoms.

2.1 Laser system

In Fig. 2.1 the hyperfine energy levels of ^{23}Na are shown. To cool, probe and manipulate the atoms, we use coherent laser radiation, of which we need to precisely tune and control the frequency and optical power.

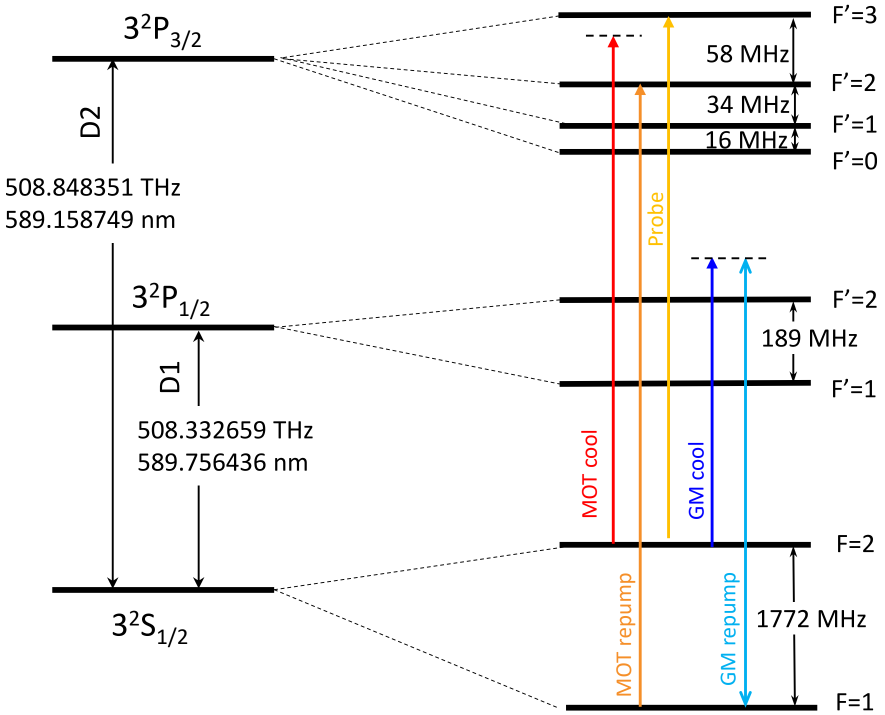

Figure 2.1: Hyperfine energy levels of the D1 and D2 transitions of ^{23}Na. The splittings are not to scale. The transitions used for the 3D MOT cooling and repumping (red and orange) and for the GM cooling and repumping (dark and light blue) are shown, as well as the transition used for probing the atoms (yellow). The frequency-splitting data are from [78].

Two main laser systems are present in our experiment. The first one is based on a laser source locked to the cycling transition $3\,^2S_{1/2}\,|F=2\rangle \rightarrow 3\,^2P_{3/2}\,|F'=3\rangle$ (D2 line) at 589.16 nm and produces the radiation used for cooling and probing the atoms. Part of the light is frequency shifted to be resonant with the $3\,^2S_{1/2}\,|F=1\rangle \rightarrow 3\,^2P_{3/2}\,|F'=2\rangle$ transition (in orange in Fig. 2.1) and is used as an optical repumper, both in the cooling stage, in a dark spot (DS) configuration [79], and to repump the atoms in $|F=2\rangle$ before imaging them with the probe light. The other laser source is locked to the D1 line $3\,^2S_{1/2}\,|F=2\rangle \rightarrow 3\,^2P_{1/2}\,|F'=2\rangle$ at 589.76 nm and is used for a gray molasses (GM) sub-Doppler cooling stage [80]. The laser radiation at $\sim$ 589 nm is produced via frequency doubling, starting from two infrared (IR) laser sources operating around 1178 nm. These were initially extended cavity diode lasers (ECDL), then substituted with distributed feedback (DFB) lasers [Innolume DFB-1178-YY-50]. The IR radiation of each source (with an optical power of about 20 mW) is amplified by a Raman amplifier [MPB RFA-P-8-1178-SF], pumped with an Yb fiber laser, to get an output power up to 7 W, on a single transverse mode, maintaining the polarization of the input beam. The infrared radiation is then frequency-doubled in a bow-tie cavity with a non-linear crystal [LEOS]. At the end of this stage about 2.5 W of visible radiation are available from each source. Fig. 2.2

shows a scheme of the optical setup for the D2 line (a) and for the D1 line (b).
The frequency of each laser source (D1 and D2) is locked to the corresponding atomic transition by means of frequency-modulated saturated absorption spectroscopy, performed on a sodium vapour cell [81].

In order to independently control the laser beams used in the different stages of the experiment, the beam at the output of each frequency-doubling cavity is split into several secondary beams by means of polarizing beam-splitter cubes and half-wave plates. The frequency and optical power of each beam is tuned by means of RF-driven Acousto-Optic modulators (AOMs) [Gooch & Housego] and Electro-Optic Modulators (EOMs) [QuBig]. Mechanical shutters [Thorlabs SHB025T [82]] are placed on each beam path and are used in combination with the AOMs to block the light when it must not reach the atoms.

For the D2 line, the various secondary beams are enumerated below, following the numbering of Fig. 2.2 (a):

1. the *spectroscopy* line, split in a probe and a pump beam. The frequency of the pump beam is modulated with respect to the probe beam by means of a double-pass AOM. The probe is split in two beams, one of which is overlapped with the counterpropagating pump beam. Both probe beams propagate through the Na heatpipe, and are detected by a differential photodiode, measuring the difference in the two absorption signals. This differential signal is then sent to a lock-in demodulator to obtain the error signal, which is finally fed to a PID controller, that acts on the laser frequency. The D2 spectroscopy line locks the laser source frequency to the $F = 2 \rightarrow F' = 3$ transition, to which the detunings listed below are referred;
2. the *3D MOT* beam, offset by $-23\,\mathrm{MHz}$ by means of two AOMs, which allow for a further tuning of the cooling frequency (this corresponds to the transition indicated in red in Fig. 2.1);
3. the atomic source line, split into the the *2D MOT* beam, with a detuning of $-10\,\mathrm{MHz}$, and the *Zeeman Slower* (ZS) beam, offset by about $-300\,\mathrm{MHz}$ by means of a double pass AOM. An EOM, operating at $1.713\,\mathrm{GHz}$, provides repumper sidebands for both lines;
4. the *dark spot/ repumper* line produces two independent laser beams at the repumper frequency, resonant with the $F = 1 \rightarrow F' = 2$ transition shown in orange in Fig. 2.1. This is done by means of a sequence of three AOMs in double pass, of which the first two (in common for the two beams) are driven at $228\,\mathrm{MHz}$ and the last one at $400\,\mathrm{MHz}$, to produce a total frequency shift of $1.712\,\mathrm{GHz}$. The two beams are used as repumper in the *Dark Spot* MOT and for imaging;
5. the *push* beam, with a detuning of $+12\,\mathrm{MHz}$;
6. the *probe* beam, split into two independent beams for the horizontal (xy) and vertical (z) probe direction. The probe light is resonant with the $F = 2 \rightarrow F' = 3$ transition. A fine tuning of the probe frequency is granted by two AOMs (one of which in common with the push beam, which is used at a different stage of the experiment).

The D1 laser setup is instead composed only by a *spectroscopy* line, analogous to the one described above, which locks the frequency of the laser source to the $3\,^2S_{1/2}\,|F = 2\rangle \rightarrow 3\,^2P_{1/2}\,|F' = 2\rangle$ D1 transition. The frequency-stabilized light is then sent to the *gray molasses* line, where two AOMs, operated at $\pm 200\,\mathrm{MHz}$ RF frequency, allow for a fine tuning

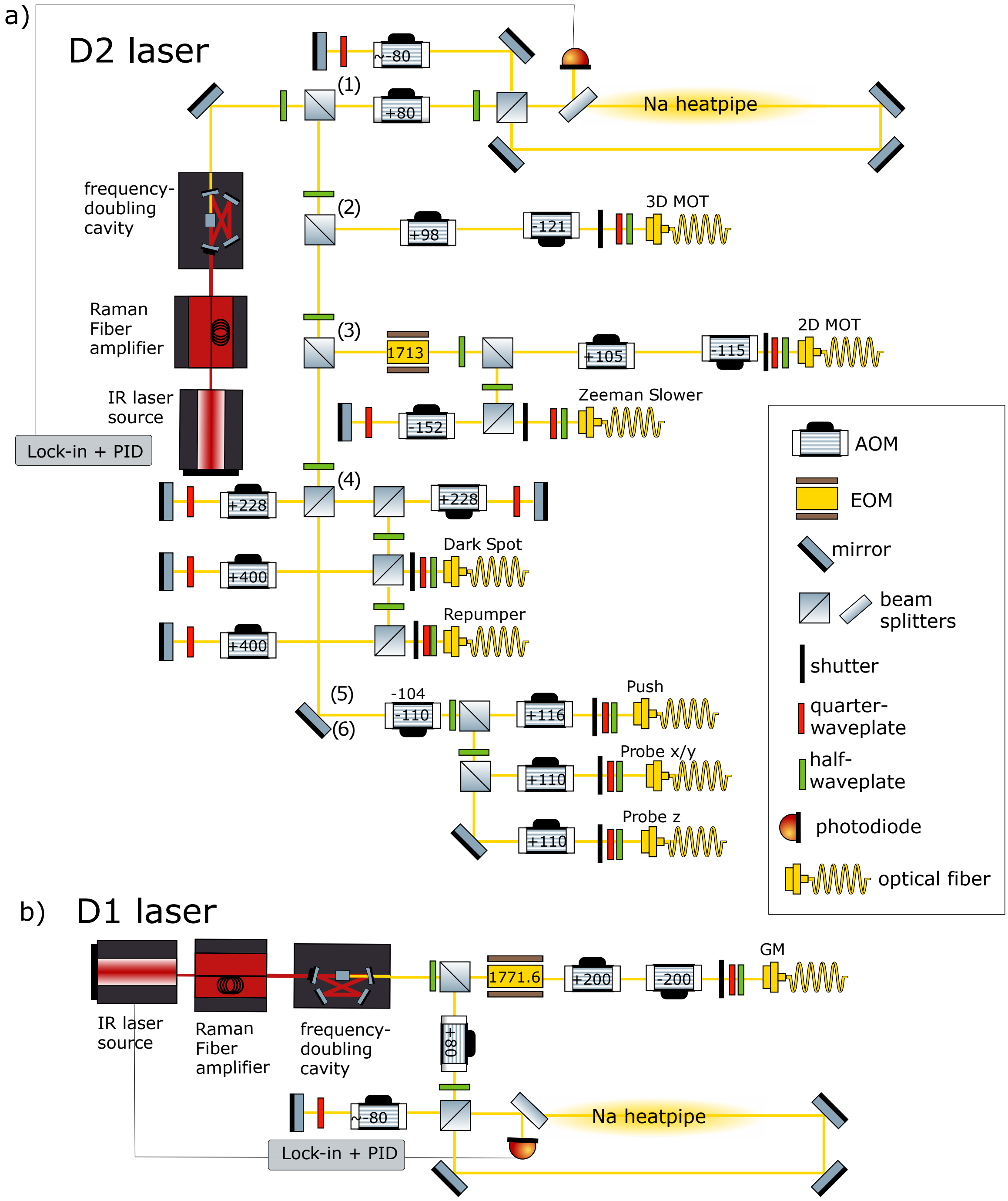

Figure 2.2: Optical scheme of the D2 laser setup (a) and D1 laser setup (b). RF frequencies in MHz are reported on top of the AOMs. Additional waveplates (not shown) are present in front of the AOMs to tune the polarization of the input light to obtain maximum diffraction efficiency. This figure, as well as the other optical setup schemes of this thesis, was drawn with the use of *ComponentLibrary* [83].

of the laser frequency and of the optical power.

The laser sources are placed on a different optical table than the one of the experiment, to which the light is delivered by means of polarization-maintaining optical fibers [Schaefter-Kirchhoff PMC-630-4.2-NA12-3-APC]. To optimize fiber coupling and stabilization, $\lambda/2$ and $\lambda/4$ waveplates are added at the input of the fibers.

On the main experimental table, another laser source with its own amplification stage is present [Innolight/Coherent Mephisto MOPA] that can provide up to 42 W at 1064 nm. Through frequency-doubling in a free-space non-linear crystal [PPSLT], visible light at 532 nm can also be obtained. Since these frequencies are far detuned from the atomic transitions, it is possible to use this light to obtain attractive (using the IR light) or repulsive (using the green light) optical potentials [84].
The DMD setup, which will be used in future experiments, has been tested using 589 nm and 532 nm light.

2.2 Vacuum system, atomic source, Zeeman slower and 2D MOT

Fig. 2.3, from Ref. [79], shows a sketch of the first stages of the experimental setup used to cool the atoms. A vacuum apparatus composed of two parts is present: a high vacuum chamber (HV) with a pressure of $\sim 10^{-7}$mbar, where the atomic source is located, and an ultra-high vacuum chamber (UHV) with a pressure $\sim 10^{-10}$mbar, where the science chamber, where the experiments are performed,is placed. A differential pumping channel with a diameter of 2 mm and a length of 22.8 mm connects the two parts of the vacuum apparatus. Each part hosts one ion pump [Varian Starcell], with nominal pumping speed of 55 L/s and a titanium sublimation pump (TSP) [Varian].

The gas of sodium atoms is obtained by heating a solid sample of sodium in an oven, located in the lower part of the apparatus [see Fig. 2.3 (b)], up to a temperature of $\sim 240\,^{\circ}$C. The hot atoms of the atomic vapour flow upwards and get captured by a 2D Magneto Optical Trap (2D MOT, shown in Fig. 2.4a), obtained by means of two circularly polarized retro-reflected laser beams and four stacks of neodymium permanent magnets (red and blue in Fig. 2.3), that produce the quadrupole magnetic field. The capture efficiency of the 2D MOT is improved by an integrated Zeeman Slower (ZS), realized by means of a red-detuned beam propagating from top to bottom towards the atomic oven, in the magnetic field gradient produced by the tails of the 2D MOT quadrupole field. The cooled atoms are then pushed towards the science cell by means of a resonant push beam, along the unconfined x direction. The resulting atomic beam finally reaches the science chamber, where it loads a 3D Magneto Optical Trap (3D MOT).

The science chamber, shown in Fig. 2.4b, is constituted by an annealed quartz cell made by Hellma Analytics, with outer dimensions of about $90 \times 60 \times 35$ mm and 5 mm thick walls (except the one on the far right in the figure, which is 4 mm thick). The cell has the shape of an irregular polyhedron: the two long lateral faces are non-parallel, to avoid spatial interference between the 3D MOT beams, while one of the short sides of the cell is connected via a flange to the UHV system. The outer surfaces of the four largest windows of the cell are covered by anti-reflection coating, which reduces the reflectivity to $\sim 0.5\%$ over a spectral range from 530 to 1100 nm.

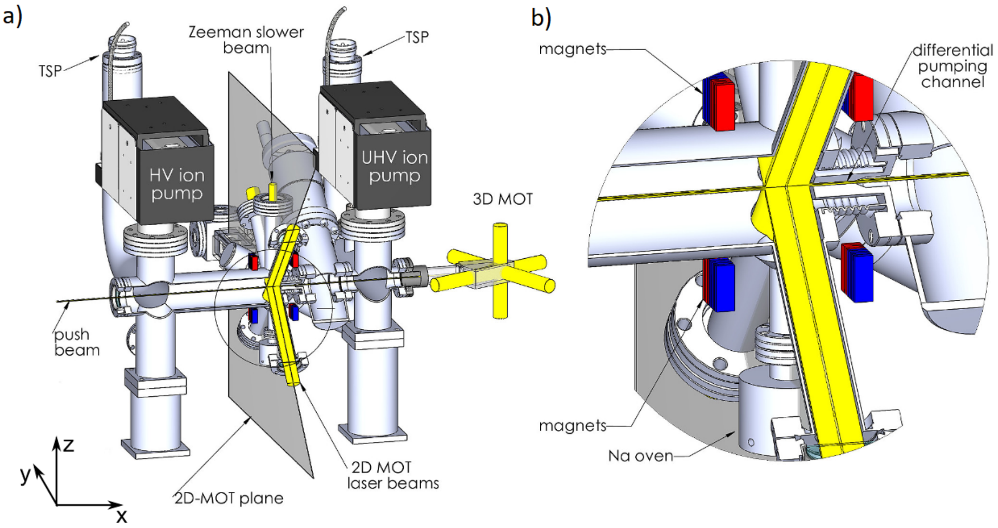

Figure 2.3: a) Sketch of the first stages of the experimental apparatus. b) Zoom on the first part of the apparatus where the Na oven and the magnets for the 2D MOT and ZS are shown. Image adapted from [79].

2.3 Magnetic fields

In the experiments described in this thesis, the atoms are confined in a magnetic trap. It is possible to trap atoms in a nonuniform magnetic field [86, 28], exploiting the Zeeman shift of the atomic energy levels [87]:

$$U_{|F,m_F\rangle}(\vec{r}) = -\vec{\mu}_{\text{at}}\vec{B}(\vec{r}) = \mu_B g_F m_F |\vec{B}(\vec{r})| \tag{2.1}$$

where

$$\mu_{\text{at}} = \mu_B g_F m_F \tag{2.2}$$

is the magnetic moment of the atoms, in units of the Bohr magneton μ_B. The potential experienced by the atoms depends on their internal state $|F, m_F\rangle$ and, in particular, on the sign of $g_F m_F$:

- if $g_F m_F < 0$ the atoms are attracted towards regions where $|\vec{B}(\vec{r})|$ is highest (*high-field seeking states*)
- if $g_F m_F > 0$ the atoms are attracted towards regions where $|\vec{B}(\vec{r})|$ is minimum (*low-field seeking states*)

Since in 3D the magnetic field can have only local minima and not maxima, the atoms can be magnetically trapped when they are in a low-field seeking state. In the case of the ground-state manifold ${}^3S_{1/2}$ of ^{23}Na, $g_F = -1/2$ for the $F = 1$ states and $g_F = 1/2$ for $F = 2$ [78]. This means that the ground-states that can be magnetically trapped are $|F, m_F\rangle = |1, -1\rangle$, $|2, 1\rangle$ and $|2, 2\rangle$, while atoms in the states $|1, 1\rangle$, $|2, -1\rangle$ and $|2, -2\rangle$ are antitrapped and those with $m_F = 0$ are, to first order in the Zeeman effect, insensitive to the magnetic field.

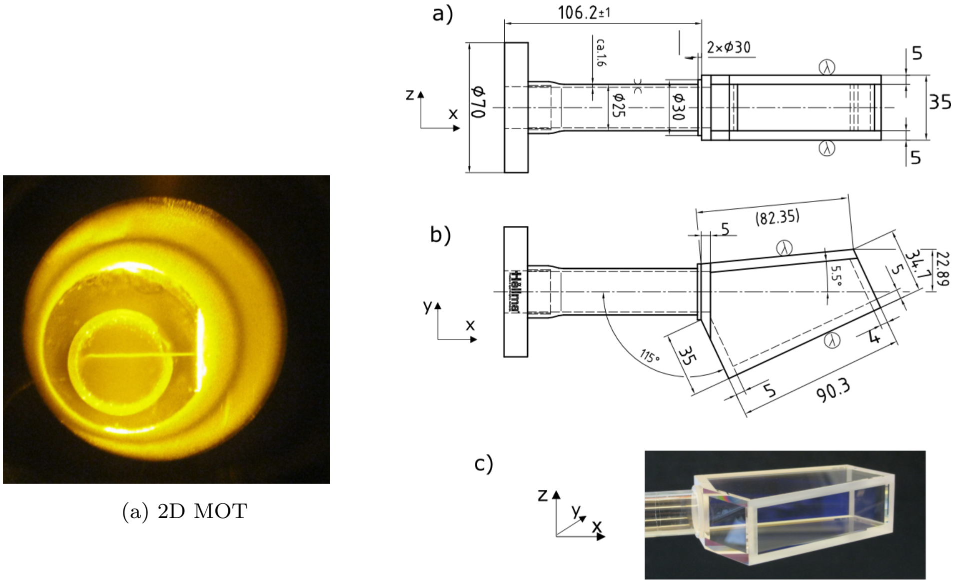

(a) 2D MOT

(b) Quartz cell: (a) view from the side and (b) from above, from the technical drawing by Hellma Analytics. The faces marked with λ are antireflection coated. (c) photograph from [70].

Figure 2.4: (a) 2D MOT fluorescence, photographed through the ZS window [70]. (b) Drawing and photograph of the quartz cell.

To confine the atoms we use a Ioffe-Pritchard (IP) trap [88], based on a static cylindrically symmetric magnetic field, with a non-zero minimum at the center, in order to avoid losses due to Majorana spin flips [28, 89]. This field is produced using the set of coils sketched in Fig. 2.6. The large cyan coils, in anti-Helmholtz configuration (i.e. with the same current flowing in opposite directions in the two coils, which are placed at a distance equal to their radius), produce a 3D quadrupole field, which is used also in the 3D MOT stage. For the conservative Ioffe-Pritchard trap, an additional set of three coils is used, formed by three coils oriented along the x axis: a *pinch coil* (green) and a pair of *compensation coils* (red). The pinch coil creates a magnetic gradient that cancels out the gradient component of the quadrupole field along x. The two compensation coils are used to reduce the bias field of the pinch coil B_0 to a few G.

The resulting magnetic field is quadratic with a bias term along x: $B_x = B_0 + B''x^2/2$, and symmetric around the x axis. The total magnetic field can be derived using Maxwell's equations and, in polar coordinates, is given by [90, 70]:

$$\vec{B}(\rho, \phi, x) = B_0 \begin{bmatrix} 0 \\ 0 \\ 1 \end{bmatrix} + B'\rho \begin{bmatrix} \cos 2\phi \\ -\sin 2\phi \\ 0 \end{bmatrix} + \frac{B''}{2} \begin{bmatrix} -x\rho \\ 0 \\ x^2 - \rho^2/2 \end{bmatrix}, \tag{2.3}$$

where $\rho = \sqrt{x^2 + y^2}$ and ϕ is the angle between y and z. Only the modulus of B enters in Eq. 2.1:

$$|\vec{B}(\vec{r})| = \left[B_0^2 + B_0 B'' x^2 + \rho^2 \left(B'^2 - \frac{B_0 B''}{2} - B' B'' x \cos 2\phi \right) + \frac{B''^2}{16}\rho^4 + \frac{B''^2}{4} x^4 \right] \tag{2.4}$$

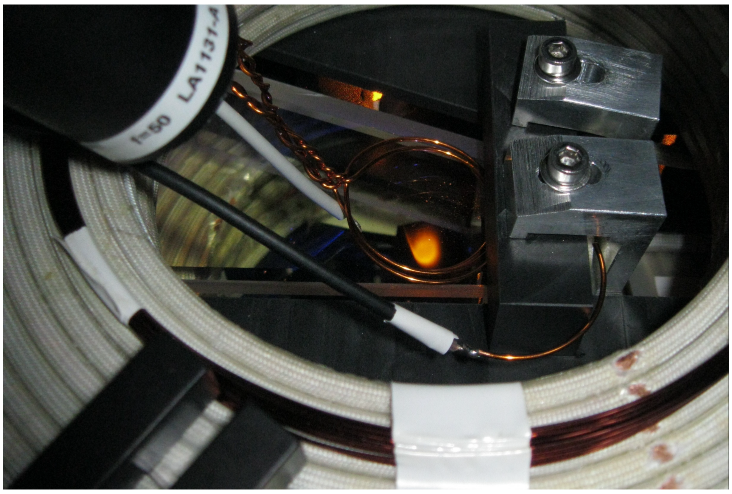

Figure 2.5: Photograph of the 3D MOT, taken before the upgrade of the vertical imaging system. The coils that generate the magnetic field are visible. A loop and a hook antenna are placed above the cell to irradiate the atoms with an RF and a microwave field, respectively. Another hook antenna is placed on the side of the glass cell. Image from [85].

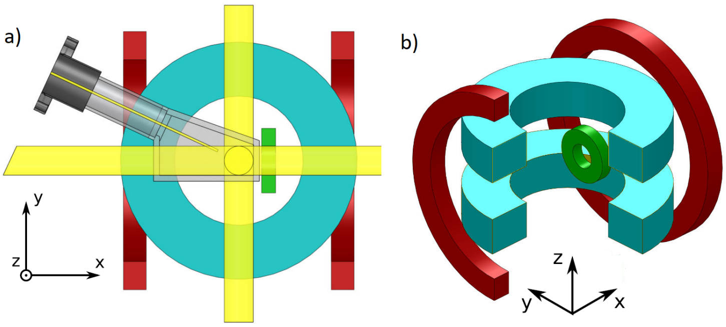

Figure 2.6: Coils used for the generation of magnetic fields. In (a) the science chamber and some optical beams (push beam, 3D MOT beams, in yellow) are also shown. Image adapted from [70].

For low-field seeking states this results in a trapping potential that, at low temperatures ($\mu_{\mathrm{at}} B_0 > k_B T$), can be written as:

$$\begin{aligned} U_{|F,m_F\rangle}(\vec{r}) &\simeq \mu_{\mathrm{at}} B_0 + \frac{\mu_{\mathrm{at}}}{2} B'' x^2 + \frac{\mu_{\mathrm{at}}}{2}\left(\frac{B'^2}{B_0} - \frac{B''}{2}\right)\rho^2 = \\ &= \mu_{\mathrm{at}} B_0 + \frac{1}{2} m\omega_\rho^2 (y^2 + z^2) + \frac{1}{2} m\omega_x^2 x^2 \end{aligned} \tag{2.5}$$

where

$$\omega_x = \sqrt{\frac{\mu_{\mathrm{at}}}{m} B''} \quad \text{and} \quad \omega_y = \omega_z = \omega_\rho = \sqrt{\frac{\mu_{\mathrm{at}}}{m}\left(\frac{B'^2}{B_0} - \frac{B''}{2}\right)} \tag{2.6}$$

are the axial and radial trapping frequencies, respectively, that characterize the strength of the magnetic confinement. Their ratio ω_ρ/ω_x is the aspect ratio of the trap, which determines the spatial distribution of the confined atomic cloud.

Three pairs of additional smaller coils in Helmholtz configuration, called *bias coils*, are present along all three orthogonal directions (not shown in the Figure). They are used to actively compensate the variations of the environmental magnetic field in the central region of the trap. This is needed in order to obtain a zero magnetic field to make the

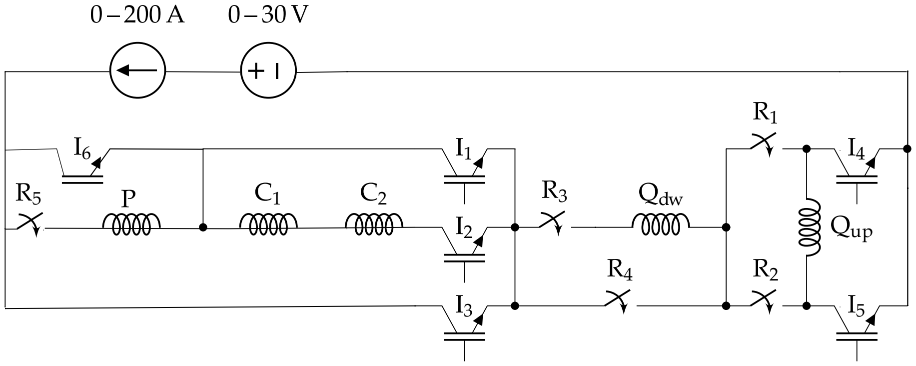

Figure 2.7: Electronic circuit used to drive the coils, labeled as P (pinch), $C_{1,2}$ (compensation), $Q_{up,dw}$ (quadrupole up and down). It is possible to switch between the different magnetic field configurations acting on the IGBT swicthes (I) and relays (R).

gray-molasses cooling stage effective. The bias coils along the x axis are, moreover, used, together with the compensation coils, to finely tune the value of the bias field B_0 in the magnetic trap, allowing to control its aspect ratio. The bias field also sets the minimum energy of the trapping potential $\mu_{\rm at}B_0$ (called *trap bottom*), which is often expressed in frequency units $\nu_b = \mu_{\rm at}B_0/\hbar$ and corresponds to the minimum Zeeman splitting of the atomic energy levels in the magnetic field. Using the compensation coils, we tune the bias field in order to have always the same trap bottom during a given stage of the experiment, compensating the variation of external fields, as further explained in Sec. 2.6.4.
Using only the lower quadrupole coil, it is also possible to generate a vertical gradient, used to compensate gravity and levitate the atoms when we want to image them after a time of flight $t_{TOF} > 20\,$ms, (see Sec. 2.8).

The high-power coils of Fig. 2.6 are driven by a pair of remotely controlled, stabilized, high power supplies (Delta Elektronica SM30-200), that erogate up to 200 A and are water-cooled by a flow of pressurized water through the hollow core of the copper wire. The coils are connected in series, which means that the current is the same in all of them, suppressing fluctuations in the trap shape. We switch between the different field configurations, in the various stages of the experiment, using fast high-current insulated-gate bipolar transistor (IGBT) switches [Semikron SKM400GAL12E4] and mechanical relays [Kilovac EV200], by means of the circuit shown in Fig. 2.7.
The typical setting time for a 200 A current, used in the initial stage of the magnetic trap, is of the order of 10 ms, limited by the switching time of the relays, while the switch-off time for a current of 50 A, typically used for BEC trapping in the final stages of the experiment, is $\sim 500\,\mu$s, limited by eddy currents.
A more detailed characterization of the magnetic field produced by the coils is given in earlier theses [90, 70, 91].

2.3.1 Gravitational sag

Since the experiments are performed on Earth, when the atoms are confined in the central region of the IP magnetic trap, their total potential energy is determined by the magnetic potential energy of Eq. 2.5, plus the contribution of gravity:

$$U_{|F,m_F\rangle}(x,y,z) = \mu_{\text{at}} B_0 + \frac{1}{2} m \omega_\rho^2 (y^2 + z^2) + \frac{1}{2} m \omega_x^2 x^2 + mgz \tag{2.7}$$

where $g = 9.81\,\text{m/s}^2$ is Earth's local gravitational acceleration. The effect of gravity is to cause a displacement of the minimum of the potential with respect to the minimum of the magnetic field. This shift, commonly known as *gravitational sag*, can be quantified as:

$$z_{\text{sag}} = -\frac{g}{\omega_z^2} = -\frac{g}{\omega_\rho^2} \tag{2.8}$$

The value of the gravitational sag is $z_{\text{sag}} \simeq 24.5\,\mu\text{m}$ for the shallow trapping potential (with trapping frequencies of the order of $\omega_x/2\pi = 8.83\,\text{Hz}$, $\omega_\rho/2\pi = 101.3\,\text{Hz}$) used in Sec. 2.9 and Chap. 3), while it is 13.2 µm in the tighter trap of Chap. 4, where the trapping frequencies are $\omega_x/2\pi = 12.3\,\text{Hz}$, $\omega_\rho/2\pi = 138\,\text{Hz}$.

2.4 Radio-frequency and microwave fields

To couple the different Zeeman and hyperfine sublevels, radiofrequency (RF) and microwave (μw) radiation is used, delivered to the atoms by means of antennas placed in the vicinity of the science chamber (see Fig. 2.5). RF radiation in the MHz range couples the different Zeeman sublevels of the $F = 1$ ground-state manifold, and is used, for instance, during the RF evaporative cooling in the magnetic trap (see Sec. 2.6.3). Such RF signals are generated by means of direct digital synthesizer (DDS) boards, amplified using Minicircuits 2W amplifiers [ZHL-1-2W-S+] and delivered to the atoms by means of ring-shaped (loop) copper-wire antennas, as the one shown on top of the cell in Fig. 2.5, which is used for RF evaporative cooling.

Other, hook-shaped, antennas are instead used to radiate the atoms with microwave radiation at $\sim 1.7\,\text{GHz}$, to couple the $F = 1$ and $F = 2$ ground-state hyperfine levels (see Fig. 2.1). This radiation is obtained by means of a function generator [Marconi 2024 [92]] and amplified using a 100 W amplifier [Minicircuits [93]]. Such high-power amplification for the microwave radiation is required to minimize the effect of the non-homogeneous magnetic field on the transition frequency, when we perform partial-transfer imaging, as described in 2.9. A pick-up antenna is also present to monitor the RF or μw radiation sent to the atoms, by picking up a fraction of the signal, which can be measured on an oscilloscope[1]. To optimize the matching of the antennas at the desired frequency, stub tuners are used in the cases where a high efficiency is critical, such as for the high-power microwave radiation.

2.5 Control of the experiment

Many different instruments are used at the various stages of the experiment, requiring a precise management of the timing and parameters at which each of them is operated. A typical experimental sequence lasts about 50 ms, during which operations need to be

---

[1] In case of μw radiation, which has a frequency outside the bandwidth of the oscilloscope, we observe the beating of the pick-up signal with another known μw signal produced by a second Marconi function generator.

performed in a reproducible way, most of which with a timing precision better than 1 µs. To this scope, most instruments are interfaced to a remote control system, based on field-programmable gate arrays (FPGAs). During my PhD we integrated in the remote control system more instruments, that were before controlled only separately.
The control system is based on a central FPGA [Xilinx Spartan XC3S250E], clocked at 10 MHz, which receives a buffered list of instructions from a computer via USB. Each instruction has a target slave board, identified by its address. The instructions are written by the FPGA on a 24 bit parallel bus, with a time resolution of 100 ns and a maximum instruction-rate of 2.5 MHz. The different boards are:

- Digital boards: each of these boards has 16 independent Transistor-Transistor Logic (TTL) channels, which output a digital $0 - 5$ V signal. They are used as trigger signals to accurately control the timing of IGBT switches, RF and μw signals, laser pulses, camera exposure, data acquisition from oscilloscopes, etc. In practice any instrument that needs to be switched on-off at a precise time, is controlled by a TTL. They are also used to control the motion of moving mirrors and shutters.
- Analog boards: these boards contain two 16-bit Digital to Analog Converter (DAC) chips. They provide control over analog parameters, such as the current generating the magnetic field, which is linearly ramped up and down during the experiment. They are also used to tune the intensity of RF and μw signals through mixers.
- DDS boards: they are used to generate RF signals to drive the AOMs and control the frequency and power of the laser beams, as well as to couple different Zeeman sublevels (see Sec. 2.4 about the RF antennas and Sec. 2.10 on evaporative cooling). Each board has a Direct Digital Synthesizer (DDS) chip [Analog devices AD9958], which outputs RF signals through two independent channels, with frequencies in a range from 200 kHz to 150 MHz, and a power up to 13 dBm. The DDS is programmed through a microcontroller [PIC18F2550], which reads the frequency and amplitude parameters from a look-up-table (LUT) with a 32 bit resolution.

Given the large amount of boards, that need to be connected to the FPGA and are located in different parts of the laboratory, a rather long bus would be needed to ensure all connections. This would cause reliability issues, due to noise pick-up. As a solution, the experiment is actually divided into two parts, located in different places, each controlled by its own FPGA, allowing for a shorter cable. Each FPGA is connected to the control computer via a USB connection. To avoid jitters in the timing, the two FPGAs are triggered by a common signal, given by an Arduino when the communication over both USBs is completed and in phase with the 50 Hz electricity network.

Each experiment consists in a timed list of instructions that is sent to the FPGAs. The list of instructions is written and compiled using a software called *Expcontrol*, developed in Python 2.7 [69] and continuously modified in the course of the years. This software has a high-level user interface to create the timed sequence of instructions. It also allows to set up and control other external devices and instruments that are not directly controlled by the FPGA, such as oscilloscopes, RF signal generators and cameras, giving the possibility to program sequences of experimental runs where different experimental parameters are scanned. In order to optimize the control on an increasing number of instruments, and the execution of multi-parameter scans, in the last few years we partially switched to the Labscript suite [94, 95]. For each experimental run, the instructions, still written and compiled using Expcontrol, are stored together with all the experimental parameters in an HDF5 file [96]. Labscript's *blacs* module allows to supervise and manage the queue of HDF5 files to be executed, changing, if needed, their order and pausing/restarting the execution. It also enables a control of the settings of devices between experimental shots. The various devices are not all connected to the same computer, but instead the instructions are sent via a set of servers, located on different computers in the lab network. At the beginning of each shot, each device's server receives the list of instructions it should execute. At the end of the execution of the program, the output data of the various instruments (cameras, oscilloscopes, sensors, etc) are stored in the same HDF5 file where the program and parameters were saved, making it easy to retrieve all relevant information for each experimental shot. The data can be read and analyzed by means of *ad-hoc* written python scripts. To visualize the data and perform on-the-run analysis during the execution of the experiments, we use the *lyse* tool of the Labscript suite. Thanks to its integration with the *blacs* tool, this program allows to read the single-shot HDF5 files as soon as they are saved to the disk, and provides an efficient way to perform single-shot (on a single HDF5 file) and multi-shot analysis (combining the results obtained for several files). To get a graphical view of the sequence of instructions of a program, we use Labscript's *Runviewer* tool.

2.6 Experimental sequence to produce Bose-Einstein condensates

A typical experimental sequence to produce Bose-Einstein condensates is sketched in Fig. 2.8. After the initial cooling stage in the 2D-MOT and ZS, the atoms are further cooled in a 3D Dark-Spot (DS-MOT) and in a gray molasses (GM) stage. Then RF-driven evaporative cooling in the magnetic trap takes place, eventually leading to the formation of a BEC, for proper choices of the cooling conditions. The final system, is then further manipulated or directly imaged at the desired time, either *in situ* or after a certain time of flight (TOF).

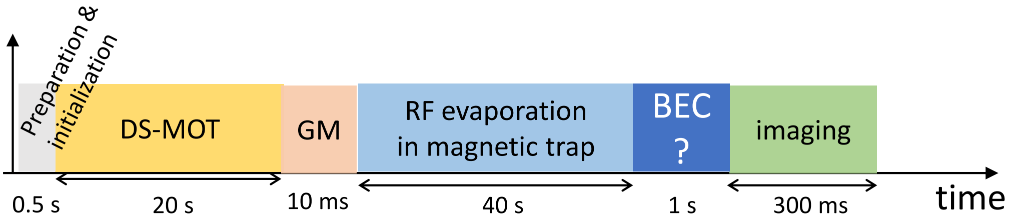

Figure 2.8: Sketch of the different phases of a typical experimental run for the experiments performed in this thesis. An indicative duration of the various stages is indicated, not in scale.

2.6.1 Dark-spot 3D MOT

The atoms are loaded from the 2D MOT, described in Sec. 2.2, in a three-dimensional dark-spot magneto-optical-trap (DS-MOT) [97]. In a standard 3D MOT [98, 99], atoms are cooled and trapped exploiting the combined effect of a magnetic field gradient and three pairs of counter-propagating laser beams with near-resonant, red detuned, frequency and opposite circular polarizations. For alkali atoms, such as ^{23}Na, this mechanism can be implemented using light with a frequency close to the $F = 2 \rightarrow F' = 3$ cycling transition (in red in Fig. 2.1). The relatively small splitting between the $F' = 3$ and $F' = 2$ hyperfine sublevels determines a finite probability for the atoms to end up in $F' = 2$ state, from which they can decay in the dark $F = 1$ ground-state. An additional repumper beam (in orange in Fig. 2.1) is therefore needed to re-cycle the atoms from $F = 1$ to $F' = 2$. In the standard 3D MOT scheme, collective effects, such as light assisted two-body collisions and the re-absorption of already scattered photons, causing an effective repulsive force between atoms, pose an upper limit to the density that can be reached in the central region of the trap and reduce the cooling efficiency. In our dark-spot configuration, instead of sending the repumper light through the same optical path as the six cooling beams, a hollow beam is used, propagating along a single axis in the horizontal plane. Hot atoms are cooled in the outer part of the MOT and drift towards the center, where they are pumped in the dark $F = 1$ state, due to the strong suppression of light-scattering in the absence of repumper light.

In our experiment the magnetic field gradient for the 3D MOT is obtained using the quadrupole coils described in Sec. 2.3, driven with a current of $\sim 10\,\mathrm{A}$, yielding a vertical gradient of about 15 G/cm in the central region of the science chamber, with a zero of the magnetic field near the center. The cooling light is brought from the laser table to the one of the experiment by a single fiber, at the output of which the beam is collimated to a ~ 1 inch diameter. The optical power is then split into three beams using combinations of polarizing beam-splitters and $\lambda/2$ waveplates. These beams propagate through the cell along the three orthogonal directions $[x, y, z)$, in the coordinate system shown in Fig. 2.6 (a)] and each of them is retroreflected by a mirror. The six resulting beams are aligned in such a way to intersect in the region of the cell where the magnetic field becomes zero. $\lambda/4$ waveplates are used to obtain the proper circular polarizations. Some of the mirrors that define the optical path of the 3D-MOT beams are mounted on motorized translational stages, in order to remove them after the MOT phase and make space for the imaging beams, used in the final part of the experiment.

The hollow-profile DS beam is obtained by means of an axicon [Thorlabs AX252-A], that converts a collimated Gaussian beam into a ring, with the highest light intensity at the outer border. Residual repumping light in the central region is further blocked using a disk-shaped obstacle placed in the DS beam path and imaged on the atoms by means of a $f = 150\,\mathrm{mm}$ spherical lens. The optical powers and polarizations of the 3D MOT and DS beams, as well as the radius of the dark region, were experimentally tuned in order to maximize the number of trapped atoms at the end of the 3D MOT cooling stage.

The duration of the DS-MOT stage can be varied in a range from 1 to $\sim 25\,\mathrm{s}$, which changes the final number of atoms. By means of a photodiode, we monitor the fluorescence signal of the bright part of the 3D-MOT, which gives an indication of the loading efficiency. This is used during the alignment and optimization procedures, and serves, as well, as a feedback signal that allows to stabilize the final atom number, by tuning the loading duration until a given fluorescence level is reached.

For a $20\,\mathrm{s}$ MOT loading time, typical atom numbers are of the order of 3.5×10^9 at a temperature $\sim 300\,\mu\text{K}$, corresponding to a maximum phase space density (PSD)[2] of the order of $\sim 10^{-7}$.

2.6.2 Gray Molasses

After the DS-MOT stage, a gray molasses (GM) stage takes place [100]. GM is a sub-Doppler cooling mechanism that combines polarization gradient cooling with the presence of velocity-selective coherent population trapping [101, 102, 103]. The working principle is that the coupling with light is suppressed for already cooled atoms, which get in a coherent dark state, allowing to reach temperatures below the Doppler limit $T_D = \hbar\gamma/(2k_B)$. It exploits blue-detuned light on an $F \to F' = F$ or $F \to F' = F - 1$ transition, contrary to standard laser cooling methods that require, instead, red-detuned light on an $F \to F' = F + 1$ transition. For sodium atoms, it was demonstrated for the first time in our laboratory [100], and a detailed description of the experimental implementation can be found in Ref. [104].
Given the ^{23}Na level structure (Fig. 2.1), the most convenient transition to implement this cooling technique is the D1 line, with cooling light blue-detuned with respect to the $F = 2 \to F' = 2$ transition.

The GM light is produced using the D1 dedicated laser setup [see Fig. 2.2 (b)] and delivered by means of an optical fiber to the experiment table, where it is then superimposed on the 3D-MOT optical path. Repumper light on the $F = 1 \to F' = 2$ transition is obtained generating frequency sidebands in the laser field by means of an EOM, driven at $\sim 1771.6\,\text{MHz}$, the frequency splitting between the two hyperfine ground-state levels at zero magnetic field.

For the GM cooling to be effective, a zero total magnetic field at the atoms is required, since the coherent dark states that are involved are the degenerate Zeeman sublevels of the ground-state manifold. For this reason, after the DS-MOT stage, the magnetic field is switched off, and we further compensate for the environmental magnetic field tuning the current in the bias coils. Right after the magnetic field transients have decayed (a few hundred μs after the switching off of the currents in the coils), the GM cooling light is turned on at maximum intensity ($\sim 150\,\text{mW/cm}^2$), with a blue detuning of 40 MHz, corresponding to $\sim 4\gamma$, with γ the natural linewidth. This first light pulse, lasting only 0.5 ms, has a capture efficiency of about 90% and cools the atomic gas lowering its temperature by a factor ~ 10. The detuning is then increased to 100 MHz and the light intensity ramped to zero in a piecewise way in $\sim 5\,\text{ms}$, further reducing the temperature down to $\sim 6\,\mu\text{K}$, leading to a final number of atoms up to $\sim 3 \times 10^9$, corresponding to a PSD of the order of $\sim 10^{-4}$. The optimum parameters were found experimentally, following the procedure described in Ref.[100].

2.6.3 Evaporative RF-cooling in Magnetic trap

After the GM cooling, to further increase the PSD and reach Bose-Einstein condensation, the atomic sample is loaded in the IP magnetic trap (see Sec. 2.3). This is done in two steps, since a direct loading in the elongated IP trap would be highly inefficient due to the difference in aspect ratio with respect to the isotropic GM. The atomic cloud is first

---

[2] The PSD is calculated as PSD $= n_p\lambda_T^3$, where n_p is the peak density of the atomic cloud, approximated with a Gaussian distribution, and λ_T the thermal De Broglie wavelength of Eq. 1.1

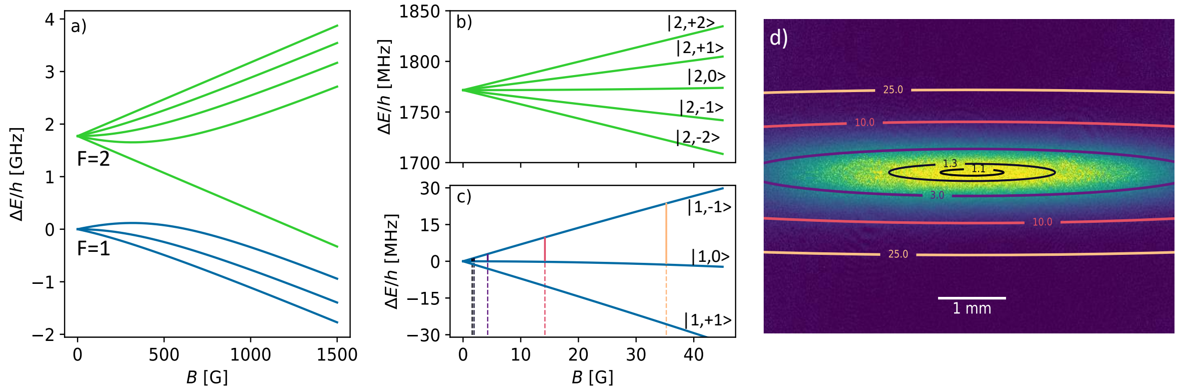

Figure 2.9: Frequency shift of the ground state levels, for high (a) and low (b-c) magnetic field. The frequency shift is calculated with respect to the energy of the $|F = 1, m_F = 0\rangle$ state at $B = 0$, using the Breit-Rabi formula (Eq. 26 in [78]), which includes the Zeeman shift of Eq. 2.1 and the hyperfine structure energy. (d) *In-situ* image of the trapped thermal cloud at an intermediate stage of the evaporation ($\nu_{\mathrm{RF}} \simeq 2.9\,\mathrm{MHz}$, see also Fig. 2.10). The ellipses represent magnetic field isosurfaces, corresponding to decreasing resonance frequencies for the $|1, -1\rangle \rightarrow |1, 0\rangle$ transition, when moving from the outside towards the center: 25 MHz, 10 MHz, 3 MHz, 1.33 MHz, 1.11 MHz (indicated, in MHz, near each curve). The bottom frequency is, also here, 1.076 MHz, corresponding to a minimum field $B_0 = 1.53\,\mathrm{G}$. The shown isosurfaces are obtained for the values of B indicated by same color vertical lines in panel (c).

loaded in a relatively shallow 3D quadrupole gradient at low current. Afterwards, the trap is switched into the IP elongated configuration and compressed by increasing the current to the maximum value of 200 A in a linear way. In this configuration the magnetic field (see Eq. 2.3) is characterized by a bias field $B_0 \simeq 1.5$ G, a gradient $B' \simeq 200\ \mathrm{G/cm}^{-1}$ and a curvature $B'' \simeq 120\ \mathrm{G/cm}^{-1}$ [90, 70].

Being the magnetic trap conservative, a cooling mechanism needs to be exploited to further cool down the cloud and increase the PSD to reach quantum degeneracy. This can be done by means of evaporative cooling. This technique is based on the forced removal from the trap of the atoms with the highest kinetic energy, and on the subsequent rethermalization of the remaining atoms to a lower temperature, induced by atom-atom collisions [28, 98, 105].

In a magnetic trap this can be performed exploiting the inhomogeneous magnetic field, that causes a position-dependent Zeeman shift of the energy levels (see Fig. 2.9). A radio-frequency (RF) field with narrow linewidth can be used to selectively remove atoms from a certain region of the trap, by inducing spin-flipping transitions to untrapped states. Only the atoms with the highest kinetic energy can reach the outer regions where the confining potential is higher (see Eq. 2.1). By applying a RF field resonant with the atomic transition in the most external part of the cloud, it is thus possible to remove only the most energetic atoms. The remaining atoms initially have an out-of-equilibrium velocity distribution, but then thermalize to a lower temperature, through two-body elastic collisions. This procedure can be iterated by gradually decreasing the energy of the RF photons, which has the consequence of lowering the temperature of the system, at the expense of a loss of atoms. If the initial number of atoms and PSD are high enough (hence the need of the previous optical cooling stages), the PSD increases during the evaporation, leading eventually to the conditions for the onset of Bose-Einstein condensation [106, 98].

In our case, RF-forced evaporation is performed by means of a RF field that couples

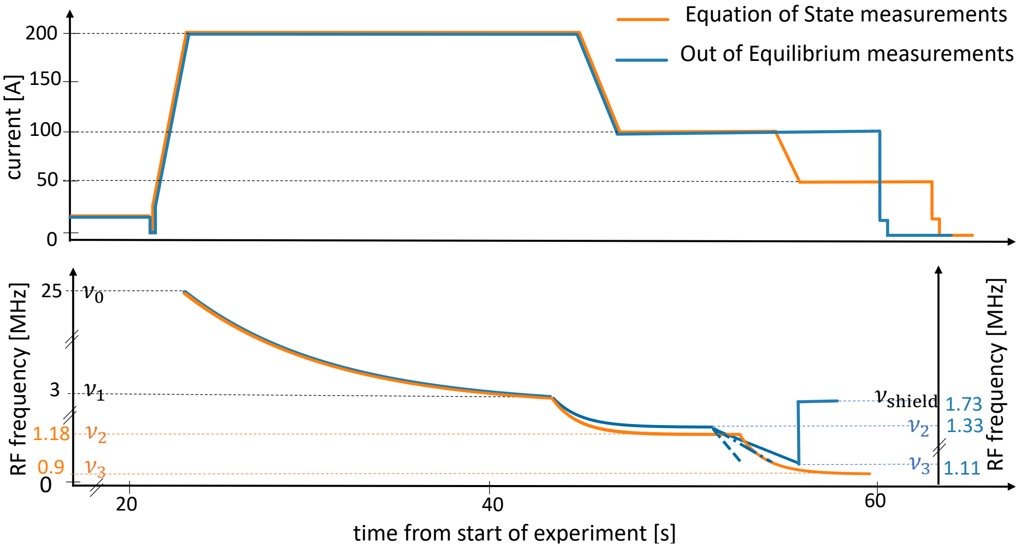

Figure 2.10: Qualitative sketch of the current in the magnetic field coils (top) and RF evaporation frequency (bottom) for the Equation of State measurements (orange) and for the study of the Out of Equilibrium dynamics (blue). The initial part of the experimental sequence is the same, while the last part of the evaporation differs for the two sets of measurements (see text). Shown RF-frequency intervals are not in scale.

the magnetically trapped atoms, in the $|1,-1\rangle$ state, to the untrapped $|1,0\rangle$ state.

To reach the lowest temperatures with the minimum atom loss, an extremely slow evaporation ramp, performed using a very weak RF field, could appear as a good solution, since ideally only few atoms would be removed. However, the evaporation would, in this way, take an extremely long time, causing inelastic three-body loss processes to become predominant [107]. An exponential RF-frequency ramp is a commonly used compromise, since it has a steep derivative, corresponding to a high variation rate of the frequency, in the initial stage, and gradually decelerates when the temperature and the atom number become lower. The initial stages of the evaporation for our experiment were optimized already previously, using exponential ramps [85, 104, 70, 69]. In particular, as shown in Fig. 2.10, an initial exponential evaporation ramp is performed, with a duration of $\sim 20\,$s and a time-constant $\tau_{\rm evap1} = 8\,$s. The RF frequency is decreased from $\nu_0 = 25\,$MHz to $\nu_1 = 3\,$MHz, remaining far above the bottom frequency $\nu_b \sim 1.08\,$MHz. The magnetic trap is then decompressed, by lowering the current in the coils to 100 A, which reduces by a factor 2 the gradient and curvature of the trap. This is done to reduce losses caused by three-body inelastic collisions, whose probability decreases at lower density. The evaporation continues with a second exponential ramp of the RF frequency, with a duration of 12 s and a time constant ranging from 1.4 s to 1.7 s, until a frequency ν_2 is reached, where the temperature is close to the transition temperature T_c.

At this point the experimental sequence becomes different for the two experiments reported in this thesis, as shown in Fig. 2.10.

For the EoS measurements, where a large, partially condensed cloud at equilibrium is required, the magnetic trap is further decompressed, with a decrease of the current in the coils to 50 A and a modification of the bias field to $B_0 \simeq 1$ G, corresponding to a bottom frequency $\nu_b^{\rm EOS} = 0.70\,$MHz. This decompression decreases the magnetic gradient in the trap, making it easier to implement the PTAI imaging described in Sec. 2.9, used for the reconstruction of the *in situ* density profile. The evaporation frequency is then further decreased, as shown in Fig. 2.10, by means of a third slow exponential evaporation ramp (of duration 3 s and time-constant 1 s) to further cool down the system and increase the condensate fraction. After the end of the evaporation, before proceeding with the measurements, the cloud is kept in the magnetic trap for 2 s, in order to ensure full re-equilibration.

For the study of the out-of-equilibrium dynamics, instead, the magnetic trap is kept in the intermediate confinement configuration at 100 A, since the higher density favors two-body collisional processes, making the timescales for the condensate formation process shorter. The bias field is in this case set at $B_0 = 1.53\,\mathrm{G}$ to keep the bottom frequency at $\nu_b = 1.076\,\mathrm{MHz}$ for the whole evaporation. In this case, the second ramp ends at a frequency $\nu_2 = 1.33\,\mathrm{MHz}$, corresponding to a trap depth of about $k_B \times 12\,\mu\mathrm{K}$. At this point, the gas temperature is $T \simeq 1.3T_c$. To study the effect of different cooling rates on the out-of-equilibrium process of condensate formation, the evaporation frequency is ramped down linearly from $\nu_i \equiv \nu_2$ to a final frequency $\nu_f \equiv \nu_3$, at a rate $q = d\nu/dt$. The critical temperature T_c for the onset of condensation is crossed during this ramp, as further explained in Chapter 4.

During the final stage, in which the atomic cloud is kept in the magnetic trap for a certain waiting time to reach its equilibrium condition, one should stop removing atoms via the RF evaporation. This can be done either by setting the amplitude of the RF field generated by the dedicated DDS to zero, or by keeping the RF on, but at a frequency much higher than ν_f. This technique is known as RF-shielding [108] and is used in the experiments of Chapter 4 to keep the total number of atoms constant in time after the end of the linear evaporation ramp, allowing for the study of an, as much as possible, isolated system. In particular, it is desirable to avoid collisions with high energy atoms of the background gas, which would cause heating and removal of atoms from the BEC through three-body collisions. For this aim, the RF frequency is set to $\nu_{\mathrm{shield}} = \nu_f + 400\,\mathrm{kHz}$, creating a resonance surface that is spatially far away from the BEC. This way, high energy atoms, moving towards the center, cross this surface and are transferred to an untrapped state, instead of hitting and heating the central cold cloud.

Depending on the specific program, the evaporation has a total duration between 30 and 50 s, making this stage, together with the DS-MOT loading stage, one of the longest parts of the experimental sequence. To this regard, the study of the out-of-equilibrium processes in the formation of the BEC was motivated also by the necessity of better understanding the physics occurring during the evaporation, with the final aim of developing more efficient evaporation strategies, capable of producing equilibrium condensates with a high number of atoms in a shorter time.

2.6.4 Typical preliminary experimental routines

"Warming up" the experiment Before taking measurements, we proceed with what we call *warm-up* of the experiment. Since the temperature of the magnetic trap coils influences the trap parameters and the cooling efficiency, we need to wait for it to reach a steady state. This process, for our water-cooled coils, takes about half an hour, in which we monitor the temperature of the coils while running continuously the same experiment, where an equilibrium cloud just above Tc is produced in the final magnetic trap. The cloud is imaged in TOF and the number of atoms and temperature are monitored (see

Sec. 2.8). We start with a series of measurements only when these two quantities have stabilized.

Trap bottom scan Another important preliminary measurement is the calibration of the trap bottom, corresponding to the lowest frequency ν_b at which atoms are still removed from the trap. As explained before, this frequency depends on the bias magnetic field B_0 and changes due to the fluctuations of the environmental magnetic fields. Such fluctuations can be caused, for instance, by a different position of magnetic objects in the vicinity of the experiment and by the activities in other laboratories. By making a scan of the current in the bias compensation coils, we find the condition that compensates the variation of the external field, keeping the total bias field - and thus the trap bottom frequency - constant. This provides us with an absolute frequency reference, allowing for comparisons between measurements performed on different days.

In case the trap bottom frequency is particularly critical, as for the measurements reported in Chap. 4, we periodically repeat this scan, interleaving it to the measurement shots, to monitor the eventual variation of ν_b and, if needed, change the compensating magnetic field to keep it constant. This scan also serves as a check to monitor the variation of external fields during the experiment, which can be critical in the case one performs experiments coupling different internal states with microwave fields of low Rabi frequency.

Given the long stabilization time needed for the experiment to reach a steady working condition, we usually let the experiment run continuously when taking measurements, without pausing it after the single experimental run.

2.7 Imaging

This Section deals with the techniques and the experimental setup used to probe the properties of the atomic clouds. This is done in our experiment, like in many others, by imaging the atoms on a ccd camera, using resonant absorption imaging (RAI) techniques [28, 109, 110, 111]. A laser beam resonant with an atomic transition propagates through the atomic cloud, which absorbs a fraction of the light, dependent on the density of the cloud along the beam path. The shadow of the cloud is then recorded on the sensor of a camera, providing information about the optical-density (OD) of the cloud, which is determined by the density integrated along the line of sight.

The imaging procedure is described in detail in Sec. 2.7.4, while here we first focus on the needed optical system.

2.7.1 Optical design of the imaging systems

Different imaging systems in the experiment

To maximize the information that can be obtained by imaging the atomic cloud, a proper system of optics is needed. The typical dimensions of a trapped BEC in our experiment are of the order of a few hundred μm, while those of a cold thermal cloud of the order of millimeters. The dimensions of the sensor of the ccd cameras we use [Allied Vision Stingray F-201 [112]] are 1624 × 1234 pixel, with a pixel-size of 4.5 µm, corresponding to an area of approx. 7.3 × 5.5 mm. Different needs of magnification thus arise, depending on the stage of the experiment at which the atomic cloud is imaged, and whether it is imaged *in situ* or after a time-of-flight expansion.

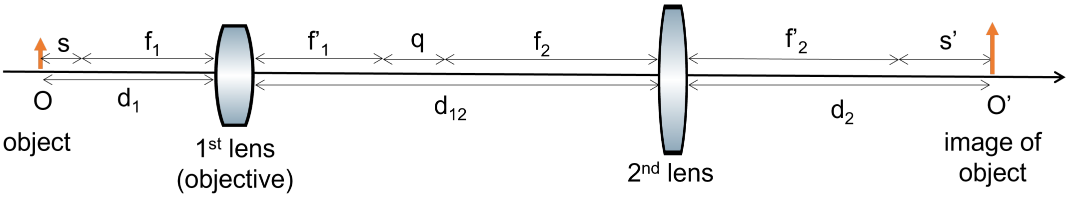

Figure 2.11: Two-lens imaging system. f_1 and f_1' are the front and back focal points of the first lens, used as objective, and f_2, f_2' of the second. O is the axial object positions and O' the axial image position.

To obtain the desired magnification and an in-focus image of the atomic cloud on the ccd, a common solution is provided by an optical system made of two lenses, as shown in Fig. 2.11. Considering the general case in which the thin lens approximation does not necessarily hold, a front and a back focal length characterize each lens : for the two lenses of figure 2.11 they are $f_1(f_1')$ and $f_2(f_2')$, respectively. In case the two lenses are placed at a distance $d_{12} = f_1' + f_2$ equal to the sum of their focal lengths, an object, placed at a distance $d_1 = f_1$ from the first lens, will produce a focused image at a distance $d_2 = f_2'$ from the second lens, with a nominal magnification determined by

$$M_0 = f_2'/f_1. \tag{2.9}$$

In the thin-lens appproximation, this is simply equal to the ratio of the two focal lengths. More in general, considering an object at a distance $d_1 = f_1 + s$ from the first lens, with the two lenses placed at a distance $d_{12} = f_1' + f_2 + q$, a focused image of the object is obtained at a distance $d_2 = f_2' + s'$ from the second lens, with q, s, s' being related by:

$$q = \frac{f_1 f_1'}{s} + \frac{f_2 f_2'}{s'}, \tag{2.10}$$

In this case the magnification is given by [113]:

$$M = M_0 \frac{1}{1 - \frac{sq}{f_1 f_1'}} = M_0 \left(1 - \frac{s'q}{f_2 f_2'}\right) \tag{2.11}$$

In practice, we work with imaging systems in a nearly afocal configuration, where the distance of the first lens from the atoms is approximately equal to its front focal length f_1, and the distance between the two lenses is equal to the sum of the two focal lengths $f_1' + f_2$. The position of the camera, roughly at f_2', is then adjusted to bring the image of the atoms at focus on the camera plane, eventually correcting also the position of the second lens, if needed. We therefore design the imaging systems considering the nominal magnification, and afterwards measure it experimentally.

Besides the magnification, the design of the imaging system has to take into account also the resolution, which determines the smallest size of spatial features that can be seen in the atomic cloud. In particular, the optical quality and numerical aperture of the first lens, used as objective, are particularly critical.

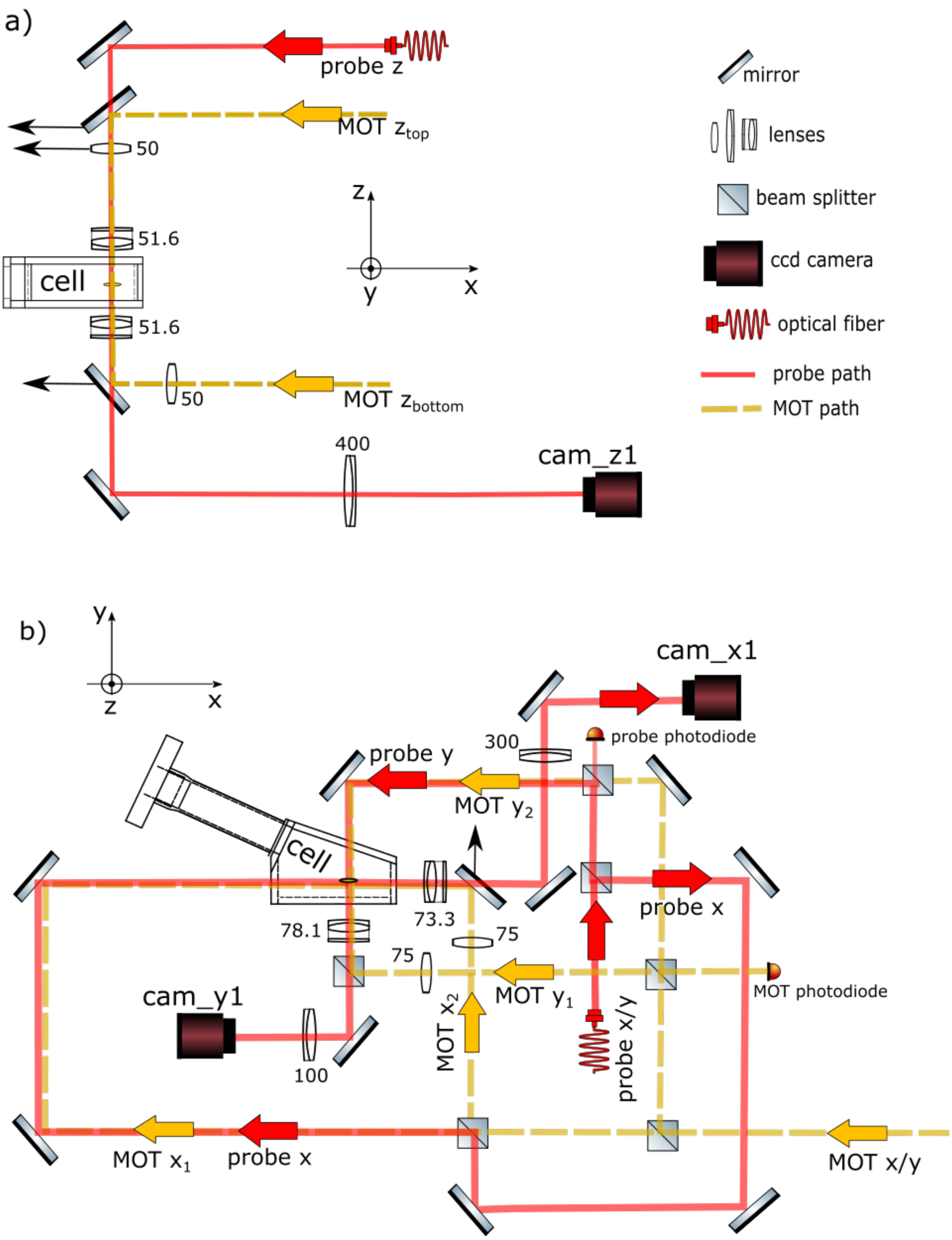

Figure 2.12: Scheme of the new imaging optical setup for probing the atomic distribution along the three orthogonal directions: (a) z imaging system, viewed from the side. (b) x and y imaging systems, viewed from above. The probe paths are shown as solid red lines, while the MOT beam path, sharing part of the optics, is represented in dashed yellow. Optics with a black arrow get removed after the MOT stage, leving space for the probe beams to propagate. Focal lengths of lenses are reported in mm. Waveplates, used to obtain the desired light polarizations, are not shown in the drawing for visual clarity.

For an ideal, aberration-free, lens of focal length f and aperture diameter D, the resolution is determined by the diffraction limit, which can be expressed by the radius of the Airy disk [114, 115]:

$$R_{\text{Airy}} = 1.22\frac{\lambda f}{D}. \tag{2.12}$$

R_{Airy} corresponds to the minimum spot-size to which a light beam can be focused using that lens. It is defined as the position of the first local minimum of the diffraction intensity profile, from the center of the optical axis, as shown in Fig. 2.13, where a comparison with the width of a gaussian profile is provided.

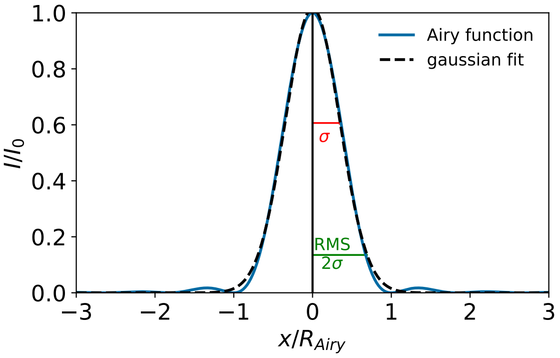

Figure 2.13: Intensity profile of an Airy function (blue solid line), normalized to the peak intensity I_0. The Airy disc radius R_{Airy} is defined as the position of the first zero of the intensity profile. The dashed black line is a fit to a gaussian function, of which the width $\sigma \simeq 0.345 R_{\text{Airy}}$ and $R_{\text{RMS}} = 2\sigma$ are reported.

The above is valid for an ideal lens. Optical aberrations can, however, further degrade the resolution, making the actual minimum spot size larger. In particular, the imaging system that was previously used to image the atoms along y, which was used also for preliminary measurements of the *in situ* density distribution to extract the equation of state [85], had a rather poor resolution, mainly caused by optical aberrations due to the presence of the thick, oblique window of the science chamber (see Fig. 2.4b) on the imaging optical path and by the geometrical aberrations of the achromatic doublet lens that was used as objective [Thorlabs AC254-075-A, f=75 mm]. Figure 2.14 shows the simulated spot diagram for this setup. The asymmetric shape is caused by the tilted glass window. Other imaging systems with not much better resolution were present in the other directions.

We redesigned the imaging systems of our experimental apparatus to let the probe beams for all three directions propagate perpendicularly through the science chamber windows, after passing through the atomic cloud (see Fig. 2.12). Three imaging systems are present, one for each direction, with different magnifications determined by the different experimental needs. The three corresponding ccd cameras are called `cam_x1`, `cam_y1` and `cam_z1` [3].

Regarding the resolution, according to Eq. 2.12, for equal lens diameter, the Airy disk size is lower for decreasing values of the focal length. We therefore designed the imaging

---

[3] Additional cameras, indicated with a number 2, have also been implemented in the experiment, allowing for different magnifications along the three imaging directions, but are not used in the measurements reported in this thesis, and therefore omitted from the optical scheme

systems in order to minimize the distance of the objective from the atoms, compatibly with the existing setup and in particular with the coil mounts that surround the cell. Since the geometry of the magnetic trap yields an ellipsoidal shape for the trapped atomic cloud, with cylindrical symmetry around the x axis, the y and z direction are fundamentally equivalent, from a geometrical point-of-view, for probing the atomic distribution along the elongated direction.

The z direction offers, between the two, the best optical access and the advantage that the upper and lower surfaces of the cell are parallel. Given the presence of the mechanical mounts holding the coils, we can place 1 inch optics at a minimum distance of about 20 mm with respect to the glass surface, both above and below the cell, corresponding to a distance of ~ 37.5 mm from the center of the atomic cloud *in situ*. We therefore place the imaging system for probing the atoms in situ along the vertical direction, with the probe propagating from top to bottom, perpendicular to the cell, and being finally collected by `cam_z1`, after its propagation through the atoms and the optical system that is described more in detail below. This imaging system has been used to obtain the density profile for the EOS measurement.

To image the atoms after a TOF expansion, we use a probe beam propagating along the horizontal y direction, since this allows to keep the atomic cloud at focus even when it falls along z in case gravity is not compensated by a magnetic levitation gradient. To reduce the aberrations, we let the probe beam enter through the oblique window, and exit perpendicularly to the other side of the glass cell, where the imaging system is placed, with the light being collected by `cam_y1`. Since this system is generally used to image the atoms after a TOF expansion or to monitor the MOT, it is designed with a low magnification $M \sim 1$. This imaging system has been used for the study of the out-of-equilibrium processes and to extract the temperature for the EOS measurement.

Another camera `cam_x1` is placed along the x direction, to image the radial distribution of the cloud. It was so-far used mainly for alignment purposes. The presence of the coil mounts does not allow to place optics closer than ~ 40 mm from the glass window in this direction, limiting the achievable resolution.

The objectives close to the cell have a 1 inch diameter (25.4 mm) due to geometrical constraints. The mirrors placed afterwards all have a diameter of 2 inch, chosen in order to avoid further degradation of the resolution due to smaller apertures. The design of the objective of the imaging setup is thus the most critical part in order to have a good resolution.

Design of a composite objective

The main challenge regarding the objective of the imaging system, is that optical aberrations strongly limit the resolution for standard commercially available lenses of short focal length, resulting in a non-diffraction limited performance. For this reason, many ultracold atom experiments are equipped with expensive microscope objectives, with resolutions below $\sim 1\,\mu$m. Given also the lack of space to accomodate large optical systems, we decided to build a simple and cost-efficient objective based on the combination of two standard, commercially available, lenses. The first is an achromatic doublet with a short focal length, close to the desired effective value. A plano-convex lens of long focal length is then added at a proper distance, with the aim of correcting for most optical aberrations of the first lens. A similar design, with the combination of four lenses, is presented in Ref.

[116]. Later, another study appeared demonstrating an excellent resolution for a different two-lens objective [117], built with ad-hoc manufactured lenses.

To design and simulate our objective, I used the program OSLO-EDU [118], which allows for directly importing lens data from several commercial catalogues and simulating the effect of a series of optical surfaces and apertures on the propagation of a laser beam[4]. The problem was treated from the reverse point-of-view, considering a collimated input laser beam and minimizing the dimensions of the spot to which the beam can be focused by the optical system. The degrees of freedom in this optimization were the focal lengths of the two lenses composing the objective and their relative distance. They were changed in an iterative way, looking for the combinations that minimized the geometrical RMS size of the spot diagram in the focal point. This RMS size is computed by OSLO considering the input beam as composed of a tunable number of uniformly distributed light rays, for each of which the propagation through the optical system is evaluated. In the focal plane, the squared distance with respect to the optical axis (on which the optics are centered) is calculated for each ray and the average over all rays is then taken to obtain the RMS size. As an input beam, a collimated gaussian beam with a 5 mm waist was chosen, with an input aperture diameter of 25 mm, slightly smaller than the optics nominal aperture of 1 inch. Up to 200 light rays were considered to increase the accuracy of the simulations. Also the presence of the 5 mm thick quartz window, with the inner surface at 12.5 mm from the desired focal plane, was taken into account in the simulations. Due to mechanical constraints, that do not allow for placing optics closer than $\sim$ 20 mm from the cell's external surface, the minimum effective focal length that can be used for the objective is $\sim$ 50 mm.

Simulations were performed comparing different combinations of lenses, placed at variable distance, for identical input conditions. Figure 2.14 provides a comparison between (a) the old setup used for imaging along y, through the tilted cell window, (b) a single $f = 50\,\mathrm{mm}$ achromatic doublet and (c) the composite objective that we decided to implement for imaging along z. For each setup, from top to bottom, the figure shows: a set of 20 incoming rays propagating through the optical setup; the geometrical spot diagram, composed by the intercepts of 200 incoming rays like the above with the focal plane; the 3D point-spread-function (PSF), computed by means of a Fast Fourier Transform (FFT); a cut of the PSF through the global maximum, along the two axis in the focal plane. The focal plane was obtained as the plane perpendicular to the optical axis on which the RMS spot size is minimized.

The optical performance of the setup can be qualitatively evaluated comparing the value of the geometrical RMS spot size R_{RMS} with the diffraction limit expressed by the Airy disc radius R_{Airy} of an ideal system, with the same effective focal length and input illumination conditions. If the lens-system has a performance close to the diffraction limit, $R_{\mathrm{RMS}} \leq R_{\mathrm{Airy}}$ and most of the ray intercepts in the spot diagram fall within the Airy disc radius, represented by a solid black circle in the spot diagrams of Fig. 2.14. If, instead, a large fraction of the ray intercepts falls outside the Airy disc, it means that optical aberrations are not negligible, determining an effective spot size larger than the ideal one. The values of R_{RMS} and R_{Airy} are reported on the left of each spot diagram. Another quantity that gives a measure of the quality of the actual optical system, in comparison

---

[4] The EDU version of OSLO puts a limitation of 10 on the maximum number of optical surfaces that can be simulated simultaneously, which was exactly enough for the system composed of the two-lens objective and the quartz cell.

1^{st}lens (achromatic)	2^{nd} lens (spheric)	d_{lenses}	d_{focus}	EFL	NA	R_{Airy} (μm)	Strehl ratio	used for
$f = 60$	$f = 300$	8.9	45.4	51.6	0.24	1.6	0.69	z imaging
$f = 75$	$f = 400$	1	58.2	63.6	0.21	1.7	0.76	DMD
$f = 75$	$f = 300$	3.2	56.9	60.9	0.21	1.6	0.73	BEC2
$f = 100$	$f = 400$	8.5	78.1	81.9	0.15	2.4	0.85	y imaging
$f = 100$	$f = 300$	3	73.3	76.1	0.16	2.2	0.80	x imaging

Table 2.1: Simulated combinations of (near) diffraction limited two-lens objectives. Distances are in mm if not specified. All lenses, from Thorlabs catalogue, have a diameter of 25.4 mm and a slightly smaller clear aperture when mounted. The first lens, an achromatic doublet, is the closest to the atoms, as in Fig. 2.15. The other lens is a plano-convex spheric lens. The distance between the two lenses d_{lenses} and the front focal distance d_{focus} (corresponding to the optimal distance to the atoms) are defined from the central point of the closest external optical surface of each lens. The center of the atomic cloud is at ~ 12.5 mm from the internal surface of the 5 mm thick quartz window of the cell. The optimum positions of both lenses have been adjusted in an iterative way, in order to minimize the simulated RMS spot size to which the input beam is focused. Since the objective is definitely not a thin lens, the distance of its closest surface from the atoms is much smaller than the EFL.

to the ideal diffraction-limited one, is the Strehl ratio, defined as the ratio between the PSF peak intensity of the actual system and the peak intensity for the corresponding diffraction-limited system. Values of the Strehl ratio > 0.5 indicate that most wavefront aberrations are corrected [119]. The Strehl ratio is reported on the right of each PSF for the three optical systems we are comparing.

In Fig. 2.14 (a) we observe that if the light propagates through the oblique cell window, the spot diagram becomes asymmetric, with an extension much larger than the Airy disc size. The corresponding PSF also has an asymmetric profile, with a rather low Strehl ratio. The optical performance improves when the light propagates perpendicularly to the quartz window, as shown in (b) and (c). A single achromatic doublet with a focal length of $f = 50$ mm (b) still performs worse than the diffraction limit, as can be noticed from the dimensions of the spot diagram and from the quite low Strehl ratio, mainly due to the fact that a relatively high fraction of the total energy ends up in the secondary maxima of the PSF. A composite objective with similar effective focal length $f = 51.6$ mm is shown in (c), composed by a 60 mm achromatic doublet [Thorlabs AC254-060-A] and a 300 mm plano-convex spherical lens [Thorlabs LA1484-A], placed at a relative distance of 8.9 mm (measured between the centers of the two closest surfaces). In this case the optical performance is close to the diffraction limit, with the simulated RMS spot size ($R_{\text{RMS}} \simeq 1.6\,\mu$m) approximately equal to the Airy disk size, and with a Strehl ratio of ~ 0.7, meaning that the actual minimum spot size will be slightly larger, but still of the same order as the Airy disc radius. The actual resolution has been measured experimentally (see below).

This composite lens-system has been selected as objective for the z imaging system and also as last lens for the setup that will be used to project, on the atoms, light patterns created with the DMD (see Sec. 2.7.2).

Also other pairs of lenses (see Table 2.1) that I simulated yield good results, and have been chosen as objectives for the other imaging systems and for the DMD setup, as well as for the imaging system in the neighbouring laboratory (BEC2), hosting a similar experiment [120, 121].

I performed analogous simulations also for the lens used to focus the image of the atoms on the camera (2^{nd} lens in the scheme of Fig. 2.11), finding that achromatic lenses with focal length $f_2 \geq 300$ and a 2 inch diameter aperture are all good choices, since

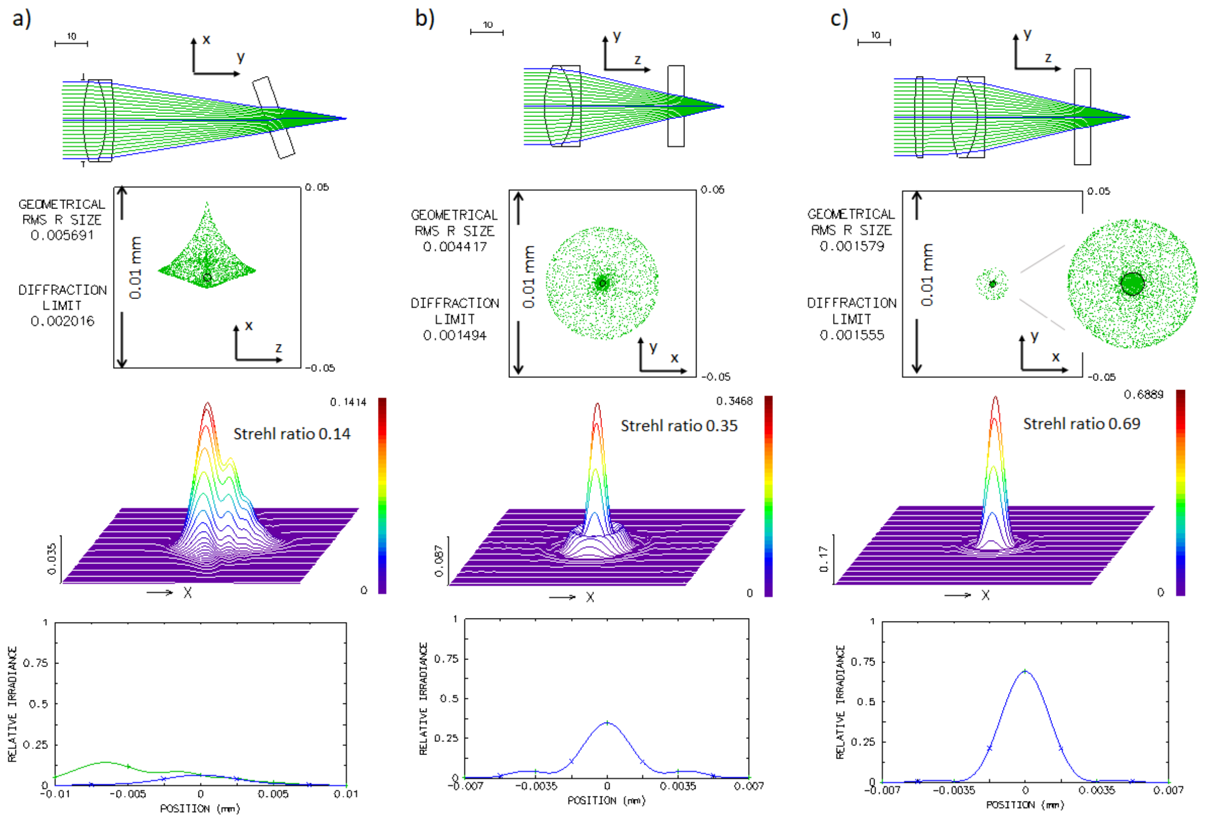

Figure 2.14: OSLO simulation of different optical systems: (a) the previous optical system used for imaging along y, through the oblique surface of the cell window (tilted rectangle in the top panel), (b) a 50 mm achromatic doublet [Thorlabs AC254-050-A], considering an imaging path perpendicular to the cell window (c) the final objective used for the z imaging, composed by a 60 mm achromatic doublet and a 300 mm plano-convex lens, with the light propagating again perpendicularly to the cell window. From top to bottom the panels show, for each lens: (top) propagation of 20 (out of a total of 200) geometrical light rays propagating through the system, (second row) spot diagram obtained from the intercepts of the 200 input rays with the focal plane, with the geometrical RMS size and Airy disc radius (in mm) reported on the left, (third row) three-dimensional PSF, with the Strehl ratio (corresponding to the relative peak amplitude) reported on the right, (bottom) 2D cut of the PSF through its global maximum, along the two coordinate axis in the focal plane. All distances are in mm.

optical aberrations are almost negligible and the simulated RMS spot size is well below the diffraction limit. The minimum spot size is thus given directly by the Airy disk radius, which is ~ 4.2 mm in the case of the $f = 300$ mm lens. The second lens does therefore not limit the resolution further, since in the image plane a higher limit to the minimum size of resolvable spatial features is determined by the camera pixel-size of 4.5 µm[5].

I tested the various combinations of lenses on a separate optical table, as shown in Fig. 2.15. The two lenses that compose the objective are placed at the simulated relative distance in a cylindrical optics-holding tube [Thorlabs SM1L10]. Cage systems [Thorlabs [122]] are used, aiding the optical alignment and improving the mechanical stability of the setup. As a test object, I used a microscope-calibration plate, shown in Fig. 2.15 (a), with a ruler with sharp-edged ticks distanced by 100 µm one from the other. The camera is the same Stingray camera used in the main setup and a second lens, analogous to that

---

[5] This is a limit to the dimensions of the smallest features that can be distinguished in the image. For the magnification of the z imaging system ($M \sim 8$), such dimensions would correspond to a minimum size at the atoms of ~ 0.55 µm, much below the resolution of the objective.

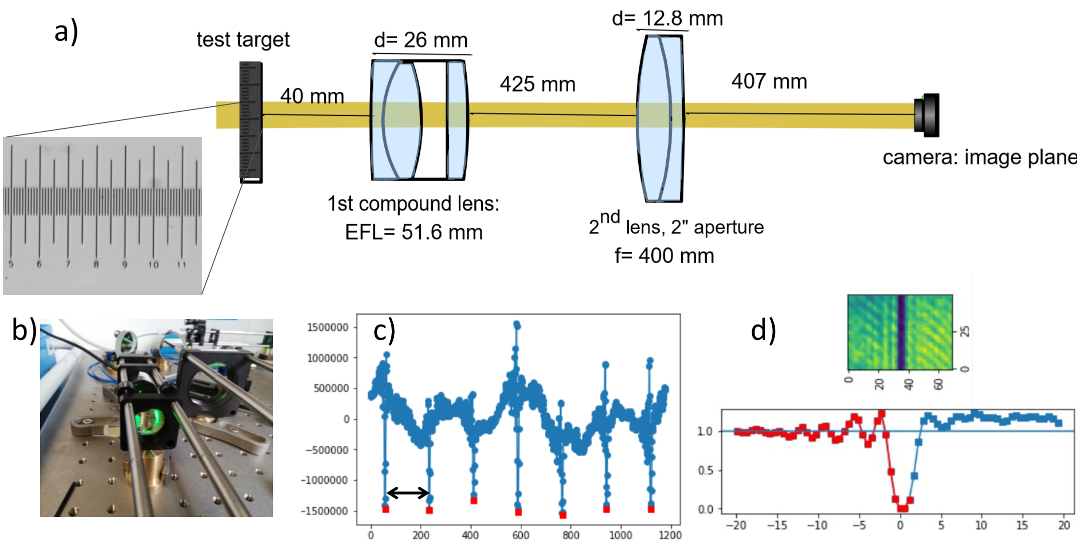

Figure 2.15: (a) Scheme of the optical setup to test the resolution of the imaging system. (b) Photograph of part of the test setup. (c) Magnification measurement. We find the average distance on the camera between the negative peaks of intensity, corresponding to the lines of the ruler on the microscope plate (the distance marked by the arrows is 177 pixel, corresponding to 780 µm). Knowing that the ticks are at a distance of 100 µm, we find the magnification of the tested imaging system to be $M \sim 7.8\,\mu\text{m}$. (d) Resolution measurement. From the measurement of the average width, in the image, of the edges of the sharp lines on the target, we estimate the actual Airy disc size.

of the z imaging system (400 mm 2 inch Thorlabs achromatic doublet), is used to focus the image of the target on the camera. The composite objective and this second lens are placed in a nearly afocal configuration, as shown in Fig. 2.15 (a). The presence of the ruler on the test target allows for a simultaneous measurement of both the magnification and the resolution of the system. The setup was tested using both green laser light at $\lambda = 532\,\text{nm}$ and the yellow probe light at $\lambda = 589\,\text{nm}$.

For the magnification measurement, we compared the relative distance between the intensity dips corresponding to the lines of the ruler, measured on the image from the camera, with the actual distance of 100 µm between the lines, as shown in Fig. 2.15 (c). We measured a magnification of $M = 7.8$ which corresponds very well to the nominal magnification of the equivalent thin-lens system $M_0 = f_2/f_1 = 7.79$, calculated using as value for f_1 the simulated effective focal length (EFL) of the two-lens objective.

The finite resolution is responsible for smearing out the sharp edge of each side of the ruler ticks, as shown in Fig. 2.15 (d). The resulting profile was fitted to a knife-edge distribution [116]. The fitted width corresponds to an Airy disk size of $R^{\text{meas}}_{\text{Airy}} = 2.3(1)\,\mu\text{m}$, not much above the simulated value and considerably smaller than the resolution limit of the previous setup.

2.7.2 Optical system for a Digital Micromirror Device

Although not-directly related with the measurements presented in this thesis, in this section I would like to briefly describe the optical setup that I built with the aim of using a Digital Micromirror Device (DMD) in our experimental apparatus. This device will be used in future experiments to produce tunable optical potentials by projecting the corresponding light-patterns on the atomic cloud. The DMD optical setup was tested and built at the same time of the imaging system and includes similar composite lens systems.

Working principle of a DMD

A DMD is an electronically controlled optical device composed by a 2D array of micromirrors, each of which can take two different angular positions, corresponding to an "on" or "off" state, respectively, as shown in Fig. 2.16. The DMD implemented in our experimental apparatus is the Texas Instruments DLP7000 [DLP 0.7 XGA 2xLVDS Type A DMD [123]], which is equipped with a 1024 × 768 array of aluminum micrometer-sized square mirrors, each of which has a 13.68 µm edge and can be tilted by ±12°, to obtain the "on" and "off" positions. The integrated control board, connected to a computer, can be loaded with sequences of binary images, where the status of each mirror can be controlled independently, providing the possibility of designing any arbitrary binary pattern and of changing the patterns dynamically acting on the timing of the sequence of images. Illuminating the DMD with a laser beam of large area, it is in this way possible to create arbitrary light patterns corresponding to the designed binary patterns, as shown in Fig. 2.16 (b).

Using far detuned laser light, it is this way possible to produce tailored optical dipole potentials [84, 124, 125, 126, 127], that can be changed dynamically by sending to the DMD a sequence of different patterns with the desired timing, opening the way to a wide range of possibilities of controlling and manipulating the ultracold atoms. For instance one can create a repulsive barrier moving through the BEC at a controllable speed, or induce local changes in the potential confining the atoms.

Design of Optical system

A sketch of the optical setup that I designed to use the DMD in our experiment is shown in Fig. 2.18 a), while b) shows a photograph of the experimental table after the implementation of the DMD and of the new imaging systems.

The optical setup for the DMD was developed keeping in mind a few requirements. It was designed planning to use laser light with two different wavelengths, blue-detuned 532 nm and near resonance 589 nm light, coming from two different fibers [green and yellow in Fig. 2.18 (b)], and propagating along two different initial paths, which are combined on a first polarizing beam-splitter. Part of the yellow light is directly sent to the atoms without passing through the DMD, and is used as z probe beam.

The input light beam that illuminates the DMD should be collimated and have a sufficiently large area to uniformly illuminate the whole DMD surface. After collimating the laser beam at the fiber output, the lenses L1 and L2 in Fig. 2.18 (a) are used to further increase the spot-size to illuminate the whole DMD with sufficient intensity. Since a gaussian laser beam is used, when designing the DMD patterns, we will need to take into account the reduced illumination near the corners.

The mirrors of the DMD tilt by $\theta_{\mathrm{tilt}} = \pm 12°$ around their diagonal: in order to let the reflected light propagate in the same horizontal plane of the incident light, the device is mounted with a 45° rotation angle with respect to the optical table surface, as shown in Fig. 2.16.

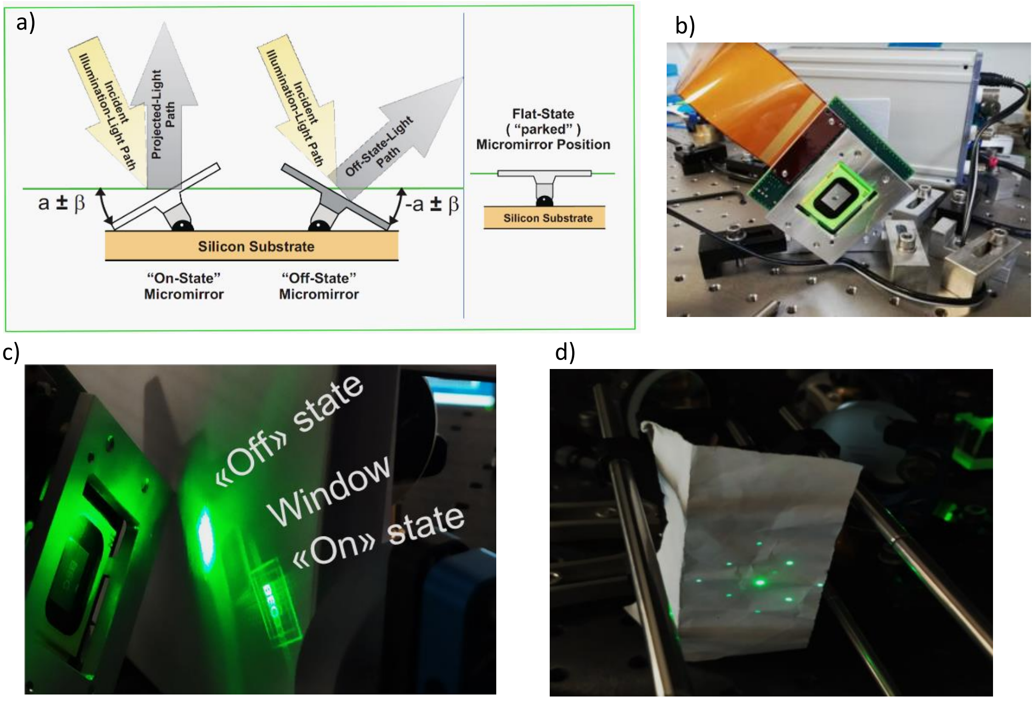

Figure 2.16: (a) Working principle of a DMD (adapted from Ref. [123]). (b) Photograph of our DMD, which is mounted with a 45° tilt with respect to the horizontal plane of the optical table. (c) The DMD is here projecting a pattern that forms the word BEC. The "off" mirrors, which are the majority in this case, project the "negative" pattern. Also the specular reflection from the glass window that protects the DMD surface is visible. Multiple copies of the projected pattern can be seen on the sides, corresponding to different diffraction orders. (d) The different diffraction orders become spatially well separated after propagating for a long enough optical path. The unwanted order are blocked placing an iris in the position of the piece of paper in this photograph, after lens R1 of Fig. 2.18.

One has, moreover, to consider that the DMD is not a single reflecting surface, but an array of micro-meter size mirrors, which determines a behavior similar to that of a 2D reflective diffraction grating, with the incoming light being reflected in a multitude of diffraction orders, as shown in Fig. 2.16 (c). This can be a disadvantage for our applications, since it distributes the optical power over many directions of propagation, while only one is used on the atoms. However, one can maximize the output power on a single selected diffraction order by finding the angle θ_i of the incident beam that satisfies the *blazing* condition. This occurs when the peak of the intensity envelope due to the single-mirror diffraction, at an angle $\theta_r = -\theta_i + 2\theta_{\mathrm{tilt}}$ with respect to the normal to the DMD surface (where $\theta_{\mathrm{tilt}} = 12°$ is the tilt of the mirrors in the position considered as "on"), overlaps with the angular position θ_m of a single diffraction order m. The latter satisfies the grating equation $\sin\theta_i + \sin\theta_m = m\lambda/d$ (where λ is the laser wavelength, m the diffraction order of interest, $d = 13.68\sqrt{2}$µm the size of the micromirrors along the diagonal). The blazing condition for a given order m can then analytically be expressed as a function of the angle of incidence [128]:

$$\sin(\theta_i) + \sin(-\theta_i + 2\theta_{\mathrm{tilt}}) - \frac{m\lambda}{d} = 0. \tag{2.13}$$

The values of θ_{in} satisying this condition for various diffraction orders m correspond to the intercepts with $y = 0$ of the curves in Fig. 2.17, which have been computed for the

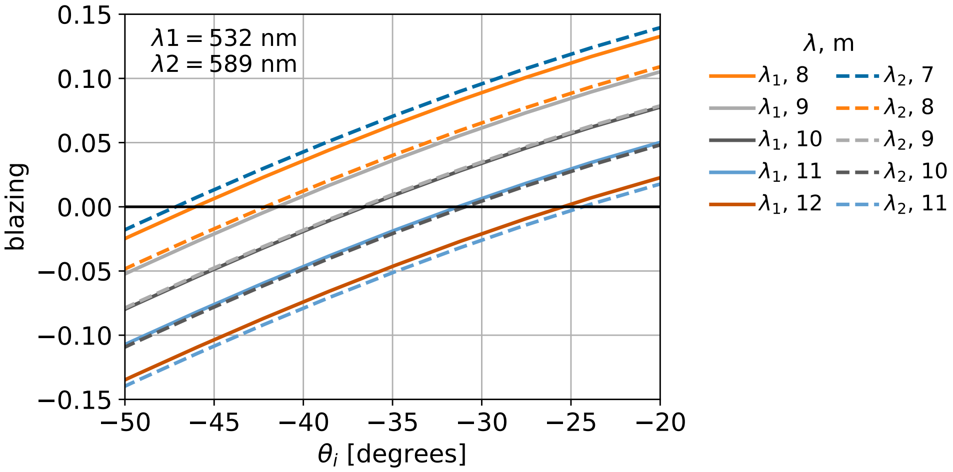

Figure 2.17: Blazing condition for a few diffraction orders m for the two different wavelengths: $\lambda_1 = 532\,\mathrm{nm}$ and $\lambda_2 = 589\,\mathrm{nm}$.

two wavelengths of interest ($\lambda_1 = 532\,\mathrm{nm}$, $\lambda_2 = 589\,\mathrm{nm}$). For an input angle $\theta_i - \sim 36.6°$, corresponding to an output angle $\sim 12.6°$, a near-blazing condition can be found for both wavelengths, exploiting the $m = 10, 9$ diffraction orders, respectively (solid dark gray and dashed light gray curves).

In practice, after placing the optics at roughly the calculated angle, the blazing condition is experimentally found, for each wavelength, by tuning the incidence angle to maximize the power in the desired diffraction direction. We were able to reach a $\sim 70\%$ diffraction efficiency on a single diffraction order for each wavelength. The other orders are blocked after spatially separating them by means of a long enough propagation. Also the reflection of the protective glass window of the DMD and the light corresponding to the "off"-state mirrors (see Fig. 2.16) are properly blocked.

To control the angle and position of the input beam, two mirrors are placed right before the DMD on the optical path. Two additional mirrors on the laser path, placed before the beam splitter that combines the two wavelengths, allow for small corrections to the incidence angle to achieve the blazing condition for both wavelengths. Two further mirrors after the DMD control the direction of propagation of the selected order output beam, sending it through the center of the lenses in the following part of the setup.

Another point to consider in designing the optical system for the DMD is the necessity of demagnification: we want to image the DMD light pattern onto the atomic cloud, which has typical dimensions of the order of 300 µm in case of a trapped BEC, while the length of the horizontal diagonal of the DMD (tilted by 45°) is 17.5 mm. We intend to fully illuminate the whole BEC with the DMD light pattern, and at the same time make sure that the projected dimensions of a single DMD pixel on the atoms plane are much smaller than the optical resolution, in order to design smooth potentials, avoiding effects due to the discrete nature of the pixels. To achieve this, a relay optical system is present, composed of two telescopes approximately in afocal configuration, made by the lenses R1, R2 and R3, R4, whose specifications are reported in the caption of Fig. 2.18. The second telescope is nominally identical to the one used for imaging the atoms along the z direction, with a demagnification of ~ 7.78. Together with the first system, having a demagnification of

~ 4.68, this provides a total demagnification of $M_{\text{relay}} \simeq 36.4$, allowing to project light patterns on the whole BEC, without an excessive waste of optical power. Irises placed in the Fourier planes of the two telescopes can be used, if needed, to place a cutoff on the maximum spatial wavevectors of the light patterns, washing out sharp features to create smoother patterns [129, 130]. When all the irises are opened at maximum aperture, the resolution of the relay optical system corresponds to an Airy disc radius of $\sim 2\,\mu\text{m}$, equivalent to ~ 5 DMD pixels, and is mainly determined by the diffraction limit of the two compound lenses of short-focal length. The resolution was first tested using the same test setup used for the imaging system, with the microscope calibration target as reference, as well as by finding the minimum detectable size of few-pixel patterns projected by the DMD.

2.7.3 Implementation in the experiment

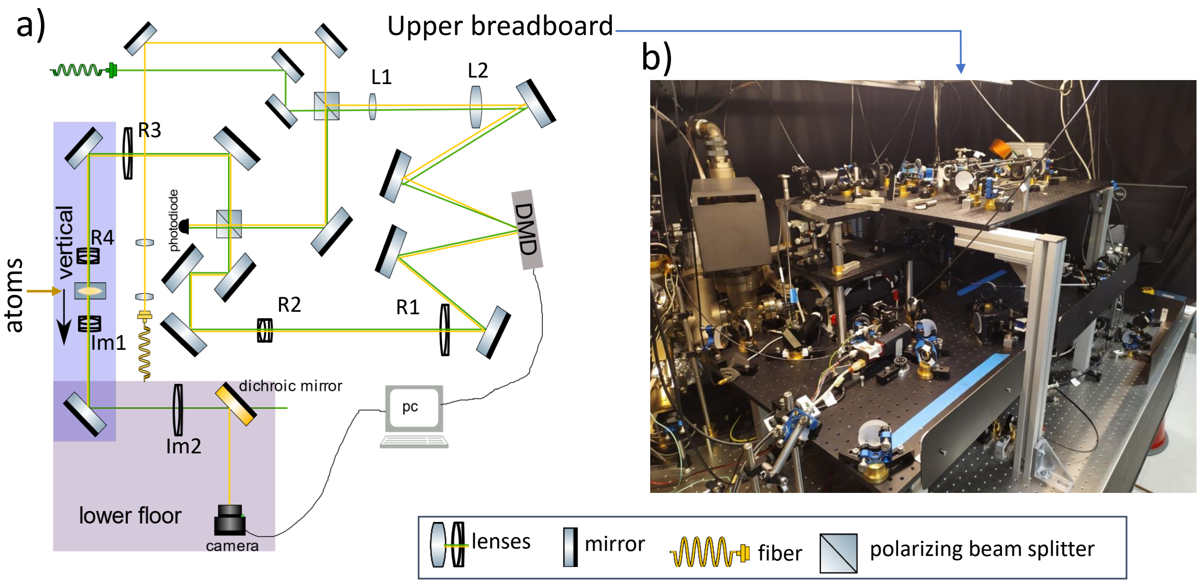

Figure 2.18: Optical setup for the DMD: scheme (a) and photograph of its implementation (b). The lenses L1 ($f = 30\,\text{mm}$) and L2 ($f = 150\,\text{mm}$) are used to obtain a collimated input beam with large area, to illuminate the whole DMD, the lenses R1 ($f = 300\,\text{mm}$ 2 inch achromatic doublet), R2 (EFL $= 63.5\,\text{mm}$, 1 inch, compound lens, see Tab. 2.1), R3 ($f = 400\,\text{mm}$, 2 inch, achromatic doublet), R4 (EFL $= 51.7\,\text{mm}$, 1 inch, compound lens, see Tab. 2.1) form the relay system used for imaging the demagnified DMD pattern onto the atoms. Im1 (EFL $= 51.7\,\text{mm}$) and Im2 ($f = 400\,\text{mm}$) are the two lenses of the z imaging setup. The system has been tested both with a $\lambda = 589\,\text{nm}$ laser beam of repumper or probe light (yellow), that can also be sent directly on the atoms without using the DMD, and with a $\lambda = 532\,\text{nm}$ beam (green), that illuminates the DMD and will be used to create repulsive optical potentials. A photodiode is used to monitor the optical power of the laser beams and could be integrated in a feedback electronic circuit for stabilization.

After the preliminary tests on a secondary optical table, the new imaging systems and the DMD setup were implemented in the main apparatus as shown in Fig. 2.18. This involved a partial rebuilding of the experimental setup, aimed at placing the imaging objectives as close as possible to the atoms and the cameras on the desired side of the science chamber, which required a substantial modification of the DS-MOT and GM optical setup. Since the MOT beams are used in a different stage of the experiment, much

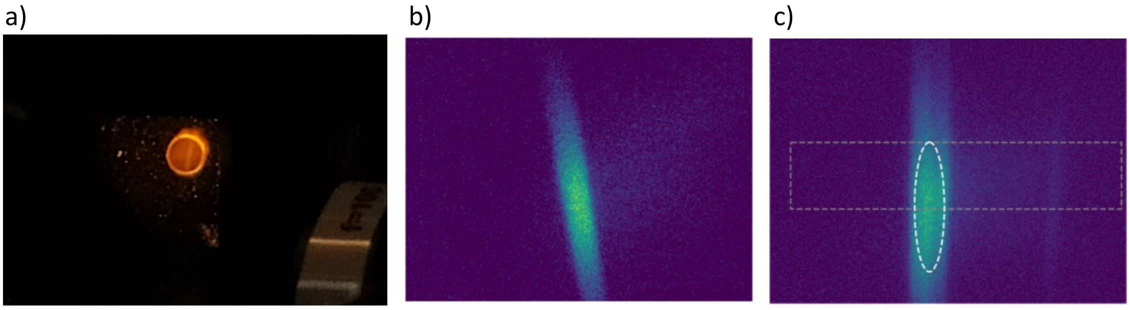

Figure 2.19: Alignment of the z optical path. (a) Photograph of the DS-MOT. The narrow, almost vertical, fluorescent line that crosses the DS MOT is the repumper beam under alignment. (b) Absorption image of a thermal cloud, taken with `cam_y1`, using the light of the beam that we are aligning to repump the atoms. This image corresponds to the photograph in (a). (c) Absorption image taken after the alignment of the vertical beam.

before the imaging of the BEC, the mirrors that retroreflect those beams are mounted on translational stages, equipped with an electrical servo-motor. This way the mirrors are removed after the 3DMOT phase, letting the imaging beams propagate through the science cell. We choose to move the MOT mirrors, rather than the imaging ones, to avoid perturbations of the probe beam paths due to vibrations, which would be highly detrimental for the imaging, while the MOT is less sensitive, given its long loading time.

Most of the optics of the DMD setup are placed, together with the optics for the z probe beam, on a secondary breadboard located above the cell, as shown in Fig. 2.18. The light is then guided along a vertical optical path, used both for the z imaging and for projecting the DMD light patterns on the atoms. The alignment of this optical path has been quite challenging, because of the many mechanical elements located in the vicinity of the cell, in particular below, reducing the access and visibility.

The z probe path was aligned first. To ensure a vertical propagation of the beam through the atomic cloud, initially, instead of the probe beam, we used a narrow beam of repumper light, turned on during the loading of a DS-MOT, as shown in Fig. 2.19. This allowed us to visualize the direction of the optical path directly by eye, observing the fluorescence of the MOT (a), as well as by imaging a thermal atomic cloud using the horizontal `cam_y1` camera, repumping a line of atoms with the beam under alignment (b-c). We then replaced the repumper light with probe light, without further changing the input path, and finely adjusted the alignment of the imaging optics placed below the cell, to image the atoms on the `cam_z1` camera, which was finally brought at focus on the atoms plane (see Sec. 2.7.6). Cage systems are used to enhance the mechanical stability and facilitate the alignment procedures.

The optical path of the DMD light was then aligned onto the atoms by making it overlap with the previously aligned vertical probe path, used as a reference. Fine alignment and focusing was then further performed by imaging the DMD pattern on the same `cam_z1` camera used to image the atoms. This allowed for a second characterization of the demagnification and resolution properties of the DMD optical setup in its final alignment conditions. Finally, a preliminary effect of repulsive potentials created by means of DMD patterns with 532 nm light was observed on an atomic cloud.

Future perspectives for the DMD The DMD was not used in the experiments that are further described in the remaining part of this thesis. Its implementation, however, opens the way to innumerable possibilities of manipulating the atoms by means of optical potentials that can be designed at will and changed with precise timing. For instance, repulsive potentials could be used to generate topological defects in an equilibrium BEC in a well controlled way. This could pave the way, for example, to the investigation of the formation of vortex rings induced by the motion of a repulsive linear barrier through the superfluid and to the study of leapfrogging dynamics [131, 132, 133]. Another perspective regards the use of the DMD to locally modify the trapping potential for an atomic cloud that is rapidly cooled across the transition, extending the investigation of the out-of-equilibrium dynamics during the BEC order parameter formation, that is treated in Chapter 4. Providing additional degrees of control on the system, the DMD could for instance allow for shortcuts to reach more efficiently the final equilibrium condition.

2.7.4 Absorption Imaging procedure

To image the atomic distribution, one of the standard techniques used in ultracold atom experiments is resonant absorption imaging (RAI) [28]. In this Section I first introduce the working principle of this technique, referring to its implementation in our experiment. Afterwards, the procedures used for calibration and focusing are explained. For further details, see Refs. [85, 5, 28, 110, 111].

Let us consider a probe beam of intensity I propagating along the z direction through the atomic cloud, of density $n(x, y, z)$. The decay of intensity of the laser beam, due to atomic absorption, is well described by the Lambert-Beer law:

$$\frac{dI}{dz} = -\hbar\omega R n, \tag{2.14}$$

where R is the scattering rate between the light and the atoms. Approximating the atoms as two-level systems, and considering π polarized light, R can be written as:

$$R = \frac{\Gamma}{2} \frac{I/(\alpha I_{sat})}{1 + \frac{I}{\alpha I_{sat}} + \left(\frac{2\Delta}{\Gamma}\right)^2}, \tag{2.15}$$

where $I_{sat} = \hbar\omega_{at}^3\Gamma/(12\pi c^2)$ is the saturation intensity for a closed two-level transition, Γ the natural linewidth of the excited atomic state, $\Delta = \omega - \omega_{at}$ the detuning of the laser (angular) frequency $\omega = 2\pi\nu$ with respect to the atomic transition frequency ω_{at} and α is a corrective coefficient depending on the magnetic field where the atoms are imaged.

Replacing this expression of the scattering rate in Eq. 2.14, we get:

$$\frac{dI}{dz} = -n\frac{\sigma_0}{\alpha} I_{sat} \frac{I/I_{sat}}{1 + \frac{I/I_{sat}}{\alpha} + \left(\frac{2\Delta}{\Gamma}\right)^2}, \tag{2.16}$$

where $\sigma_0 = 3\lambda^2/(2\pi)$ is the resonant value of the absorption cross-section.

For resonant light ($\Delta = 0$), integrating 2.16 along the direction of imaging z, we obtain the following expression for the optical density (OD):

$$\mathrm{OD} = \alpha \ln\left(\frac{I_{in}}{I_{out}}\right) + \frac{I_{in} - I_{out}}{I_{sat}}, \tag{2.17}$$

where $I_{in} = I(z = -\infty)$ and $I_{out} = I(z = \infty)$ are the input and output intensity of the light, i.e. the intensities of the probe beam before and after the propagation through the atomic cloud, respectively.

The OD is related to the column density n_1, which is given by the atomic density integrated along the line of sight:

$$n_1(x, y) = \int_{-\infty}^{\infty} n(x, y, z)dz = \mathrm{OD}(x, y)/\sigma_0. \tag{2.18}$$

In practice, to measure the light intensity we record the counts $C(i, j)$ on the pixels (x_i, y_j) of the sensor of a camera. These counts, for a probe-pulse duration τ_p, are given by:

$$C(i, j) = \eta GT \int_0^{\tau_p} \frac{I(x_i, y_i, t)}{\hbar\omega} \left(\frac{L_{pix}}{M}\right)^2 dt = \chi_{sat} \frac{I(x_i, y_j)}{I_{sat}} \tau_p, \tag{2.19}$$

where the intensity is assumed to be time-independent and χ_{sat} collects all the factors characterizing the imaging system and the sensor, such as the detector efficiency η and gain G, the optics transmittance T, the pixel size L_{pix} and the magnification M of the imaging system:

$$\chi_{sat} = \eta GT \left(\frac{L_{\mathrm{pix}}}{M}\right)^2 \frac{I_{sat}}{\hbar\omega}. \tag{2.20}$$

To measure the input and output light intensities I_{in} and I_{out}, we collect three images, as shown in Fig. 2.20. These images are:

- (a) *atoms picture*: a picture of the atoms, illuminated by a pulse of probe light of duration τ_{probe}, resonant with the $|F = 2\rangle \to |F' = 3\rangle$ cycling transition. Before the probe pulse, the atoms, initially in the $|F = 1, m_F = -1\rangle$ trapped ground state, need to be transferred to $F = 2$ to become resonant with the probe frequency: in our experiment this is done either by illuminating the sample for a short pulse-time with an optical repumper beam, that transfers the atoms to the excited $F' = 2$ state (orange arrow in Fig. 2.1), or by means of a pulse of microwave radiation, resonant with the $|F = 1\rangle \to |F = 2\rangle$ transition, which can be used to outcouple and image a small fraction of atoms (see Section 2.9).
  For each pixel (i, j), the *atoms* image yields the counts $C(i, j)_{out}$, which depend on the time-integral of the output intensity profile $I(x, y)_{out}$, over the duration of the probe pulse.
- (b) *probe picture*: a picture taken in the same probe illumination conditions as the previous, but without atoms, since no repumping to states resonant with the probe light takes place. The corresponding pixel counts $C(i, j)_{in}$ give a measure of the time- integral of the input intensity I_{in}.
- (c) *background picture*: a picture taken without atoms nor probe light. The pixel counts $C(i, j)_{bg}$ depend on the background illumination conditions, determined by external stray light and dark-counts of the sensor.

For each pixel x_i, y_j of the camera, the following relation holds between the atomic OD and the camera counts:

$$\mathrm{OD} = \alpha \ln \left(\frac{C_{in} - C_{bg}}{C_{out} - C_{bg}}\right) + \frac{C_{in} - C_{out}}{\chi_{sat}\tau_p}, \tag{2.21}$$

where the probe-pulse duration τ_p is directly controlled in each experimental run and the imaging parameters α and χ_{sat} are found using the calibration methods described in the following paragraph.

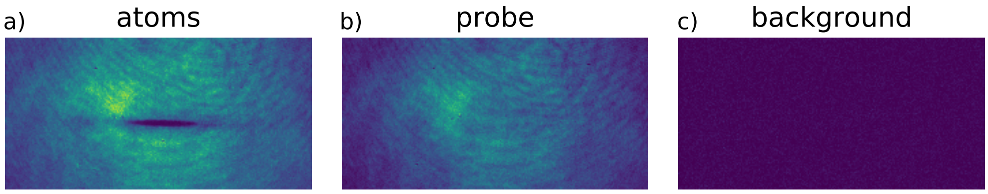

Figure 2.20: The three images used to obtain the optical density of the atomic cloud, here imaged in situ using the `cam_z1` camera.

2.7.5 Calibration of imaging system

Determination of χ_{sat} and α

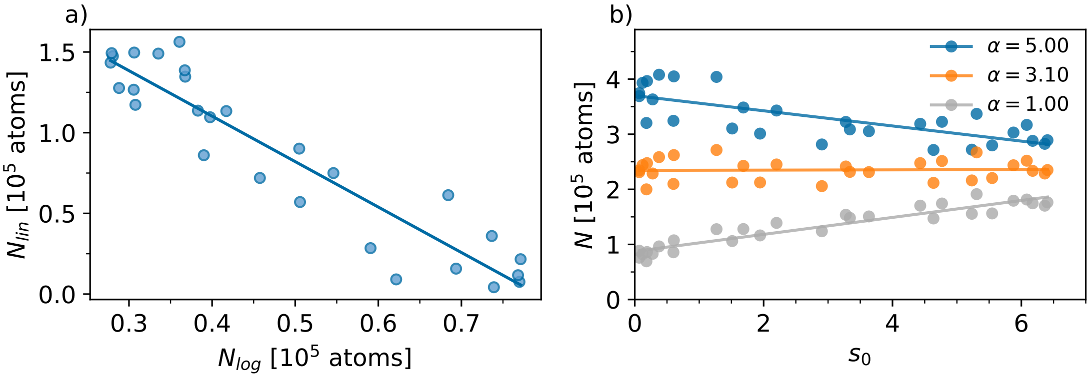

Figure 2.21: Calibration of α for the `cam_z1` camera, used for the measurements of the equation of state reported in [5] and in Chapter 3. (a) Following the approach of [110] we determine α from the slope of a linear fit of N_{lin} Vs N_{log}, measured scanning the probe light intensity. We obtain $\alpha_1 = 3.2(2)$. (b) Using the method described in [111], the value of α is determined by minimizing the variation of the measured atom number N for a scan of $s_0 = I_{in}/I_{sat}$. This yields $\alpha_2 = 3.10(2)$. The two values are compatible, with an average $\alpha = 3.15(12)$.

To get a quantitative measurement of the column density, one needs to calibrate the imaging system first, finding the experimental values of χ_{sat} and α. We measure χ_{sat} by scanning the probe light intensity and comparing the total pixel counts of the probe images with the measurement of a calibrated power meter.

To calibrate α, two different, although equivalent, procedures can be followed [110, 111], as described in [5]. Dividing Eq. 2.17 by σ_0 to obtain the column density n_1 via Eq. 2.18, and then integrating over the region containing the atomic sample, we obtain the measured total number of atoms N, which we can write as:

$$N = \alpha N_{log} + N_{lin}, \tag{2.22}$$

where N_{log} and N_{lin} are the two contributions in the absorption signal coming from the linear and logarithmic term, respectively. Each of the two quantities depends on $s_0 = I_{in}/I_{sat}$, but their weighted sum is the number of atoms N, and must thus be independent of the probe light intensity. Scanning I_{in}, we measure N_{lin} and N_{log} for a dilute atomic sample. Following the method of [110] we can determine α from the slope of a linear fit of N_{lin} against N_{log}, as shown in Fig. 2.21a). Alternatively, for the same scan of I_{in}, we can compute $N(s_0)$ for several values of α, as shown in Fig. 2.21 (b), finding the value that minimizes the variation of N, as in [111]. We tested both calibration methods, finding compatible results. In Fig. 2.21 we report those for the calibration of the `cam_z1` camera.

Determination of the magnification

To convert the length scales d_{pix}, measured in pixels on the camera, into actual distances in the plane of the atoms d_{at}, we need to find the magnification M of the imaging system, since $d_{\mathrm{at}} = d_{\mathrm{pix}} \frac{L_{\mathrm{pix}}}{M}$, where L_{pix} is the camera pixel size ($L_{\mathrm{pix}} = 4.5\,\mu\mathrm{m/pixel}$ for our Stingray cameras).

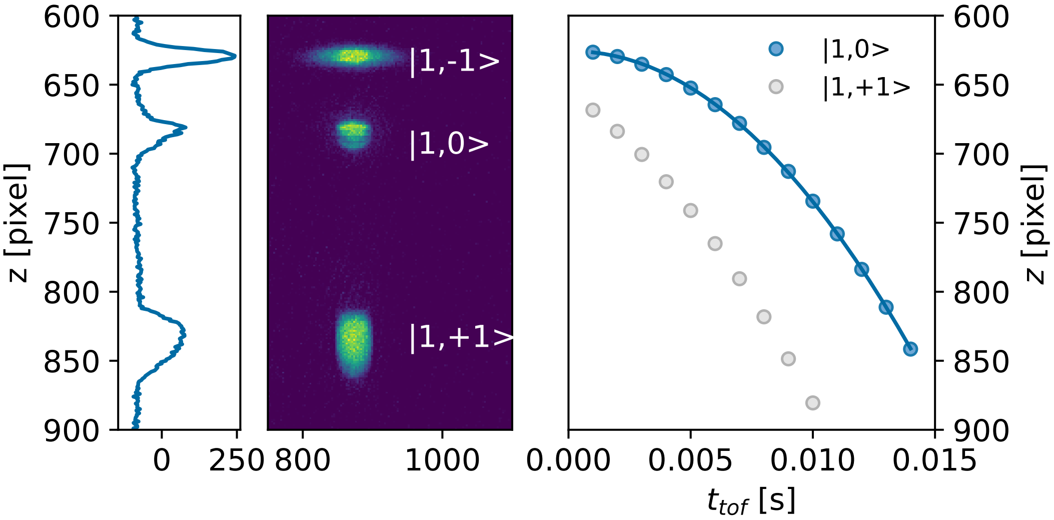

Figure 2.22: The magnification of the `cam_y1` camera is extracted from the free fall of the $|1,0\rangle$ atoms.

For the horizontal cameras, we measure the magnification exploiting the free fall of the atoms. By means of a pulse of the same RF field used for the evaporation, a fraction of atoms is extracted from the trapped $|F=1, m_F=-1\rangle$ sample, and transferred to the $|1,0\rangle$ and $|1,+1\rangle$ states (see Fig. 2.22). The cloud of $|1,0\rangle$ atoms is not sensitive to the magnetic field of the trap, to first order in the Zeeman effect, and thus fall under the effect of the gravitational acceleration g, while the $|1,+1\rangle$ atoms are antitrapped and fall thus with a higher acceleration, determined also by the vertical magnetic field gradient. By means of the `cam_y1` camera, we record the z position of the center of mass of the free-falling cloud of $|1,0\rangle$ atoms for various times of flight t_{tof} (blue dots in the right panel of Fig. 2.22). We fit the measured displacement with a second order polynomial $z[\mathrm{pixel}] = a t_{\mathrm{tof}}^2 + b t_{\mathrm{tof}} + c$ (solid line). Comparing the fitted coefficient a with the coefficient $g/2$ expected for the free fall, and considering the pixel size of the camera, we find a magnification $M_{\texttt{cam\_y1}} = a\, L_{\mathrm{pix}}/(g/2) = 1.020(6)$.
In a similar way, we calibrate also the other horizontal cameras.

To measure the magnification for the vertical imaging system `cam_z1`, we apply, instead, a horizontal force through a pulse of a magnetic gradient along x, and measure the subsequent in-trap dipole oscillations with both `cam_y1` and `cam_z1`, capturing the displacement Δx as a function of time, as shown in Fig. 2.23. Comparing the oscillation amplitude A for

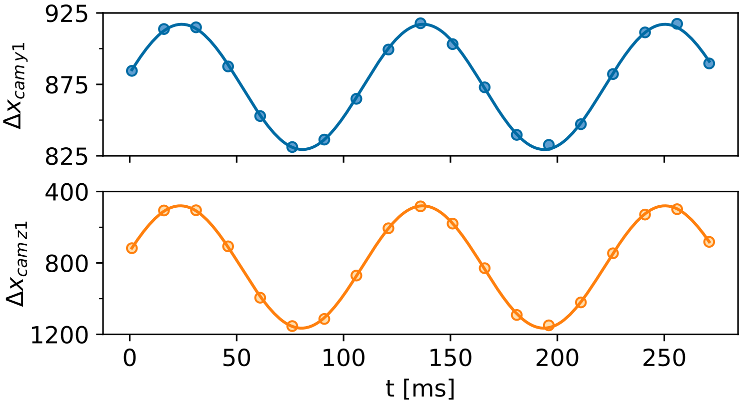

Figure 2.23: Comparison of dipole oscillations along x measured with `cam_y1` (above) and `cam_z1` (below). Notice the different scale of the vertical axis. Knowing the magnification of `cam_y1`, we obtain that of `cam_z1`.

the two cameras (obtained from a sinusoidal fit, solid line), we obtain the magnification of `cam_z1`, knowing that of `cam_y1`: $M_{\texttt{cam\_z1}} = M_{\texttt{cam\_y1}} A_{\texttt{cam\_z1}} / A_{\texttt{cam\_y1}} = 7.97(17)$.

The same data yield also a measurement of the axial trapping frequency $\omega_x/2\pi = 8.83(2)\,\mathrm{Hz}$.

2.7.6 Focusing the imaging system

A precise focusing of the imaging system is important because an out-of-focus imaging system yields blurred pictures, spoiling the resolution. Moreover, when the camera is not at focus, non-resonant atoms in $|F = 1\rangle$ can provide a non-negligible signal, that could lead to a wrong estimation of the column density profile. This signal can be estimated as follows [134], [85], [28], [135].

In conditions of weak probe intensity ($I/I_{\mathrm{sat}} \ll 1$) or far detuned light ($\delta = 2\Delta/\Gamma \gg 1$) the atomic response to light can be considered linear and the atomic cloud treated as an optical medium with a density-dependent refractive index:

$$n_{\mathrm{ref}} = 1 + \frac{\sigma_0 \lambda n}{4\pi} \left(\frac{i}{1+\delta^2} - \frac{\delta}{1+\delta^2} \right) , \tag{2.23}$$

where the imaginary part, maximum at resonance, is responsible for the absorption (see Sec. 2.7.4). The real part, instead, describes the accumulation of a phase factor $e^{i\phi}$ in the probe beam that propagates through the atomic cloud, with ϕ proportional to the column density $n_1 \equiv \int n dz$ along the line of sight:

$$\phi = \frac{2\pi}{\lambda} \int \mathrm{Re}(n_{\mathrm{ref}} - 1) dz = -\frac{\sigma_0}{2} \frac{\delta}{1+\delta^2} \int n dz, \tag{2.24}$$

where the "thin lens" approximation has been used, considering light to enter and exit at the same (x, y) coordinate [28]. Assuming a flat intensity I_0 for the incoming probe beam, after a propagation over a distance D, the phase-shifted light produces an intensity profile:

$$I(D) = I_0 \left(1 - \frac{\lambda D}{2\pi} \nabla^2 \phi \right) , \tag{2.25}$$

which is proportional to the second derivative of the column density. This signal can be used for a far-detuned non-destructive imaging technique known as *shadowgraph imaging* [135]. Here D is the distance between the plane of the atoms and the object plane that is at focus on the camera. The diffractive signal of Eq. 2.25 is cancelled if $D = 0$, which occurs when the atoms are imaged perfectly at focus on the camera. We exploit this fact to focus the camera with sub-millimeter precision, by moving it with a micrometric translational stage while recording the shadowgraph signal. To obtain this signal, for each position in which we move the camera, we produce a condensed sample of $|1, -1\rangle$ atoms in the magnetic trap. The sample is then imaged taking 4 pictures, instead of only the usual 3 images needed to reconstruct the OD. The first picture is taken illuminating the atoms with the probe beam, but without any repumper, this way capturing the dispersive signal of the $F = 1$ atoms, which is non-zero if the camera is not perfectly at focus. The other three pictures are used to measure the OD of the cloud, which is useful to monitor that the atomic signal is still present[6]. The third picture, in particular, is taken after releasing the atoms from the trap to obtain the probe profile.

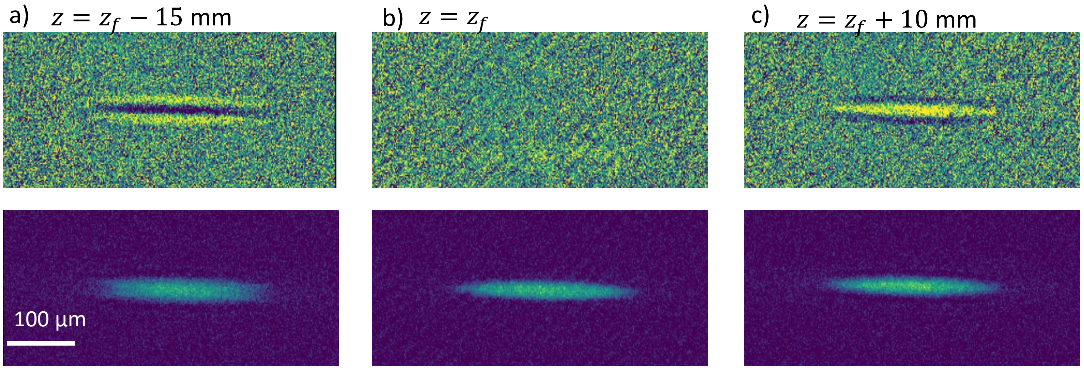

Figure 2.24: Shadowgraph signal of the $F = 1$ atoms (top) and OD for the same shot, measured during the focusing procedure of `cam_z1`, where the position z of the camera along the optical axis is changed. The camera is at focus ($z = z_f$) when the off-resonant signal is minimized, as shown in (b).

Figure 2.24, taken while focusing the z imaging system, shows how the first picture (top) appears in case: (a) the camera is too far from the atoms, (b) the imaging system is correctly at focus and (c) the camera is too close to the atoms. The bottom pictures show the corresponding OD.

Moving the camera, we minimize the shadowgraph signal, which can be quantified by integrating our $F = 1$ images over the rows, after subtracting the probe image, and fitting the resulting profile to a function given by the second derivative of a Gaussian $A(x^2 - 1)e^{-x^2/2\sigma^2}$ [85].

This procedure has been used to precisely focus all our cameras. We could not completely remove the dispersive signal for `cam_x1`, given the long dimensions of the condensate in the x direction, which do not allow to get the whole sample at focus.

We also scan the probe frequency to make sure that it is at resonance with the $|F = 2\rangle \to |F' = 3\rangle$ transition.

---

[6] Otherwise a zero shadowgraph signal could simply be caused by a zero atomic density, in case of failure in some previous stage of the experimental shot.

2.8 Time of flight imaging

The typical dimensions of a BEC in our trap are of the order of a few hundred μm, with typical central densities $n_0 \geq 10^{20}\,\mathrm{m}^{-3}$, corresponding to optical densities $\geq 10^2$. This impedes a correct estimation of the column density profile of the trapped cloud, when the standard resonant absorption imaging technique, described before, is used. When the optical density along the probe path is too high, indeed, saturation occurs: after the absorption in the atomic medium, the remaining intensity I_{out} becomes comparable with the background noise, yielding an inaccurate estimation of the column density of the cloud.

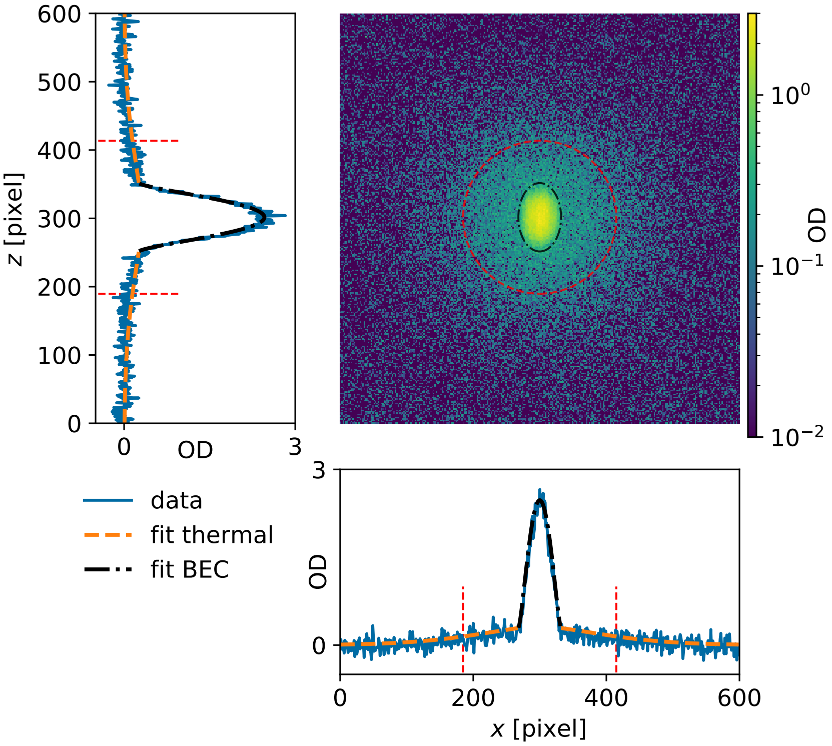

Figure 2.25: Optical density of a partially condensed cloud, imaged after a time of flight $t_{TOF} = 50\,\mathrm{ms}$. The profiles on the left and below correspond to a central slice along z and x, respectively. The Bose and Thomas-Fermi fits are shown. The black dot-dashed ellipse marks the extension of the BEC, given by the fitted Thomas-Fermi radii, while the red dashed line indicates the dimensions $\sigma_{x,z}$ of the thermal cloud.

A frequently used solution to measure the number of atoms in the system, is to let the cloud expand by releasing it from the trap and image it after a time of flight (TOF), when its density has become low enough.

In order to perform TOF imaging, we switch off the magnetic trap and we either let the atoms fall under the action of gravity, or levitate them by means of a vertical magnetic gradient.

An example of a TOF image of a partially condensed cloud, taken after an expansion of $t_{\mathrm{TOF}} = 50\,\mathrm{ms}$, is shown in Fig. 2.25.

To extract the temperature and number of atoms from the measured optical density of the cloud, we perform a fit to a 2D bimodal function, given by the sum of an integrated Thomas-Fermi distribution to account for the condensed part and a Bose function for the non-condensed thermal tails:

$$f_{\mathrm{bim}}(x,z) = f_{\mathrm{TF}}(x,z) + f_{\mathrm{Bose}}(x,z) + \text{offset}, \tag{2.26}$$

where the Bose function is:

$$f_{\mathrm{Bose}}(x,z) = \frac{A_{th}}{\zeta_2} g_2 \left\{ \exp\left[-\frac{(x-x_0)^2}{2s_x^2} - \frac{(z-z_0)^2}{2s_z^2} \right] \right\}, \tag{2.27}$$

while the Thomas-Fermi function is:

$$f_{\mathrm{TF}}(x,z) = \max\left\{ 0, A_{\mathrm{TF}} \left[1 - \left(\frac{x-x_0}{r_x}\right)^2 - \left(\frac{z-z_0}{r_z}\right)^2 \right]^{3/2} \right\}. \tag{2.28}$$

In the above expressions:

- (x_0, z_0) are the coordinates of the position of the center of the cloud in the image (assuming a common center for the BEC and thermal cloud);
- $s_{x,z}$ and $r_{x,z}$ are the widths of the thermal distribution and the Thomas-Fermi radii along the x, z directions, respectively, measured in pixels on the image. The corresponding dimensions of the atomic distribution are obtained multiplying by the camera pixel size and dividing by the magnification: $\sigma_{x,z} = s_{x,z} L_{\mathrm{pix}}/M_{\mathrm{cam}}$, $R_{x,z} = r_{x,z} L_{\mathrm{pix}}/M_{\mathrm{cam}}$;
- A_{th} and A_{TF} are the amplitudes of the two distributions;
- ζ_ν is the Riemann function;
- $g_2(u) = -\int_0^u \log(1-t)/t\, dt$ is the polylogarithm of order 2 (also known as Spence's function).

From the amplitude A_{th} and widths σ_x, σ_z of the Bose function, the number of thermal atoms N_{th} can be obtained:

$$N_{th} = 2\pi \frac{\zeta_3}{\zeta_2} A_{th} \frac{\sigma_x \sigma_y}{\sigma_0}, \tag{2.29}$$

where σ_0 is the resonant scattering cross-section.
The number of atoms N_0 in the BEC can be extracted from the Thomas-Fermi fit:

$$N_0 = 1.25 A_{\mathrm{TF}} \frac{R_x R_y}{\sigma_0} \tag{2.30}$$

The total number of atoms in the cloud is then given by $N = N_{th} + N_0$.
During the TOF expansion, the density distribution of the cloud changes shape, due to the conversion of the energy of the trapped sample into kinetic energy. For a BEC, in the Thomas-Fermi limit of large number of atoms, the initial kinetic energy can be neglected and the *in situ* energy is mainly determined by the mean-field interactions. In this case the expansion is well described by the Castin-Dum equations [136], relating the Thomas-Fermi radii after the TOF expansion to the *in-situ* radii $R_\rho(0), R_x(0)$:

$$R_\rho(t_{\mathrm{TOF}}) = R_\rho(0)\sqrt{1 + (\omega_\rho t_{\mathrm{TOF}})^2} \tag{2.31}$$

$$R_x(t_{\mathrm{TOF}}) = R_x(0)\left\{ 1 + \lambda^2 \left[(\omega_\rho t_{\mathrm{TOF}}) \arctan(\omega_\rho t_{\mathrm{TOF}}) - \ln\sqrt{1 + (\omega_\rho t_{\mathrm{TOF}})^2} \right] \right\} \tag{2.32}$$

where $\lambda = \omega_\rho/\omega_x$ is the aspect ratio of the elongated trap. The expansion is much faster in the tightly confined radial directions than in the axial direction, which has the well-known consequence that the BEC inverts its aspect ratio during the expansion, as can be seen in Fig. 2.25, where the BEC is more elongated in the z direction, while *in situ* this is a direction of tight confinement.

The expansion of the thermal cloud is instead governed by the kinetic energy of the thermal atoms, determined by the temperature T. The width of the thermal cloud after t_{TOF}, assuming a purely ballistic expansion with isotropic velocity $v_0 = \sqrt{k_B T/m}$, can be written as: $\sigma^2(t_{\mathrm{TOF}}) = \sigma^2(0) + t^2_{\mathrm{TOF}} k_B T/m$, which becomes linear in T for long enough t_{TOF}. A measurement of the temperature can thus be performed by taking images of the thermal cloud at different expansion times, and performing then a linear fit of $\sigma^2(t_{\mathrm{TOF}})$ as a function of t^2_{TOF}.

The temperature can also be extracted from the widths σ_x and σ_z of the thermal distribution of a single image, taken after an expansion for long enough time of flight $t_{\mathrm{TOF}} \gg 1/\omega_{x,\rho}$, to ensure the nearly-ballistic asymptotic expansion regime to be reached. Following [137], we extract an effective temperature for each direction:

$$T_i = \frac{m\omega_i^2\sigma_i^2}{(1+\omega_i^2 t^2_{\mathrm{TOF}})k_B}, \text{ for } i = x, z. \tag{2.33}$$

For a thermal cloud that is released from an elongated trap, hydrodynamic collisions can create a velocity imbalance between the axial and the radial directions, proportional to the equilibrium collisional rate γ_{coll}, making the expansion weakly anisotropic. For weak deviations from the ballistic expansion ($\gamma_{\mathrm{coll}} \lesssim \omega_\rho$), kinetic energy conservation suggests that the mean square expansion velocities take the form $\langle v_\rho^2\rangle/v_0^2 \sim 1 + b\gamma_{\mathrm{coll}}/(2\omega_\rho)$ and $\langle v_x^2\rangle/v_0^2 \sim 1 - b\gamma_{\mathrm{coll}}/\omega_\rho$, where b depends in general on ω_x, ω_ρ and t_{TOF}. The temperature of the cloud can then be estimated according to the following expression, independent of the coefficient b:

$$T = \frac{2\omega_x^2 t^2_{\mathrm{TOF}} T_z + (1+\omega_x^2 t^2_{\mathrm{TOF}})T_x}{1 + 3\omega_x^2 t^2_{\mathrm{TOF}}}, \tag{2.34}$$

where hydrodynamic corrections are cancelled out to first order in $\gamma_{\mathrm{coll}}/\omega_\rho$ (see note 26 in Ref.[137]). This formula has been used for the measurement of the temperature for the Equation of State of the Bose gas, in Chapter 3.

To make the measurement of the temperature more reliable, one can limit the fitting region for the Bose fit to the outer tails of the thermal distribution, where the effect of interactions is minimized and the expansion is closer to the ideal case. If the condition $t_{\mathrm{TOF}} \gg 1/\omega_i (i = \rho, x)$, required for a nearly ballistic asymptotic expansion, is well satisfied only for the radial direction, but not for the weakly confined axial one, a reliable measurement of the temperature can be obtained from Eq. 2.33, taking only the radial expansion of the cloud into account, as shown in Ref. [138]. This was done in the case of the measurements of Chapter 4.

The fact that via a long enough TOF expansion the *in situ* momentum distribution is mapped into the TOF density distribution, can be exploited to measure the *in situ* spatial phase fluctuations

2.9 In situ imaging: Partial Transfer Absorption Imaging and HDR reconstruction

Although TOF imaging allows for the measurement of the number of atoms and of the temperature of the ultracold gas, a direct measurement of the density profile of the trapped gas can only be obtained by *in situ* imaging.

In this section I describe the partial transfer imaging (PTAI) and reconstruction technique that we developed [4] to obtain accurate *in situ* images of the optical density distribution of a partially condensed trapped Bose gas, which was fundamental for the measurement of the Equation of State [5].

The standard resonant absorption imaging (RAI) technique described in 2.7.4, if applied to a BEC in situ, does not yield accurate results, because of the high optical density at the center of the cloud $n_0 \geq 10^{20}\mathrm{m}^3$, corresponding to typical maximum OD values ≥ 100, much above the saturation limit of standard RAI . The consequence is that the probe beam gets completely absorbed in the highest OD regions, yielding a signal comparable with the camera noise, with the result of producing a distorted OD distribution as outcome of the measurement. In contrast, in the dilute thermal tails of the partially condensed cloud, the OD is several orders of magnitude smaller. A high dynamic-range imaging is therefore needed, to capture both high and low ODs with a good signal to noise ratio (SNR).

The problem of imaging dense samples can be tackled by using saturated absorption and high-intensity imaging [111, 139], but this still gives access only to an OD-range that spans at most one order of magnitude, instead of the full desired range.

Moreover, RAI is fully destructive, since the interaction with the resonant probe photons imparts large kinetic energy to the atoms, with the consequence that only a single image of the atomic distribution can be taken per experimental cycle, which has a typical duration of up to one minute in our case. In addition, one has to rely on the reproducibility of the experimental conditions, without being able to observe the same sample multiple times.

Alternative imaging methods, such as phase-contrast [140, 141], Faraday [142] and diffraction contrast imaging [143], have the advantage of being non-destructive, but still suffer from the same dynamic-range limitations as RAI.

The imaging technique we implemented is based on partial transfer absorption imaging (PTAI), a method first demonstrated by [144, 145], which allows for minimally destructive measurements.

The principle at the basis of PTAI is to transfer a fraction of atoms from the sample to an auxiliary state, making sure that the outcoupled atoms maintain the original density distribution, apart from a constant multiplicative factor determined by the extraction ratio. The extracted atoms are then imaged using light that is resonant with a cycling transition from the auxiliary state to an electronically excited state. The imaging light is instead far-off-resonance for the remaining atoms in the original sample, which are left practically undisturbed. This makes this method minimally destructive and enables multiple measurements on the same sample, allowing, for instance, to study dynamical processes in a reliable and time-efficient way, since only one (or a few) shots are needed to fully characterize the dynamics of interest. We exploited this feature to rapidly characterize physical parameters of our system, such as the trapping frequencies of the potential that confines the atoms or the Rabi frequency of the outcoupling microwave field.

Changing the fraction of extracted atoms, PTAI allows to image arbitrarily high ODs with a high signal to noise ratio. We exploited this feature to optimally capture the full OD range of the trapped atomic cloud, taking several images of the same system in a single experimental shot, at increasing extraction ratios. These images are then combined, upon proper recentering and rescaling, to obtain an accurate image of the full distribution in a way analogous to High Dynamic Range (HDR) photography [146, 147, 148], where the final image is the result of the combination of several frames taken at different exposure conditions.

We used this reconstruction technique to accurately measure the column density profile of the trapped Bose gas to obtain the Equation of State, which is the subject of Chapter 3.

2.9.1 Experimental implementation

In our experiment, to implement PTAI, we use a signal generator (Marconi Instruments 2024 [92]) to generate a microwave field resonant with the $|F=1, m_F=-1\rangle \rightarrow |F'=2, m'_F=-2\rangle$ transition, in presence of the IP trap magnetic field. The radiation is amplified by means of a 100 W amplifier [Minicircuits ZHL-100W-272+ [93]] and delivered to the atoms by means of a hook antenna [see Fig. 2.26 (a)], with predominantly σ^- polarization, which favors the chosen transition. The transferred atoms are then imaged with probe light resonant with the $|F=2\rangle \rightarrow |F'=3\rangle$ cycling transition, as shown in Fig. 2.26b).

The microwave field causes the system to undergo Rabi oscillations between the two levels coupled by the radiation. The fraction of atoms transferred after a time $\tau_{\mu w}$ is:

$$P(\tau_{\mu w}, \delta) = \frac{\Omega^2}{\Omega^2+\delta^2} \sin\left(\frac{\tau_{\mu w}}{2}\sqrt{\Omega^2+\delta^2}\right)^2, \tag{2.35}$$

where δ is the detuning of the microwave frequency from the atomic resonance. The combination of the non-homogeneous magnetic field and gravity causes the detuning to be spatially dependent:

$$\delta(x,y,z) = \frac{3m}{2\hbar}\left(\omega_x^2 x^2 + \omega_y^2 y^2 + \omega_z^2(z^2 - 2zz_{sag})\right) \tag{2.36}$$

where the origin of the coordinates is set at the center of the atomic cloud, m is the atomic mass and $z_{sag} = g/\omega_z^2$ is the gravitational sag (Eq. 2.8), responsible of the displacement of the center of mass of the cloud with respect to the minimum of the magnetic field. The origin of the reference frame is set on the center of mass of the atomic cloud, where $\delta = 0$. The non-uniform detuning causes a local variation of the transferred fraction, potentially introducing distortions in the measured optical density profile, as the outcoupled cloud is not a rescaled copy of the original distribution. However, one can identify a regime of parameters where the non-uniformity can be neglected.

For $\Omega\tau_{\mu w} \ll 1$ the transferred fraction of Eq. 2.35 becomes $\sim \Omega^2\tau_{\mu w}^2/2$, independent of the microwave frequency. For a given product $\Omega\tau_{\mu w}$, a large Rabi frequency $\Omega \gg \delta$ reduces

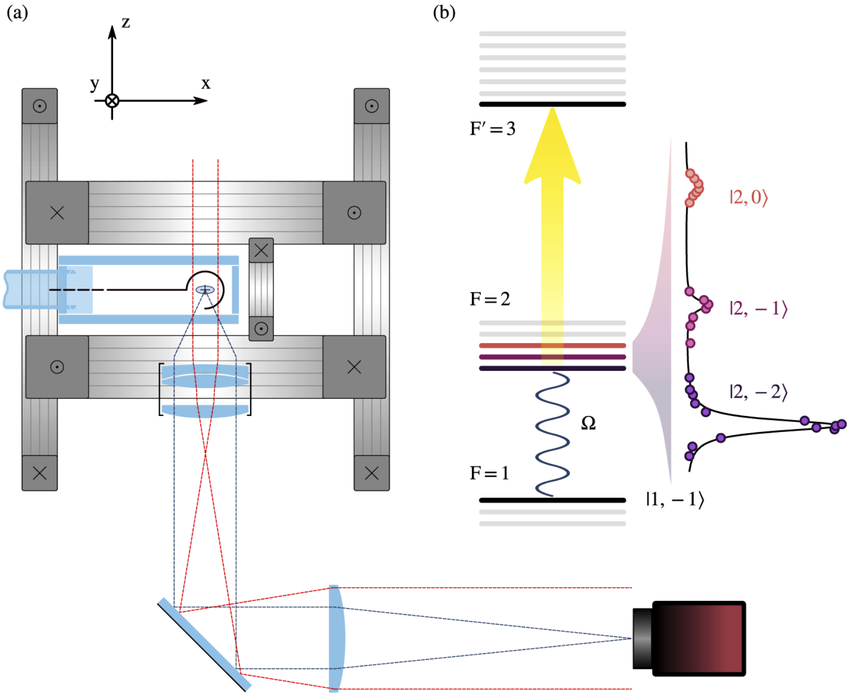

Figure 2.26: (a) Experimental apparatus used for the PTAI imaging. The coils generating the magnetic field are shown in grey. The microwave field is delivered to the atoms (blue ellipse) by a hook antenna placed on the side of the glass cell. (b) The atoms are initially in the $|1,-1\rangle$ state. A tunable fraction is transferred to the $|2,-2\rangle$ state by means of a microwave pulse of Rabi frequency Ω and then imaged in $F'=3$ using resonant probe light (yellow arrow). On the side, a spectroscopy of the three allowed microwave transitions between $|1,-1\rangle$ and the $F=2$ manifold are shown, obtained by scanning the microwave frequency, keeping the same polarization. Image adapted from [4]

the distortions caused by the inhomogeneous detuning thanks to the power-broadening of the resonance. More details about the effect of the inhomogeneous transfer are presented in Sec. 2.9.6.

For a given pulsetime, we scan the microwave frequency to find the maximum transfer, which occurs when the field is resonant with the center of the cloud, where the density is highest. This agrees with our choice of setting $\delta = 0$ at the center of the atomic cloud.

2.9.2 Multi- and single-shot measurement of the Rabi frequency

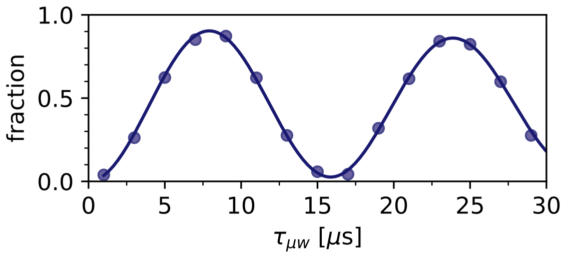

Figure 2.27: Multishot measurement of the Rabi frequency of the microwave field. The fraction of extracted atoms is measured scanning the duration of the microwave pulse $\tau_{\mu w}$. The frequency is then extracted from a fit (solid line), taking the nonuniform detuning into account (Eq. 2.40).

In order to quantify the extracted fraction of atoms in Eq. 2.35, the Rabi frequency Ω of the microwave field needs to be known. The standard way to measure Ω is by following the Rabi flopping of the populations of the ground- and excited- state. This is done by repeating the experiment several times, changing each time the duration of the microwave pulse $\tau_{\mu w}$. The populations of the two states are measured using a Stern-Gerlach [149] technique, counting the fraction of atoms in the two clouds after spatially separating them. This is done by letting the transferred atoms fall under the action of gravity and of the magnetic field, in which they are antitrapped, for a time of flight $t_{\mathrm{TOF}} \sim 10\,\mathrm{ms}$, after which they are imaged with the `cam_y1` camera. The remaining atoms are then released from the trap and also imaged with the same camera after TOF using an optical repumper to bring them at resonance with the probe. The duration of this last TOF expansion is chosen to be long enough to get a sufficiently dilute cloud, where the number of atoms can be counted accurately. The Rabi frequency is then extracted from the period of the oscillations of the relative populations of the two states (see Fig. 2.27). The nonuniform extraction causes a damping of the oscillations due to loss of coherence, which becomes evident for long pulse times, as further explained in Sec. 2.9.6.

The non-destructiveness of PTAI provides an alternative way to measure the Rabi frequency in a single shot. Fig. 2.28 shows the result of a sequence of microwave pulses, each of which extracts the same small fraction of atoms from the trapped sample. The extracted atoms are then imaged after a 4 ms TOF using a camera along y. For each frame the number of extracted atoms is recorded. Applying microwave pulses of duration $\tau_{\mu w} = 1.5\,\mathrm{ms}$, we observe that we can repeat the process up to 20 times before emptying the BEC: the number of atoms indeed decreases by a constant fraction $q \simeq [\sin \Omega\tau_{\mu w}/2]^2$ at each pulse. If N_k is the number of extracted atoms in frame k, after $k+1$ pulses, the relative number of extracted atoms $p_k = N_k/N_0$ follows a geometric series $p_k = (1-q)^k$. From a fit of $p_k(k)$ to this function (solid line in Fig. 2.28(b)), we can extract q and thus Ω. For the data shown in Fig. 2.28 we find a value $\Omega/(2\pi) = 58.8(5)\,\mathrm{kHz}$, in agreement with the results of multishot measurements performed in the same conditions. This

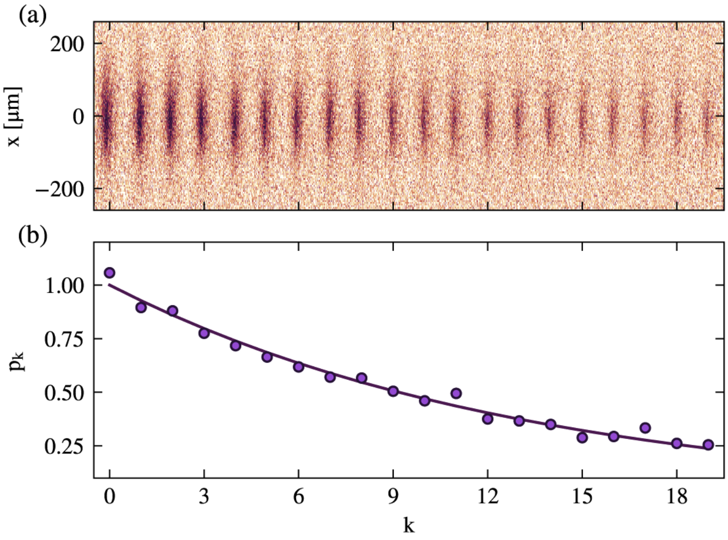

Figure 2.28: (a) Partial-transfer images of the same atomic cloud, taken consecutively using always the same microwave pulse duration. (b) The number of atoms in each frame, with respect to the initial number, decays as a geometric series with the number of extractions. The solid line represents a fit to the function $p_k = (1-q)^k$. Image from [4].

method, besides being faster, has also the advantage of being less sensitive to the spatially dependent detuning. Indeed, for the same intensity of the microwave field, much shorter pulses can be used in this single-shot method, suppressing the effect of the local detuning thanks to Fourier spectral broadening.

2.9.3 Single shot measurement of the trapping frequencies

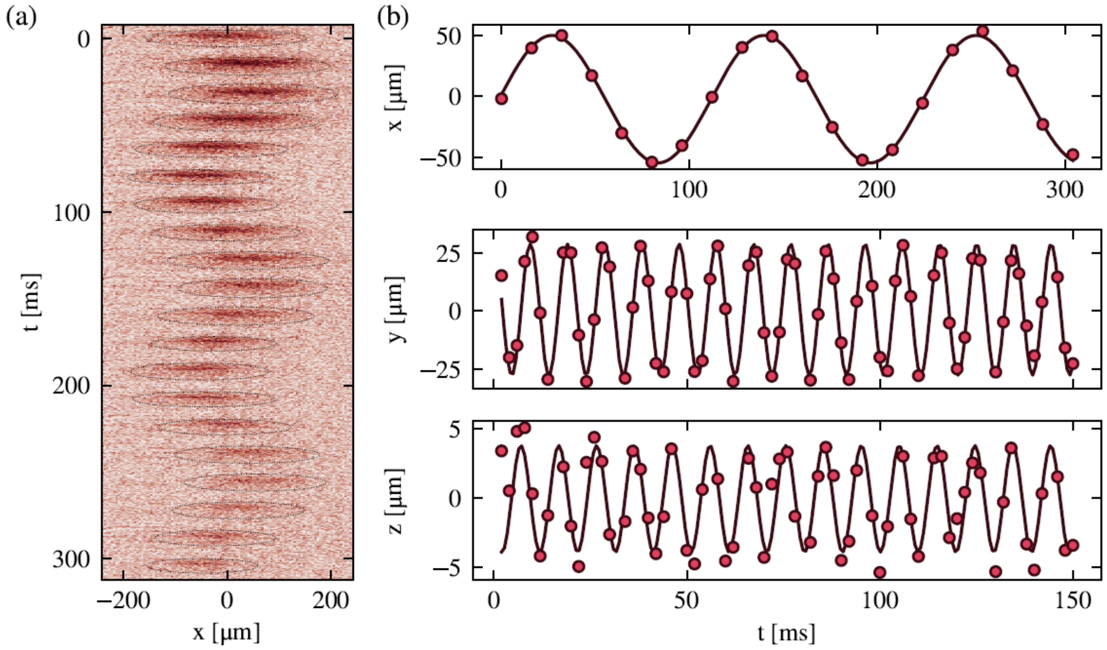

Figure 2.29: (a) Sequence of PTAI images of the same cloud that allow the measurement in a single experimental shot of the trapping frequency along x. (b) From a sinusoidal fit to the center-of-mass oscillation in the three directions, we extract the trapping frequencies. For the x direction, the data points of the single shot shown in (a) are sufficient to extrapolate the trapping frequency, while for the y and z directions, the oscillation is sampled by interleaving the data from a few shots with a delay of 2 ms in the starting time.

The non-destructiveness of the PTAI technique can be exploited in a similar way to measure also other dynamical quantities in a single experimental shot, such as, for instance, the trapping frequencies of the potential confining the atoms.

After briefly displacing the BEC in the trapping potential by means of a magnetic field kick, we sample the oscillation of the center of mass by repeatedly extracting to $|2,-2\rangle$ a small fraction of atoms from the sample every 16 ms, as described in the previous paragraph. In this case, the extracted atoms are imaged using two cameras, along the y and z axis, after a TOF of 4 ms, recording the position of the center of mass in time.

The sampling rate is set by the maximum frame-rate of the camera for the selected height of each image, and is sufficient to measure the axial trapping frequency, but not the radial ones. To obtain also these trapping frequencies, given the reproducibility of the initial conditions, we repeated the experiment a few times, shifting the start time of the sampling by 2 ms each time, and then interleaving the data points to get an effective sampling rate of 500 ms. Fig. 2.29 (a) shows such a sequence of images taken along the y direction during a single experimental run.

The trapping frequencies are obtained by performing a sinusoidal fit to the center of mass oscillation, as shown in Fig. 2.29(b). We find $\omega_x/2\pi = 8.83(2)\,\mathrm{Hz}$, $\omega_y/2\pi = 101.5(7)\,\mathrm{Hz}$, $\omega_z/2\pi = 101.2(1)\,\mathrm{Hz}$, in agreement with the results of multishot measurements, demonstrating the validity of this method, which is particularly suitable for preliminary measurements, given its time-efficiency. From the same measurement one can also obtain again the Rabi frequency with the method described above.

2.9.4 Measurement of the microwave pulse duration

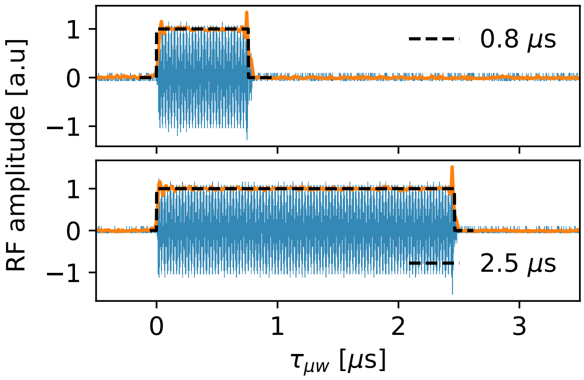

Figure 2.30: Trace (blue) and envelope (orange) of the pick-up signal of the microwave pulse, for $\tau_{\mu w} = 0.8\,\mu\mathrm{s}$ (top) and $\tau_{\mu w} = 2.5\,\mu\mathrm{s}$ (bottom). The black dashed line represents the equivalent rectangular pulse having the same area as the pulse envelope.

In order to correctly estimate the extracted fraction of atoms, we need to accurately know also the duration of the microwave pulse. A non-rectangular pulse-shape can be indeed a source of systematic errors. Using the pick-up antenna mentioned in Sec. 2.4, we directly measure the pulse shape during the experiment. Figure 2.30 shows the trace captured by means of an oscilloscope of the pick-up signal for two different durations of the microwave pulse. Fitting the pulse envelope, we find its rise and fall time, of the order of $\tau \sim 20\,\mathrm{ns}$, corresponding to a deviation from a perfect square pulse of the order of $\tau/t \sim 3\%$ for the shortest pulses ($\tau_{\mu w} \simeq 0.8\,\mu\mathrm{s}$). To eliminate this small systematic source of error, we define the pulse width $\tau_{\mu w}$ as the width of the rectangle with the same area as the pulse envelope, measured in each shot.

2.9.5 HDR reconstruction technique

In this paragraph I explain the technique we developed to reconstruct the in situ optical density profile of the trapped cloud, using multiple PTAI images of the same sample. For these measurements, we produce partially condensed clouds, with a BEC fraction of $\sim 50\%$, to fully demonstrate the dynamical range of the method, and to find the optimum parameters for the EOS measurements, which are performed in similar conditions.

We take a sequence of partial-transfer images of the same cloud, increasing each time the duration of the microwave pulse and thus the effective optical density of the extracted cloud, bringing different regions of the cloud into the optimum range of ODs for our imaging parameters [110]. Short pulses, extracting only a few % of the atoms, allow to accurately image the dense center of the BEC, as shown in the upper panel of Fig. 2.31 (a). The peak OD in the extracted cloud is ~ 5, which is near the saturation limit for

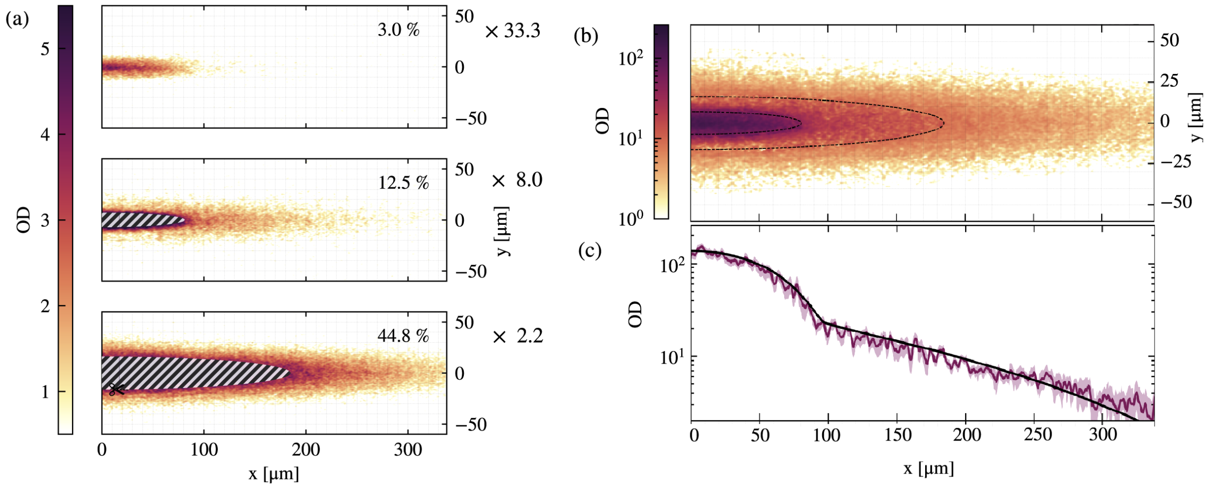

Figure 2.31: (a) Three partial-transfer images of the same sample, taken with the z camera, at different extraction ratios (reported as % in the top right corner of each panel). Each image is rescaled by the inverse of the extraction P_{xy} in the imaging plane. The nominal scaling factors $1/P_0$ are reported on the right, next to each image. The dashed areas represent the cropped-out regions, where the $OD > 4$. (b) HDR image obtained from the weighted mean of the frames in (a). The dotted ellipses correspond to the boundaries of the cropped-out regions in each frame. (c) Profile of a central one-dimensional slice. The black line represents the theoretical profile predicted by Hartree-Fock theory, which well agrees with the experimental data. The OD in the reconstructed profile spans more than two orders of magnitude. Figure adapted from [4].

our imaging conditions. This limit is defined as the value of optical density for which the transmitted probe light becomes of the order of the noise level of the camera. For such short pulses, the thermal tails of the extracted cloud are not visible. Longer pulses are required to image also the tails with high enough SNR, as shown in the two lower panels of Fig. 2.31 (a). In these conditions the central part of the cloud (dashed area) becomes saturated.

The complete image of the atomic cloud is reconstructed combining the information of the various frames in a way inspired by HDR photography. For each frame, we first find the center of the cloud by means of a bimodal fit, then we shift the coordinate axes in order to make the origin always coincide with the common cloud center. We crop away the regions of the cloud that are above the saturation threshold $OD_{\text{th}} = 5$. To avoid the cropping to be biased by the camera noise, and to obtain a smooth edge, we select as cropping region the largest convex hull of pixels where $OD > OD_{\text{th}}$. No cropping is performed on the image at the lowest extraction, since the pulse duration is chosen such that even the densest regions of the cloud remain below the saturation threshold.

To reconstruct the original optical density, the various images are pieced together, after rescaling each image by the inverse of the extraction fraction P_0. To favor the frames with higher SNR in the overlap region, each frame is weighted, in the reconstruction, by its own SNR, where the signal is evaluated from the bimodal fit performed before rescaling, and the noise level is the same in all images, being set by the photonic shot noise. Figure 2.31 (b) and (c) show, respectively, the reconstructed OD and a central one-dimensional slice $OD(x, y = 0)$. The good match in the overlap regions indicates that the rescaling has been performed properly, with consistent scaling factors. In Fig. 2.31 (c) the OD has been fitted to a Hartree-Fock profile (black solid line), to verify that the method yields physically meaningful results. The shaded region around the data represents the errorbar (at one standard deviation), including the statistical noise due to the camera shot noise, the systematic error due to the uncertainty in the Rabi frequency and the effect of the spatial dependence of the detuning along the direction of integration z. Since the various error sources are uncorrelated, we add them in quadrature.

2.9.6 Effect of the non-uniform detuning

As seen above, one of the error sources on the reconstructed OD is determined by the local detuning of the microwave field. This effect can be reduced working at high Rabi frequency Ω and using short pulses $\tau_{\mu w}$. Fig. 2.32 shows, for different values of the Rabi frequency Ω, the relative variation in the extraction fraction in the $y = 0$ plane (a) and in the $z = 0$ plane (b) with respect to the zero-detuning value at the cloud center $P_0 = P(\tau_{\mu w}, \delta = 0)$: $\Delta P/P_0 = [P(\tau_{\mu w}, \delta(x,z)) - P_0]/P_0$, evaluated by combining Eqs.2.35 and 2.36. For each Rabi frequency, the pulsetime $\tau_{\mu w}$ has been chosen such to obtain a nominal extraction of $P_0 = 0.2$ in the center of the condensate. Grey ellipses indicate the size of the BEC (Thomas-Fermi radius, inner solid ellipse) and of the thermal cloud (size of the Bose distribution at 2.5 σ, outer dashed ellipse), of a typical atomic sample used in the measurements of Chapter 3.

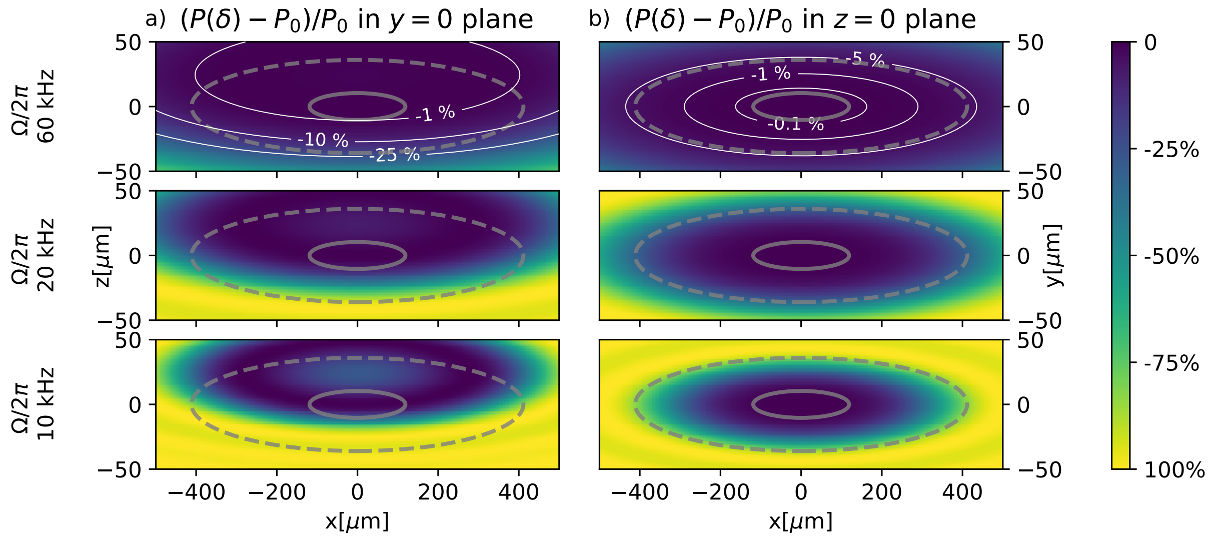

Figure 2.32: Relative variation $\Delta P/P_0 = [P(\tau_{\mu w}, \delta(x,z)) - P_0]/P_0$ of the extraction fraction in the $y = 0$ plane (a) and in the $z = 0$ plane (b), as a function of the spatial coordinates, for different values of Rabi frequency Ω (indicated on the left) and a pulsetime $\tau_{\mu w}$ yielding a nominal extraction of $P_0 = 0.2$ in the center of the condensate. Grey ellipses mark the boundaries of the BEC (solid line) and of the thermal cloud (dashed line). For the highest value of Ω, which has been used in the HDR reconstruction, contour levels have been traced in white to more clearly show the quite small relative variation in the extraction fraction. One can notice the z displacement of the center of the cloud with respect to the center of the magnetic trap, due to the gravitational sag.

For the highest value of the Rabi frequency ($\Omega/2\pi = 60\,\text{kHz}$, upper panels), used for the HDR reconstruction, the relative variation of the extraction in the xy plane (panel b) is below 0.1% at the BEC boundaries and smaller than 5% in the thermal tails of the cloud. This variation can actually be taken into account in the reconstruction, as done in [4], where the OD of each pixel (x, y) of the various PTAI images is weighted by the local extraction fraction $P_{xy} = P(x, y)$ instead of the nominal value P_0. However, for high enough Ω, this variation can be actually neglected, approximating P_{xy} with P_0. Figure 2.32 highlights that this would not be a good approximation for much lower values of Ω. For the same value of $\Omega/2\pi = 60\,\text{kHz}$, the variation $\Delta P/P_0$ in the xz plane is much more relevant for two reasons. The first reason is that in the region occupied by the atomic cloud, the absolute value of the variation in the xz ($y = 0$) plane is much larger than that in the xy plane, since the main contribution in Eq. 2.36 is given by the gravitational sag term $\propto z$. In the upper panel of Fig. 2.32 (a), we notice that for the Rabi frequency used for the HDR reconstruction, there is a maximum relative variation of the extraction of the order of 1% in the region occupied by the BEC, while for the thermal tails, the top to bottom difference becomes larger than 20%. The other reason that makes this variation more relevant is that the cloud is imaged along z, and thus the local variation of the extraction modifies the OD of the imaged cloud in the direction of integration. This means that the effect of the nonuniform detuning along the z direction cannot simply be factored out considering a spatially dependent extraction factor, as in the xy plane. To quantify the systematic error on the OD, we evaluate the integral:

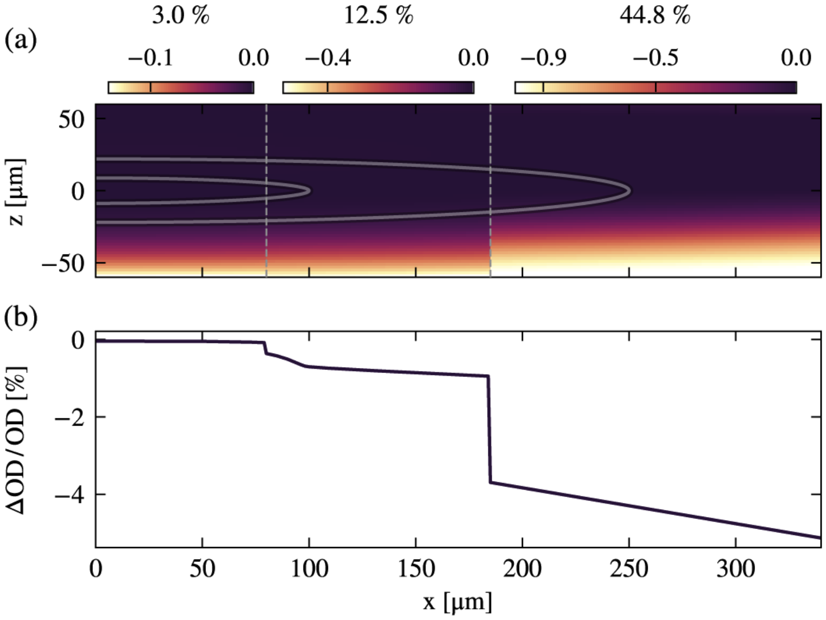

Figure 2.33: (a) Map of the relative variation in the extraction $\Delta P/P_0$ in the xz plane, evaluated for the parameters used in the HDR reconstruction. The three parts of the image, separated by the dashed lines, correspond to the non-cropped regions of the three frames, in each of which a different pulsetime $\tau_{\mu w}$ has been used. Notice that the scale of the colormap is different in the three sections in order to highlight the great difference in the spatial variation of the extraction. (b) Relative error in the optical density caused by the nonuniform extraction, calculated according to Eq. 2.37.

$$\Delta\text{OD} = \int \frac{P(\tau_{\mu w}, \delta) - P_0}{P_0} n dz, \tag{2.37}$$

where n is the atomic density profile, obtained from the Hartree-Fock fit of the reconstructed OD of Fig. 2.31. Figure 2.33(b) shows the relative error on the optical density $\Delta\text{OD}/\text{OD}$ along the x axis. Although the variation of the extraction is largest in the thermal tails, the small density in these regions strongly reduces their contribution to the total error in the OD, which remains below 1% in the region occupied by the condensate and below 5% for the whole atomic distribution.

Figure 2.33(a) highlights that for increasing microwave pulsetimes, the effect of the inhomogeneous transfer becomes more and more evident. If we measure the Rabi frequency with the standard multishot technique, where the fraction of transferred atoms is measured as a function of the pulsetime (see Sec. 2.9.2), this effect needs to be taken into account. Due to the local detuning, the transferred fraction of atoms has a damped oscillation.
The fraction of extracted atoms after a pulse of duration $\tau_{\mu w}$ can, indeed, be written as:

$$\tilde{P}(\tau_{\mu w}) = \frac{N_2}{N_1 + N_2} = \frac{1}{N}\int P[\tau_{\mu w}, \delta(r)]n(r)d^3r \tag{2.38}$$

where N_1 is the number of atoms remaining in $|F=1\rangle$ and N_2 the number of atoms transferred to $|F=2\rangle$, with $N = N_1 + N_2$ the total number of atoms. To quantify the effect of the inhomogeneous detuning, we approximate the density distribution $n(r)$ with a Gaussian and consider only the dominant term due to the gravitational sag in Eq. 2.36[7]. Integrating along x and y, we get:

$$\tilde{P}(\tau_{\mu w}) = \frac{1}{\sqrt{2\pi}\Delta_0}\int P(\tau_{\mu w}, \delta)e^{-\delta^2/2\Delta_0}d\delta, \tag{2.39}$$

where Δ_0 is the range of detuning spanned by the atomic cloud, which for the Rabi frequency used for the reconstruction is equal to $\Delta_0/2\pi \simeq 20\,\text{kHz}$, for a BEC with a Thomas-Fermi radius $R_z \simeq 12\,\mu\text{m}$. The integral in Eq. 2.39 can be solved analytically, yielding the function used in the fit of Fig. 2.27:

$$\tilde{P}(\tau_{\mu w}) = \frac{1}{2\sqrt{1+2D^2}}\left(1 - \frac{\cos\left[T + \arctan(b)/2\right]}{(1+b^2)^{1/4}}\right) \tag{2.40}$$

with $D = \Delta_0/\Omega$, $T = \Omega\tau_{\mu w}$, $b = TD^2/(1+2D^2)$. Without the effect of the local detuning (i.e., if $\delta = 0$ in the whole cloud), the oscillation would maintain constant amplitude, following the function: $P(\tau_{\mu w}, \delta = 0) = [\sin\tau_{\mu w}\Omega/2]^2$. The damping of the oscillation becomes evident for long pulsetimes and low values of Ω, as shown in Fig. 2.34.

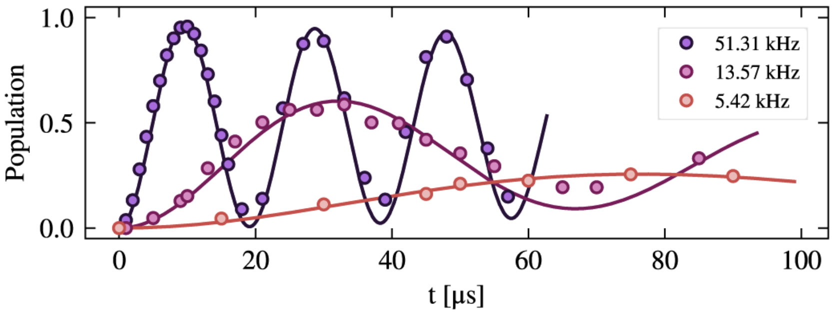

Figure 2.34: Population of the $F = 2$ state as a function of the microwave pulsetime, for different values of Ω. For long pulsetimes, the amplitude of the oscillation decreases because of the loss of coherence caused by the local detuning.

---

[7] In this approximated calculation, we consider the detuning as uniform along the x and y directions, which is justified by the fact that the relative variation of the extraction is much smaller along the x and y directions than along z, as can be noticed from Fig. 2.32(a-b).

2.9.7 Side effects: excitation of collective modes

The extraction process can excite collective modes in the BEC, potentially distorting the density profile. The dipole mode just shifts the center of mass of the BEC, without changing its shape: the BEC can be simply recentered without any problems of distortion as long as the displacement is perpendicular to the imaging axis, while if it is along the imaging direction, focusing errors might arise. However, also higher order modes are naturally excited by multiple microwave extractions, such as the quadrupole mode. Figure 2.35 shows the variation of the Thomas-Fermi radius R_x, normalized by the value before the first extraction, for different extraction fractions. We notice that the relative variation of R_x becomes appreciable for extraction fractions above 5%. This effect gets hidden by arranging the sampling frequency to match the oscillation frequency, in a way that all the subsequent images are consistent. Another option is to perform the extraction and imaging process before any quadrupole oscillation can take place: indeed, if the sampling frequency is much faster than the mode frequency, the shape of the BEC is essentially frozen in all frames. Our cameras, however, have a limited frame rate: if the full sensor area is acquired, there must be a minimum delay of 70 ms between the start of two consecutive exposures [112]. In the above described HDR reconstruction, we take three frames at different extraction fractions ($\sim$ 3.5%, $\sim$ 12.5%, $\sim$ 44.8%). In this case, the effect of the quadrupole mode excitation is minimized if we first take the frame at lowest extraction fraction, which causes an almost negligible perturbation. The other two images are taken 70 ms later, but with the two microwave (and probe) pulses only 600 µs apart (at the end and at the beginning of the two exposures of the camera, respectively). Between the two pulses, we remove the atoms that have been already imaged by illuminating them with a 5 µs probe pulse along y, which pushes them away from the line of sight of the z imaging. This sequence minimizes the effect of the quadrupole mode excitation on the images.

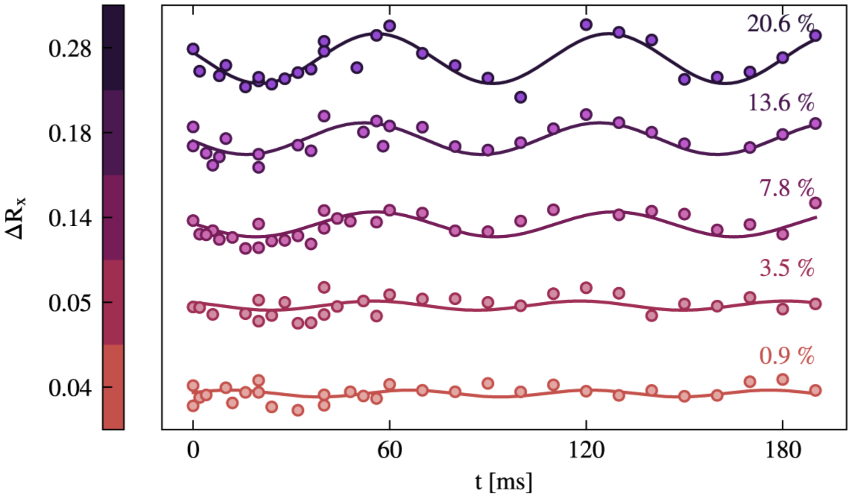

Figure 2.35: Quadrupole oscillation of the condensate caused by multiple extractions. The amplitude of the oscillation increases with the extraction fraction, reported on the right of each plot.

2.9.8 Side effects: off-resonant scattering

The probe light is resonant with the $F = 2 \rightarrow F' = 3$ transition, to image the atoms that have been transferred to the $F = 2$ state. The remaining atoms in the $F = 1$ state, however, interact off-resonantly with the probe light, with a detuning of 1.77 GHz. This interaction can in principle cause a depletion of the atomic reservoir, leading to systematic errors in the measurement of the number of atoms in the subsequent images. The imaging intensity used in our experiment ($I/I_{sat} \simeq 4$), anyway, leads to an off-resonant scattering rate of the order of $10^3\,\mathrm{s}^{-1}$, making the losses negligible for probe pulses of a few μs duration.

2.9.9 Conclusions & considerations on the PTAI+HDR method

In the Sections above I explained how we implemented a method based on PTAI and HDR reconstruction to obtain the full optical density profile of a partially condensed cloud, with a high dynamic range of ODs, from $\sim 10^{-1}$ to $\sim 10^2$. The strengths and weaknesses of performing multiple extractions on the same trapped cloud were investigated. Namely, we found an efficient way to follow dynamical processes and measure characteristic quantities, such as the trapping frequencies and the microwave Rabi frequency, in a single shot. We found optimum parameters to reconstruct the column density profile using three images of the same trapped sample. The final reconstructed profile is sufficiently smooth in the overlap regions, and well agrees with a theoretical Hartree-Fock profile. The effect of the local variation of the detuning, caused by the nonuniform magnetic field and by the gravitational sag, was taken into account in the estimation of the extraction fraction and the related error on the reconstructed OD was computed. This method was used, in first instance, to reconstruct the column density for the EoS measurements. However, the potential distortions in the profile caused by the excitation of quadrupole modes for multiple extractions, together with the need of taking anyhow more experimental shots for statistical reasons, made us change the final procedure. For the measurements reported in Chapter 3, we still use the HDR reconstruction technique described above, but - profiting from the equilibrium state of the system - the images are obtained by repeating the experiment in identical conditions, taking only a single *in situ* PTAI image of each cloud, at several variable extraction ratios yielding an optimum SNR in all regions of the sample. Its high dynamic range makes our technique suitable for the imaging also of other dense objects, such as, for instance, quantum droplets [150, 151, 152].

Chapter 3

Bose gas in equilibrium: measurement of the equation of state

3.1 Introduction

In this chapter I present our results regarding the measurement of the equation of state (EoS) of a 3D homogeneous weakly interacting Bose gas. An EoS is a relation between three thermodynamic quantities, from which the full thermodynamic properties of the system at equilibrium can be derived.

So far, experimental measurements on the EoS of Bose gases both in 2D [153, 154] and in 3D [3, 155] have been obtained in the grand-canonical approach, where the pressure of the uniform gas is expressed in terms of the chemical potential and the temperature. This approach has enabled important observations, such as the identification, in a Bose gas at zero temperature, of the Lee-Huang-Yang correction to the EoS, originating from beyond-mean-field quantum fluctuations [156]. Our aim is to find the EoS directly in the canonical framework, where the pressure $p(v, T)$ is expressed as a function of the specific volume $v = 1/n$, at constant temperature T and fixed scattering length a.

In our experiment the atomic sample is confined in a nonuniform trapping potential. Nevertheless we can use it to extract the thermodynamic behavior of uniform matter by applying the local density approximation (LDA). As explained in Sec. 1.1.6, the LDA establishes a connection between the local properties of the nonuniform system and the bulk properties of the corresponding homogeneous system, assuming an effective local chemical potential:

$$\mu(x, y, z) = \mu_0 - V_{ext}(x, y, z) \tag{3.1}$$

where μ_0 is the chemical potential in the center of the trap and V_{ext} the non-uniform trapping potential. Using the LDA, the non-uniformity of the system becomes for us an advantage, rather than a problem. From the measurement of the column density, we extract the on-axis density profile $n(x) = n(x, 0, 0)$. The variation of the density along the x axis corresponds to a spatial variation of the reduced temperature $T/T_c(x)$, at fixed T. This enables us, in principle, to extract the full EoS from images of a single partially condensed cloud which can be considered as a continuous ensemble of homogeneous systems at different reduced temperatures. We study the dependency of the chemical potential on the reduced temperature, observing a non-monotonic behavior, with the presence of a peak around the critical point. Such a peak was already observed in other superfluid systems, such as Fermi gases [157], and in the thermodynamic behavior of liquid Helium

[158], suggesting that it could be a general signature that characterizes transitions from the normal to superfluid phase. We provide a first observation of the presence of this peak in the chemical potential also for the weakly interacting Bose gas, where this behavior is predicted by HF theory.

Finally we derive also the grand-canonical equation of state, finding good agreement with previous results [3].

The role of interactions in the thermodynamics of the Bose gas clearly emerges in this study: it becomes evident, for instance, observing the major differences between the EoS of our weakly interacting Bose gas and the model EoS of an ideal, non-interacting Bose gas. We also observe the predicted interaction-induced shift of the critical point.

The achievement of these results was possible thanks to technical improvements in the setup and in the experimental procedures. The measurement of the *in situ* density of the 3D condensed gas, which spans over three orders of magnitude, was performed using the partial-transfer absorption imaging technique (PTAI) and the HDR reconstruction method described in Sec. 2.9 and in our paper [4]

The upgrade of the imaging system, with the achievement of a higher resolution was highly beneficial for this measurement, since it enabled an accurate study of the thermodynamic behavior even in the critical region, which corresponds to a rather narrow spatial range of the density profile, and it allowed a clear observation of the predicted peak in the chemical potential.

3.2 Experimental procedure

Through RF evaporation in the magnetic trap, a partially condensed cloud is produced, as described in Chapter 2. Lowering the current in the magnetic trap coils to 50 A in the final stages of the evaporation yields a quite shallow, harmonic confining potential, with trapping frequencies of $\omega_x/2\pi = 8.83(2)\,\mathrm{Hz}$ and $\omega_r/2\pi = 100.8(7)\,\mathrm{Hz}$, which were measured both with the single-shot technique reported in Sec. 2.9.3 and with the standard multi-shot method. At the end of the RF evaporation ramp we hold the atoms in the shallow magnetic trap, without evaporating further, and wait for 2 s to ensure that thermodynamic equilibrium has been reached in the atomic cloud well before the time at which we image it. Acting on the evaporation ramp parameters, we tune the final condensate fraction and temperature. In order to optimize the signal-to-noise ratio, we choose to work with a condensate fraction of about 50%.

To image the cloud *in situ*, we apply the PTAI technique described in Chapter 2, which yields a good signal-to-noise ratio in the full range of ODs spanned by the atomic cloud.

We use a microwave field of Rabi frequency $\Omega/2\pi = 60.2(2)\,\mathrm{kHz}$ to outcouple a small, tunable, fraction of the atoms from the magnetically trapped $|F, m_F\rangle = |1, -1\rangle$ state to the non-trapped $|2, -2\rangle$ state. The extracted atoms are then imaged along the z direction with the `cam_z1` camera, using a π-polarized probe pulse of duration $\tau_p = 5\,\mu\mathrm{s}$, resonant with the $F = 2 \rightarrow F' = 3$ cycling transition, with an intensity $I/I_{sat} = 4$, as described in Sec. 2.7.4. The extraction and imaging process has a total duration of less than 10 µs, allowing us to safely neglect losses caused by spin-flipping collisions, which could in principle occur given the probe polarization.

We repeat the experiment multiple times in identical conditions, tuning the duration $\tau_{\mu w}$ of the microwave pulse to extract a different fraction $P(\tau_{\mu w})$ of atoms from the sample, as described in Sec. 2.9.

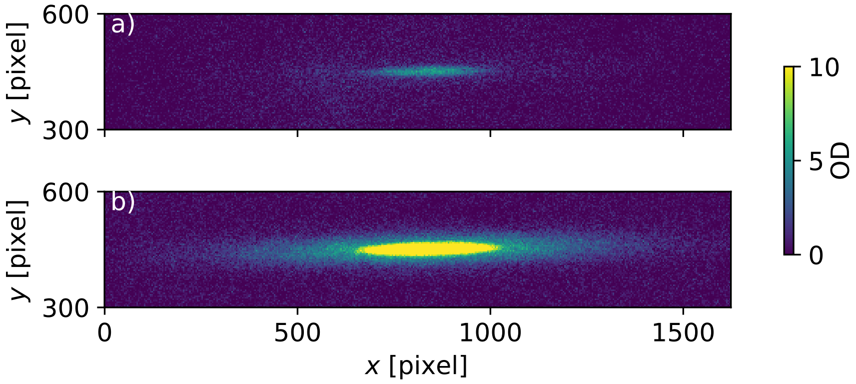

Figure 3.1: Optical density of the trapped Bose gas imaged extracting a different fraction of atoms, by means of different microwave pulse durations $\tau_{\mu w}$. (a) For $\tau_{\mu w} = 0.8\,\mu\mathrm{s}$, corresponding to an extraction of $\sim 2.3\%$, we are able to image the central region of the condensate, where the column density is the highest, without saturation. However, the thermal tails are barely visible. (b) Using a longer microwave pulse $\tau_{\mu w} = 2.5\,\mu\mathrm{s}$, corresponding to an extraction of $\sim 20.6\%$, we manage to accurately image also the tails. The central saturated part, where $OD > 5$ is discarded in the reconstruction of the total column density profile.

Short pulses allow to extract a small fraction of atoms (between 1 and 8%) and accurately image the dense condensate core at the center of the sample, without saturation problems, as shown in Fig. 3.1 (a), where the optical density always remains below the saturation threshold $OD < OD_{th} = 5$. In these images the much more dilute thermal tails are, however, barely visible and suffer from a poor signal-to-noise ratio (SNR). In order to improve the SNR, we also take images where we extract a higher fraction of atoms (up to 20%) in order to increase the absorptive signal, as shown in Fig. 3.1 (b). In these images, the dense central region (shown in yellow) is saturated, while the low-density tails are accurately imaged with high signal-to-noise ratio. We crop each image as described in Sec. 2.9 in order to retain only the non-saturated part. Each image is then rescaled by the corresponding extraction fraction to correctly estimate the original column density.

The various rescaled images are then averaged together after recentering them so that the origin of the x axis is always at the center of the BEC and cropping them to the area that contains the atomic cloud. The resulting column density $n_1(x, y)$ is shown in Fig. 3.2, where each pixel is obtained from the average of 5 up to 80 images.

We could in principle extract the EoS from just one experimental run, reconstructing the column density from multiple PTAI images of the same cloud, taken consecutively at increasing extraction fractions, directly applying the procedure that was used to obtain Fig. 2.31 in Sec. 2.9. However, in Fig. 2.35 we noticed that the microwave extraction perturbs the density distribution of the sample by exciting the quadrupole mode. This could introduce systematic errors in the estimation of the density from images taken after the first one. Although these errors would be small for low extractions (see Fig. 2.35), we prefer to avoid them by repeating instead the experiment, taking only one in-situ image for each experimental realization.

After imaging the sample in situ, we release the remaining atoms from the trap and let them expand for a time of flight $t_{TOF} = 50\,\mathrm{ms}$, after which we image them along y with the `cam_y1` camera to measure the temperature from the width of the thermal cloud. We checked that the previous microwave extraction has no significant effect on

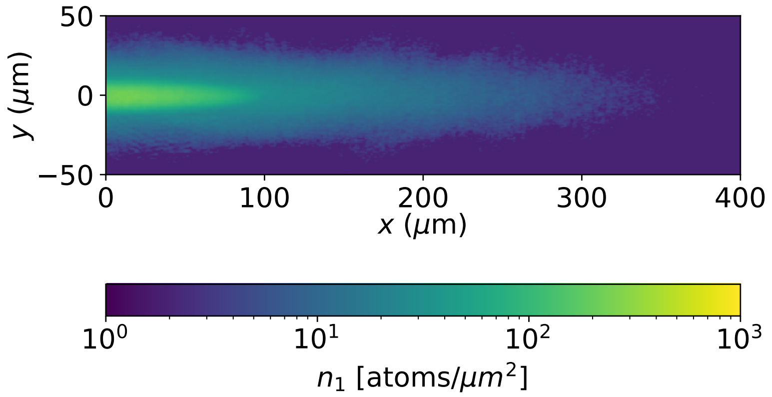

Figure 3.2: Column density of the trapped Bose gas, reconstructed from multiple images taken at different partial extractions. Each pixel of this figure is obtained from the average of 5 to 80 images at different extraction ratios. Given the symmetry, we show only the $x \geq 0$ half, where $x = 0$ corresponds to the center of the sample.

this measurement.

3.3 Obtaining the relevant thermodynamic quantities

In this Section I explain how the relevant thermodynamic quantities are extracted from the images of the atomic cloud.

3.3.1 Pressure

The pressure along the x axis of the trapped sample $p(x) \equiv p(x, y = 0, z = 0)$ can be directly obtained from the column density $n_1(x, y)$ of the reconstructed in-situ image, following a method proposed by [159, 160] and already implemented in [161, 3, 162, 163]. The starting point is the Gibbs-Duhem thermodynamic relation [164]:

$$dp = nd\mu + sdT, \tag{3.2}$$

where s is the entropy density and μ the chemical potential. Integrating Eq. 3.2 at constant temperature, and knowing that $p(-\infty) = 0$, we can write:

$$p(x) = p(x, y = 0, z = 0) = \int_{-\infty}^{\mu(x)} n(\mu)d\mu. \tag{3.3}$$

We use the LDA relation for the chemical potential:

$$\mu = \mu_0 - V_{ext}, \text{ with } V_{ext} = \frac{1}{2}m(\omega_x^2 x^2 + \omega_y^2 y^2 + \omega_z^2 z^2), \tag{3.4}$$

where μ_0 the chemical potential in the center of the trap and V_{ext} the trapping potential. For a given x, one can write $d\mu$ as [160]:

$$d\mu = -dV_{ext} = -\frac{m\omega_y\omega_z}{2\pi}dydz, \tag{3.5}$$

which finally yields the following expression for the pressure along x:

$$\begin{aligned} p(x) &= \int_{V_{ext}(x)}^{\infty} n(\mu_0 - V_{ext}) dV_{ext} = \\ &= \frac{m\omega_y\omega_z}{2\pi} \int\int n(x,y,z) dy dz = \frac{m\omega_\rho^2}{2\pi} \int n_1(x,y) dy. \end{aligned} \tag{3.6}$$

This equation shows that the pressure $p(x)$ can directly be obtained by integrating along the y axis the measured column density $n_1(x,y) = \int n(x,y,z)dz$. Performing this integration on the column density profile of Fig. 3.2, we obtain the pressure profile shown in Fig. 3.3.

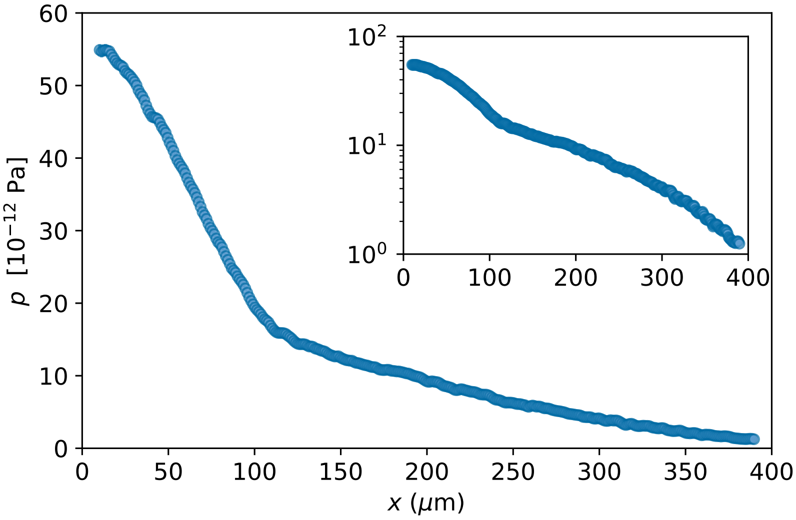

Figure 3.3: Pressure $p(x)$ along the x axis of the trapped sample. The inset shows the same plot with the pressure axis in logarithmic scale.

3.3.2 Density

To obtain the canonical EoS, which relates the pressure to the density n and to the temperature T, we need to find the density profile along the x axis, $n(x) \equiv n(x, y = 0, z = 0)$. For this scope, we tested two different methods.

The first method exploits again the Gibbs-Duhem relation of Eq. 3.2, following the proposal of [160], and consists in finding the density via the numerical derivative of the pressure:

$$\begin{aligned} n &= \left(\frac{\partial p}{\partial \mu}\right)_T = -\left(\frac{\partial p}{\partial x}\right)\left(\frac{\partial \mu}{\partial x}\right)^{-1} = \\ &= -\frac{1}{m\omega_x^2 x}\frac{\partial p}{\partial x} = -\frac{\omega_\rho^2}{\omega_x^2}\frac{1}{2\pi x}\frac{\partial(\int n_1(x,y)dy)}{\partial x}, \end{aligned} \tag{3.7}$$

where the LDA relation for the chemical potential has been used, and in the last expression the pressure p has been written according to Eq. 3.6.

The second method to retrieve the on-axis density exploits, instead, the axial symmetry of the system to find the density through the inverse Abel transform or Abel inversion

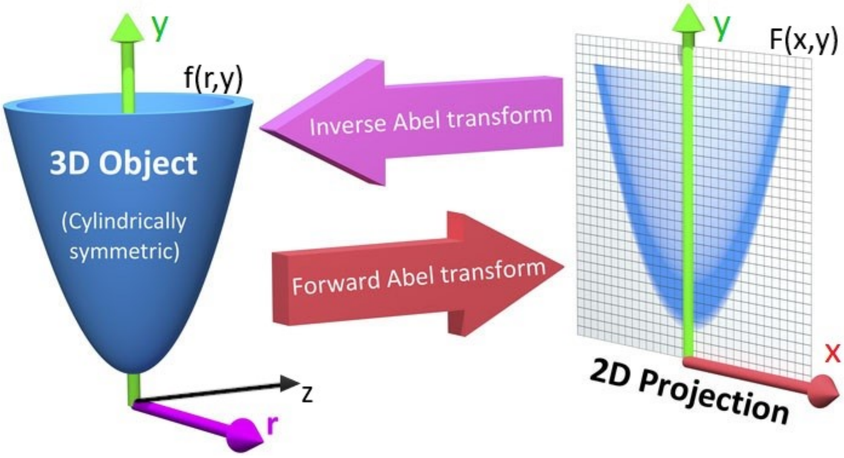

Figure 3.4: Forward and inverse Abel transform, adapted from [165]. As in the text, $r = \sqrt{x^2+z^2}$ and z is the direction of the line of sight. The symmetry axis y lies in the image plane.

[166, 167, 168]. This is a powerful tool that allows to retrieve a 3D cylindrically symmetric distribution from its 2D image. It has been used in various fields, including photoelectron spectroscopy [169, 170], the study of the emissivity distributions of plasmas [171, 172], flames [173, 174], planetary and cometary atmospheres [175, 176], as well as the imaging of ultracold atomic clouds [177, 178, 157, 125, 179].

The imaging process intrinsically involves a forward Abel transform. This transformation takes a 3D cylindrically symmetric distribution $f(x, y, z) = f(r, y)$ (with $r = \sqrt{x^2+z^2}$) and yields a 2D projection $F(x, y)$, as shown in Fig. 3.4, via integration along a line of sight, in this case z, perpendicular to the symmetry axis. The projection $F(x, y)$ given by the forward Abel transform, can be, in general, written as:

$$F(x, y) = \int_{-\infty}^{+\infty} f(x, y, z) dz = 2 \int_{x}^{\infty} \frac{f(r, y) r}{\sqrt{r^2 - x^2}} dr. \tag{3.8}$$

Rearranging this equation for $f(r, y)$, one obtains the inverse Abel transform, that allows to retrieve a slice of the cylindrically symmetric 3D distribution $f(r, y)$ from the projection $F(x, y)$:

$$f(r, y) = -\frac{1}{\pi} \int_{r}^{\infty} \frac{\partial F(x, y)}{\partial x} \frac{1}{\sqrt{x^2 - r^2}} dx. \tag{3.9}$$

Although Eqs. 3.8, 3.9 can be evaluated analytically for some mathematical functions, experimental data are affected by the discrete nature of the pixels of the camera, and subject to noise, requiring a numerical evaluation of the inverse transform. Several algorithms have been developed for this purpose, the main issues being the need for computationally efficient algorithms and the necessity to obtain reliable results even in presence of noise. The treatment of noise is, indeed, particularly delicate since the numerical differentiation operation propagates and enhances noise-fluctuations at high-spatial frequencies.

In our case the atomic cloud has an ellipsoidal shape, with more than one axis of symmetry. The density distribution $n(x, y, z)$, besides being circularly symmetric around the x axis thanks to the geometry of the IP trap ($\omega_y = \omega_z = \omega_\rho$), has a cylindrical symmetry also around any of the principal axes of the ellipsoid, for instance around the y axis, after rescaling the x coordinate by the aspect ratio $\lambda = \omega_\rho/\omega_x$ of the trapping potential : $n(x, y, z) = n(r, y)$, with $r = \sqrt{(x/\lambda)^2 + z^2}$.

Using the inverse Abel transform, starting from the projection $n_1(x, y)$, we retrieve the central slice $n(x, y, z = 0)$, that contains, thanks to the cylindrical symmetry, all the information of the original 3D atomic density distribution. Since we are interested in the on-axis density $n(x, y = 0, z = 0)$, to increase the signal-to-noise ratio, we can further exploit the symmetry of the trapping potential and azimuthally average the obtained density over elliptical iso-density lines. To avoid beyond-LDA effects, which modify the density profile and are stronger further away from the axis, we compute this average considering only the points within a small angle (±10°) around the x axis.

The axial density profile $n(x) = n(x, y = 0, z = 0)$ resulting from the Abel inversion is shown in Fig. 3.5.

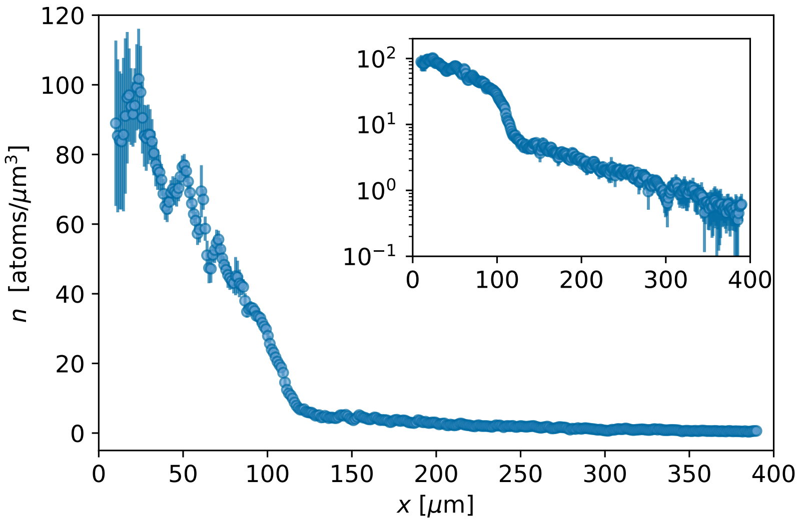

Figure 3.5: Density $n(x)$ along the x axis of the trapped sample, obtained applying the inverse Abel transform to the reconstructed column density of Fig. 3.2. The inset shows the same plot with the axis of ordinates in logarithmic scale.

We tested both the approach based on the Gibbs-Duhem equation (GD) and the one based on the inverse Abel transform, to get the density profile from the experimentally measured column density. The critical issue in both cases is the calculation of numerical derivatives (see Eqs. 3.7 and 3.9), which amplify the noise at high spatial frequencies. In case of the GD approach this problem is mitigated implementing a smooth numerical differentiation based on the central difference scheme, which allows for a tunable degree of smoothing depending on the size N of the averaging window [180]. For the inverse Abel transform, noise is treated, as stated before, by using the recursive Hansen-Law algorithm [181], in the version implemented in the PyAbel Python package, which includes noise-reduction operations (Kalman filter) [168, 165]. In addition, the effect of noise is reduced by azimuthally averaging the reconstructed 2D density slice. A comparison between the density profiles obtained with the two methods is shown in Fig. 3.6a. We decided to use the Abel transform because it yields a low-noise profile, while still preserving local sharp features, which are fundamental for an accurate study of the behavior in the critical region (see Fig. 3.6b and the related discussion in Sec. 3.4).

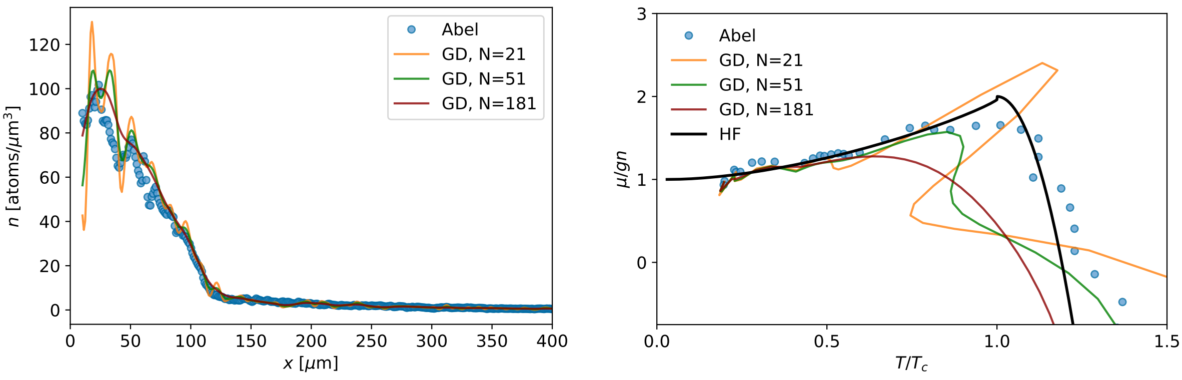

(a) (b)

Figure 3.6: Comparison of the axial density profile (a) and chemical potential Vs reduced temperature (b), obtained using the Abel transform (blue dots) or the GD method, with different lengths N of the filter window (solid lines). For low N, high-frequency fluctuations appear in the GD density profiles (orange and green lines) due to the amplification of noise in the differentiation, yielding unphysical features in the corresponding reduced chemical potential profile. Higher N provides a higher degree of smoothing, mitigating such high-frequency fluctuations of the density, but also smears out local sharp features, washing out almost completely the peak in the chemical potential, with an effect equivalent to a worsening of the spatial resolution. Intermediate values of N were also tested, but did not yield better results for the GD method compared to the Abel transform.

3.3.3 Temperature

The temperature T of the sample is found independently, using the images taken after a $t_{TOF} = 50\,\mathrm{ms}$ time-of-flight expansion. We fit the column density distribution with a 2D bimodal function, as described in Sec. 2.8 and extract the temperature from the widths σ_x and σ_z of the thermal distribution, using Eq. 2.34 to account for hydrodynamic corrections to the ballistic expansion. Also the total number of atoms in the cloud is obtained from the TOF image and is compared with the number estimated from the PTAI images, to check the consistency of the calibration of the extracted fraction.

The temperature of the samples was tuned by changing the final evaporation frequency of the second exponential ramp in Fig. 2.10. For the derivation of the EOS we use samples with a temperature $T = 280$ nK, where the condensate fraction is about 50%[1]. Post-selection on the data was performed, eliminating the shots where the temperature or atom number deviated significantly from the average or were not consistent with the atom number obtained from the PTAI measurements.

From the measured temperature T and the axial density distribution $n(x)$, we find the local reduced temperature $T/T_c(x)$, where $T_c(x)$ is the critical temperature, estimated using Eq. 1.42:

$$T_c(x) = \frac{2\pi\hbar^2}{mk_B}\left(\frac{n(x)}{\zeta_{3/2}}\right)^{2/3}. \tag{3.10}$$

In Fig. 3.7 the reduced temperature is shown as a function of the axial coordinate x. At the center, where the density is maximum, $T/T_c \sim 0.2$, while in the thermal tails it rapidly becomes much larger than 1. The inset clarifies the fact that the critical region

---

[1] Measurements on colder samples, with a temperature $T \sim 150\,\mathrm{nK}$ and an almost negligible thermal part, were also performed. They are shown in Sec. 3.4.3

around $T/T_c \simeq 1$ corresponds to a quite narrow spatial region (T/T_c varies from 0.75 to 1.25 in less than $20\,\mu\mathrm{m}$). This makes the study of the behavior near the critical point rather challenging, motivating our efforts to increase the spatial resolution and to find suitable techniques to treat the noise without excessively smoothing out local features in the density data.

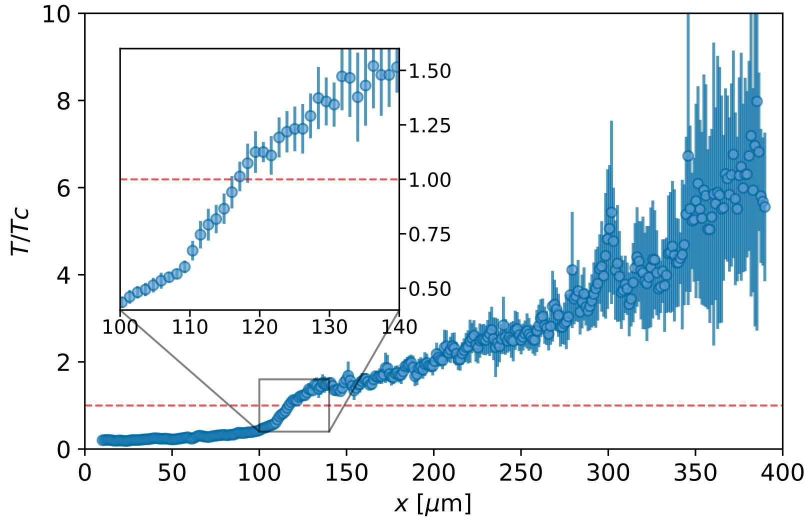

Figure 3.7: Reduced temperature $T/T_c(x)$ for $T = 280\,\mathrm{nK}$ and $T_c(x)$ calculated from the density $n(x, 0, 0)$, plotted as a function of the axial coordinate x. The inset is a zoom of the region around $T/T_c = 1$ (red dashed line).

3.4 Results

In the following I show the main results that we obtained regarding the measurement of the thermodynamic properties of the Bose gas.

3.4.1 Canonical EOS

We obtained the EoS of the uniform Bose gas in canonical variables, determining a relation $p(v, T)$ between the volume, the pressure and the temperature of the ultracold gas, like the well-known classical ideal gas law.

From the density profile $n(x)$, we find the specific volume $v(x)$:

$$v(x) = \frac{1}{n(x)}. \tag{3.11}$$

At the critical point, the specific volume v_c is obtained from the definition of the critical temperature (Eq. 1.42):

$$\frac{v}{v_c} = \left(\frac{T}{T_c}\right)^{3/2} \rightarrow v_c = \frac{1}{n_c} = \frac{\lambda_T^3}{\zeta_{3/2}}. \tag{3.12}$$

where λ_T is the De Broglie wavelength (Eq. 1.1). We also calculate the critical pressure, from the IBG formula Eq. 1.52:

$$p_c = \frac{\zeta_{5/2} k_B T}{\lambda_T^3}, \tag{3.13}$$

Using the pressure and density profiles $p(x)$ and $n(x)$ of Figs. 3.3, 3.5, rescaled by the critical values, we obtain the canonical EOS $p(v)$ in reduced variables p/p_c and v/v_c, at fixed temperature $T = 280\,\text{nK}$, which is shown in Fig. 3.8.

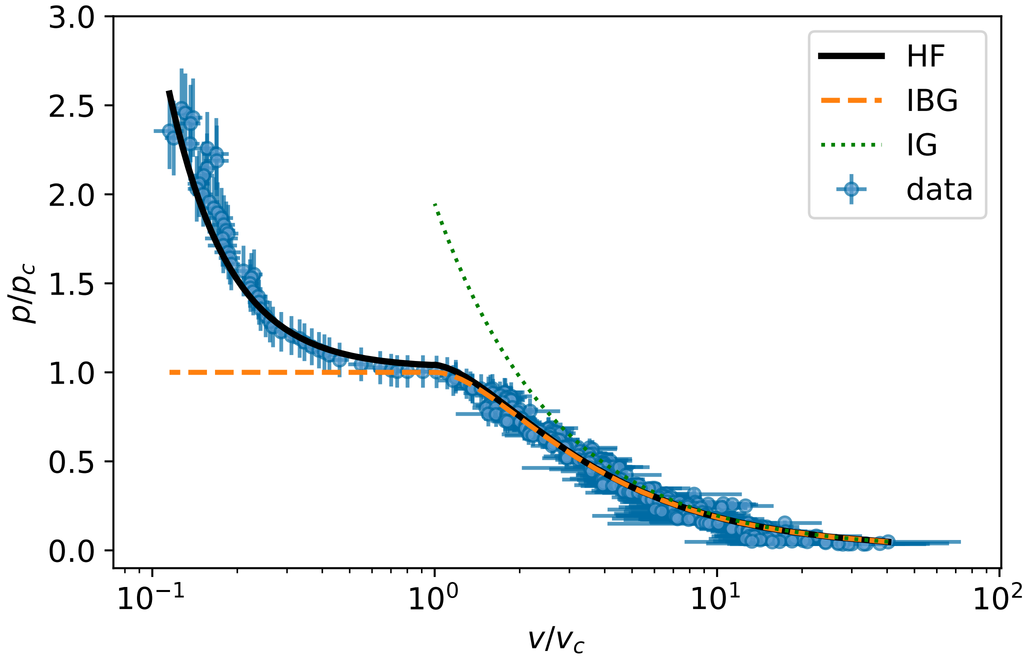

Figure 3.8: Canonical equation of state $p(v)$.

For $v/v_c > 1$, the prediction of the classical ideal gas law $p = k_B T/v$ is shown (IG, green dotted curve). We observe that this curve captures the behavior of the Bose gas only at high temperatures, i.e. for $v/v_c \gg 1$, showing the importance of quantum effects in the vicinity of the critical point.

The prediction for the non interacting Bose gas is also shown (IBG, orange dashed line). This curve correctly captures the experimental behavior until the critical point. For $v < v_c$ the measured pressure strongly increases, instead of remaining equal to the critical value as predicted by the IBG model of Eq. 1.52. This behavior highlights how the thermodynamics is dominated by the effect of the interactions, not included in the IBG model.

Let us now compare the experimental data with the EoS predicted by Hartree-Fock for the uniform interacting Bose gas. The HF pressure profile for the uniform Bose gas, given by Eq. 1.54

$$p = gn^2 - \frac{1}{2} g n_0^2 + \frac{k_B T}{\lambda_T^3} g_{5/2}[e^{(\mu - 2gn)/k_B T}],$$

is shown in Fig. 3.8 as a solid black line. It was evaluated using the density profile data $n(x)$ and the measured temperature $T = 280\,\text{nK}$, without any fitting parameters.

An excellent agreement can be observed between this curve and the experimental data, which confirms the validity of the mean field approach for the description of a weakly interacting gas and of our LDA approach.

This agreement also holds for $v \ll v_c$, where the HF model predicts a divergence of the pressure as $(\xi_{3/2}^2/\xi_{5/2})(a/\lambda_T)(v/v_c)^2$ for $v/v_c \to 0$. The explicit dependence on the interaction strength and on the temperature, through a/λ_T, highlights the non-universal character of the EoS.

3.4.2 Compressibility

The isothermal compressibility, defined according to Eq. 1.55 as the relative variation of the density with respect to the pressure,

$$k = \left(\frac{1}{n}\right) \frac{\partial n}{\partial p}\bigg|_T,$$

was calculated for the experimental data through numerical differentiation of the density profile $n(x)$.

The resulting profile is shown in Fig. 3.9, as a function again of the reduced specific volume v/v_c. The compressibility k is normalized by the HF zero-temperature value

$$k_0 = \frac{1}{gn^2}, \tag{3.14}$$

for the density $n(x)$.

The curve predicted by HF theory is shown in black. Good agreement can be observed for small v/v_c, while at the critical point the theory predicts the presence of a narrow peak, which we did not observe experimentally. Several reasons could explain this disagreement:

- the mean field HF theory does not account correctly for the large fluctuations near the critical point, in a region of width $|\mu - \mu_c| \sim m^3 g^2 k_B^2 T_c^2/\hbar^6$, where μ_c is the chemical potential at the transition [33]. This corresponds to a temperature range $\Delta T/T \sim an^{1/3}$ around the transition point. For the density at the transition $n \sim n_c$ and the temperature of our cloud this is a relative temperature range of $\sim an_c^{1/3} = (\zeta_{3/2})^{1/3} a/\lambda_T \sim 5 \times 10^{-3}$ around T_c. The dependence on a/λ_T of the width of this critical region is again a signal of non universality.

- The HF curve is obtained from the theory for uniform matter, assuming the LDA to be valid everywhere, including the region near the boundary between the BEC and the thermal phase. A proper description of the behavior in this region requires instead corrections, that lead to a finite thickness $d = (a_x^4/(2R_x))^{1/3}$ of the boundary of the condensate, where R_x is the Thomas-Fermi radius along the x direction [182]. Since R_x scales with the number of atoms of the condensate, this can be regarded as a finite size effect. For our system we have $R_x \sim 100\,\mu\mathrm{m}$ and thus $d \sim 2\,\mu\mathrm{m}$, of the same order of magnitude as the resolution of the imaging system.

- Finally, we should consider the effect of the finite resolution of the imaging system ($\sim 2\,\mu\mathrm{m}$), which smears out the sharpest features in the density profile.

In Fig. 3.9 the data are compared also with a theoretical curve, obtained applying the HF model to the density profile convoluted with the resolution (grey dashed line). This curve already agrees much better with our data, and shows the strong effect of the finite imaging resolution in smearing out the narrow peak. Considering a two times worse resolution, one obtains the curve represented in brown, which well agrees with the experimental data. This may imply that the resolution has been underestimated. However, since the previous two effects need to be taken into account anyway, the remaining differences are more likely to be caused by the violation of LDA, as was concluded in the paper that we published on this work [5]. A recent theoretical work [183] also showed that in a non-uniform Bose gas the effect of the confining potential might completely wash out the divergence in the compressibility at the critical point. This corresponds to admitting the failure of LDA in a region with an extension at least equal to the width of the peak.

The compressibility peak was instead clearly observed in the unitary Fermi gas [157], where the width of the critical region, where the peak appears, is much larger, since the energy scale is fixed by the Fermi energy, reducing the impact of the effects described above.

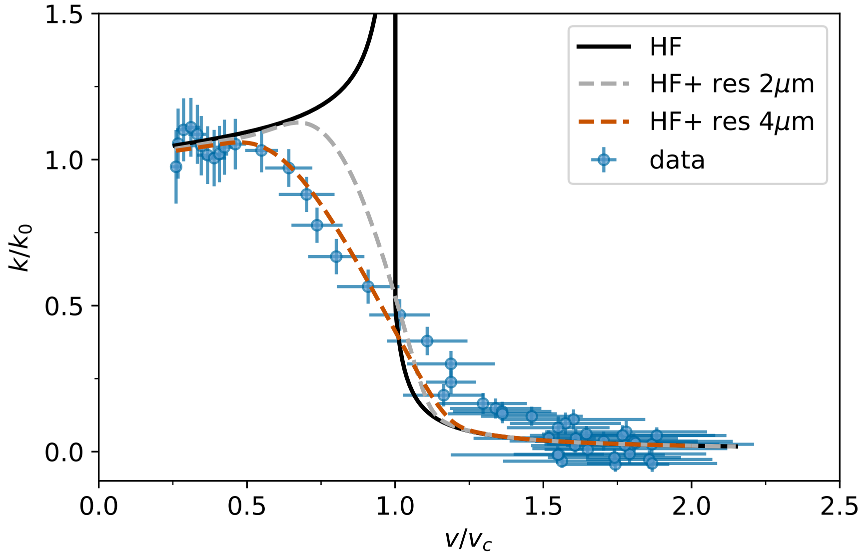

Figure 3.9: Compressibility k, normalized to the $T = 0$ value k_0, as a function of the reduced volume v/v_c. The solid black curve represents the HF prediction, while the dashed lines correspond to the HF prediction for a density profile convoluted with the resolution of the imaging system ($\sim 2\,\mu\mathrm{m}$, grey) and with a 2 times worse resolution ($4\,\mu\mathrm{m}$, brown).

3.4.3 Chemical potential

The study of the temperature dependence of the chemical potential has been one of the main goals of this project. Indeed a non-monotonic behavior, with a peak at the critical point, was predicted [158], but never observed before in a Bose gas. The chemical potential μ should have a non-monotonic behavior with T/T_c due to the combination of the following reasons:

- Below the critical point, $\mu(T)$ is expected to increase with T because of two main effects. For very low temperatures ($T < gn/k_B$), the thermal excitation of phonons

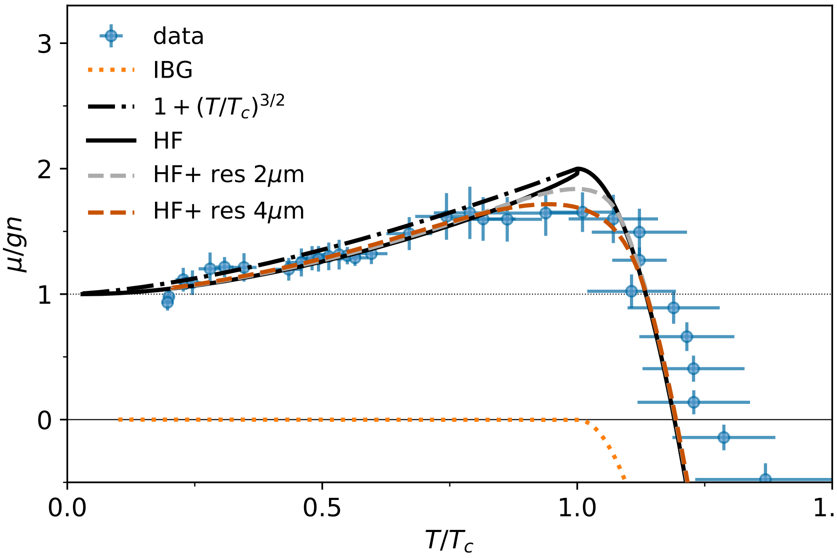

Figure 3.10: Chemical potential μ/gn as a function of the reduced temperature T/T_c. The dotted orange curve represent the IBG prediction, while the solid black curve the HF prediction. The dashed lines correspond to the HF prediction for a density profile convoluted with the resolution of the imaging system ($\sim 2\,\mu$m, grey) and with a 2 times worse resolution ($4\,\mu$m, brown), as in Fig. 3.9.

determines a dependence as $\mu \sim T^4$. For higher temperatures, but still below T_c, the chemical potential is predicted to increase as $\sim (T/T_c)^{3/2}$ because of exchange effects that characterize the thermal contribution to the energy of the system [29].

- above T_c the chemical potential is expected to decrease, reaching, for $T \gg T_c$, the behavior $\sim k_B T \ln(n\lambda_T^3)$, typical of a classical gas.

Since μ/gn is expected to increase for $T < T_c$ and decrease for $T > T_c$, it must have a maximum in between. The HF model predicts this to occur at the transition point, where the exchange effects are maximized being $n = n_T$, with μ/gn reaching the value of 2. The peak in the chemical potential, rather than being peculiar to Bose-Einstein condensates only, is a property of neutral superfluids in general. It was indeed observed already in the unitary Fermi superfluid gas [157] and in the thermodynamic behavior of liquid ^{4}He.

In our experiment we obtained a first observation of the non-monotonic behavior of μ also in a Bose gas. Within the LDA, the chemical potential μ is directly known from the external potential V_{ext} up to the constant μ_0. To determine μ_0, we fit the density to the HF profile obtained at $T = 280\,$nK, finding $\mu_0/k_B = 66.7(2)\,$nK. The experimental profile for the reduced chemical potential μ/gn is shown as a function of T/T_c in Fig. 3.10 (blue dots), clearly revealing a peak around T_c. The relative temperature range across the transition $0.2 \leq T/T_c \leq 1.5$, shown on the x axis in Fig. 3.10, corresponds to a spatial displacement along the x axis from the center of the trapped sample in the range $10\,\mu\text{m} \leq x \leq 140\,\mu\text{m}$, as shown in Fig. 3.7.

Similarly to what was observed for the compressibility measurement of Fig. 3.9, also in this case a discrepancy between the experimental data and the theoretical predictions can be noticed near the critical point. The sharpest features predicted by the theory get indeed smeared out by the effect of the finite resolution, besides being affected by the other limitations discussed in Sec. 3.4.2. The discrepancy is, however, smaller than in Fig. 3.9, and the presence of the peak in the chemical potential can be clearly observed.

The gray dashed line in Fig. 3.10 shows the behavior predicted by the HF model for a density profile convoluted with the imaging resolution of 2 µm.

In Fig. 3.10 we also plot the behavior for the IBG (orange dotted line), where the chemical potential is zero for any $T < T_c$ (see Sec. 1.1.4), as well as the universal behavior $\mu/gn = 1 + (T/T_c)^{3/2}$ (dash-dotted black line). The latter corresponds to the lowest order approximation of the HF chemical potential μ in terms of the interaction strength g and can be obtained by using the IBG expression for the thermal fraction n_T. It is worth noticing that the universal curve differs from the HF one only in the details of the shape for $T < T_c$, but both curves show a clear non-monotonic behavior and are in good agreement with the data.

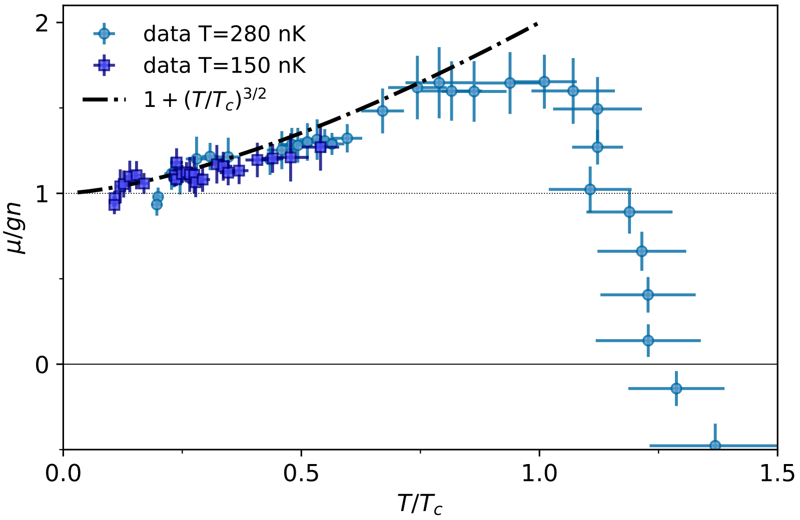

Figure 3.11: Chemical potential μ/gn as a function of the reduced temperature T/T_c, comparison between the measurements performed on samples at two different temperature (T=280 nK light blue circles, T=150 nK dark blue squares).

We also took measurements at a lower temperature ($T = 150\,\mathrm{nK}$), where a fit to the HF model is not needed for the estimation of μ_0, since one can assume the zero-temperature limit $\mu_0 \simeq gn(0)$, given the strong suppression at low T of the thermal fraction at the center of the trap. The central density $n(0)$ was obtained from a fit to a Thomas-Fermi profile in the central region ($x < 60\,\mu\mathrm{m}$, corresponding to $T/T_c < 0.15$), which yields $\mu_0 = 69.0(4)\,\mathrm{nK}$. We checked *a posteriori*, using HF theory, that the local thermal fraction in this whole central region is < 0.02. The reduced chemical potential profile μ/gn corresponding to this lower temperature measurement is shown in Fig. 3.11 (dark blue squares), where it is compared with the higher temperature result discussed before (light blue circles). We observe again that μ/gn monotonically increases for $T < T_c$, in agreement with the measurement at higher temperature and with the prediction of the HF model. This behavior clearly indicates the contribution of exchange effects to the energy of the system, that are captured even using a zero-temperature model to estimate μ_0.

The two different temperatures $T = 150\,\mathrm{nK}$ and $T = 280\,\mathrm{nK}$ of the samples correspond to different values of the parameter a/λ_T, 3×10^{-3} and 4×10^{-3} respectively. In principle we should thus notice a non-universal difference in the shape of the μ/gn curves for the two datasets. This difference is however not discernible from our measurements: in both cases the experimental data well agree, within the errorbars, with the universal curve $1 + (T/T_c)^{3/2}$ (dot-dashed line in Fig. 3.11). To find quantitative evidence of deviations from the universal curve, more precise and systematic measurements of μ/gn as a function of temperature would be needed. Such measurements could also provide evidence for beyond mean field effects [184].

3.4.4 Grand canonical EOS

The above results can be discussed also in the grand canonical framework, finding the EOS of the pressure p in terms of the grand canonical variable given by the chemical potential μ instead of the canonical variable, i.e. the density n.

In figure 3.12 we show, for the dataset at $T = 280\,\text{nK}$, the reduced pressure p/p_c as a function of the inverse fugacity ζ, which is related to the chemical potential μ and the temperature T by the expression:

$$\zeta = \exp\left(-\frac{\mu}{k_B T}\right). \tag{3.15}$$

Outside the degenerate region, for $\zeta > 1$, the reduced pressure has the behavior of the

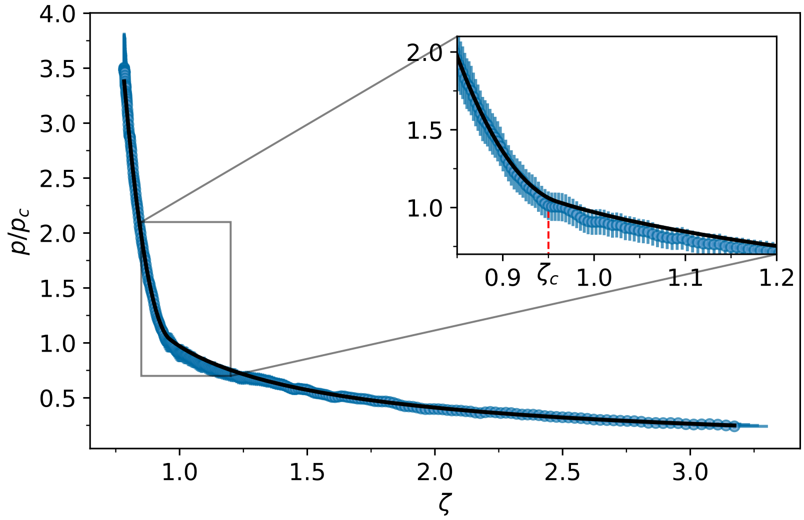

Figure 3.12: Grand canonical equation of state: p/pc as a function of the inverse fugacity ζ.

non-interacting Bose gas $\sim g_{5/2}(\zeta)/\zeta_{5/2}$, which in the limit of $\zeta \gg 1$ eventually approaches the classical gas law $\sim \zeta^{-1}$. On the other side, for smaller ζ, the slope of the pressure suddenly increases at the transition point for condensation ζ_c, as highlighted in the inset of Fig. 3.12. In the deeply degenerate regime, for $\zeta \to 0$, the effect of interactions becomes evident, causing the pressure to diverge as $(\lambda_T/a)\ln^2\zeta$. A similar measurement of the grand canonical EOS was reported already in Ref. [3], where the authors show the presence of a cusp in the pressure as a function of the inverse fugacity at the transition point, which they identified at $\zeta_c = 1.0(1)$, in agreement with the value of $\zeta_c = 1$ expected for the IBG, being in their case the interaction induced mean-field correction compatible with the experimental uncertainty.

From our measurements we find $\zeta_c = 0.95(1) < 1$, which highlights the presence of a shift in the transition point, compatible with the mean field shift caused by interactions. This value of the critical fugacity corresponds indeed to a chemical potential of $\mu_c = k_B \times 14(3)\,\mathrm{nK}$, which agrees with the mean-field shift $2gn_c \simeq k_B \times 12.2(5)\,\mathrm{nK}$, calculated using the critical density for the temperature of 280 nK, and also with the results for the chemical potential shown in Sec. 3.4.3.

3.5 Conclusions

The work presented in this chapter provides an important contribution to the study of the equilibrium thermodynamic properties of a 3D weakly interacting Bose gas [5]. The Equation of State of the uniform Bose gas, across the critical point, was obtained for the first time in its canonical formulation $p(v)$, at fixed temperature T and scattering length a. We also observed, for the first time in a Bose gas, the non-monotonic behavior across the phase transition of $\mu/(gn)$ as a function of the relative temperature T/T_c, which appears to be a consequence of Bose-Einstein condensation and a common feature in the thermodynamic behavior of neutral superfluids.

Our measurements well agree with the predictions of the mean-field Hartree-Fock model for the weakly interacting uniform Bose gas, when the effect of the finite resolution of the imaging system is taken into account.

The achievement of these results was possible thanks to the high-dynamic-range partial-transfer imaging and reconstruction technique that we developed to accurately measure the density profile of the trapped gas [4] and thanks to the upgrade of the imaging system described in Sec. 2.7.1.

Chapter 4

Study of out-of-equilibrium Bose gases

4.1 Introduction

In this chapter I present the results of an experimental investigation on the formation and growth dynamics of the BEC order parameter and its fluctuations, as a function of the rate at which the ultracold Bose gas is cooled across the BEC transition point. In particular, we focused on the study of the timescales associated to such dynamics, and were able to identify a universal power-law scaling. The results of this study were recently published in [27].

This chapter is structured as follows. In Sec. 4.2, I first present the experimental sequence and the procedures to extract the relevant observables for these measurements. Sec. 4.3 shows how the cooling rate and the initial number of atoms in the cold sample influence the growth dynamics. Sec. 4.4 presents a discussion on the dynamics of the phase fluctuations arising at the onset of condensation and on their subsequent decay as the system relaxes towards its final equilibrium state.

4.2 Experimental procedure

This set of experiments is based on the cooling, by means of RF driven evaporation, of a cold cloud of atoms, initially at equilibrium at a temperature above the critical point for Bose-Einstein condensation. During the cooling process, the transition point is crossed at a tunable cooling rate, and the subsequent evolution of the system is studied.

We exploit the cooling techniques described in Chap. 2: after the initial laser-cooling stage in the DS-MOT and later in the GM, the pre-cooled gas of sodium atoms is transferred in the magnetic trap, where RF evaporation takes place, driven by a radio-frequency field that transfers the $|F, m_F\rangle = |1, -1\rangle$ trapped atoms to the non trapped $|1, 0\rangle$ state (see Sec. 2.6.3). A first evaporative cooling stage, in common with the experimental sequence used for the EoS measurements (Chap. 3), takes place by sweeping down the RF frequency in two consecutive exponential ramps, as shown in Fig. 2.10.

During the cooling procedure, the sample is confined in the magnetic trap described in Sec. 2.3, with the final cooling stage taking place in the configuration with a 100 A current in the magnetic coils, as shown in Fig. 2.10. The axial and radial measured trapping frequencies, in the final trap configuration, are $\omega_x = 12.30(5)\,\mathrm{Hz}$ and $\omega_\rho = 138(1)\,\mathrm{Hz}$, respectively. The bias field B_0 is 1.53 G, corresponding to a trap bottom frequency of $\nu_b = 1.076\,\mathrm{MHz}$.

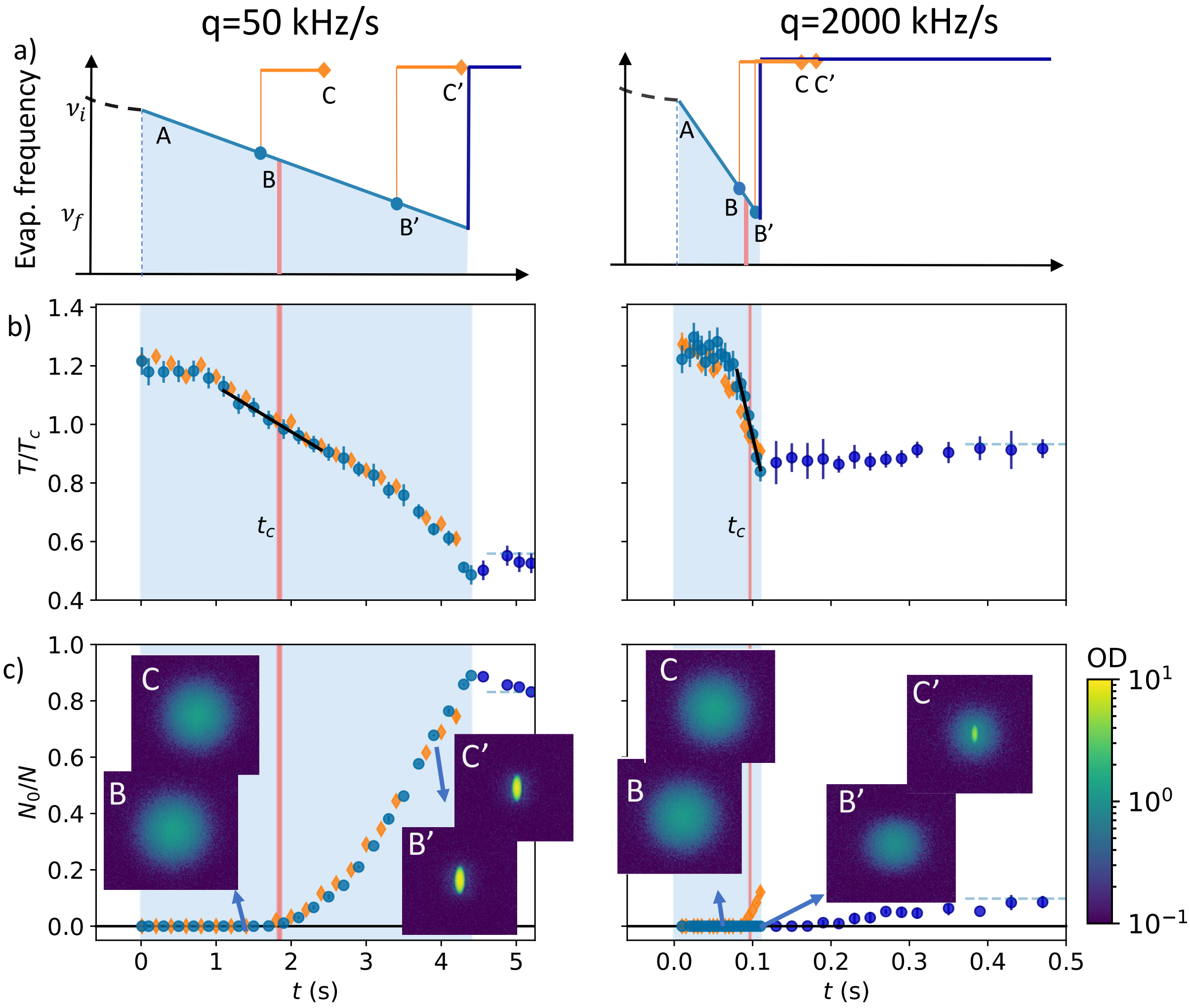

Figure 4.1: Exploring the gas parameters during the evaporation ramp for a low (left column) and high (right) evaporation rate. (a) Variation of the RF evaporation frequency ν in time; the evaporation rate is defined as $q = d\nu/dt$. (b) Temperature and (c) condensed fraction, measured by interrupting the ramp at different times t and either imaging the cloud immediately (light and dark blue circles) or keeping the gas in trap for a waiting time of 1 s for equilibration (orange diamonds). Temperature is extracted from a Bose distribution fit to the tails of the atomic distribution measured after a time of flight $t_{\mathrm{tof}} = 50\,\mathrm{ms}$ and is normalized to the transition temperature T_c. The red vertical line represents the time t_c at which T_c is experimentally crossed in the instantaneous measurements. The horizontal blue dashed line in (b) corresponds to the final temperature after equilibration, while the horizontal dashed line in (c) marks the final condensate fraction. The insets show absorption images taken in points B, C (for $t < t_c$) and B', C' (at $t > t_c$). The light-blue shaded area marks the duration of the ramp.

At the end of the first two exponential evaporation ramps [point A in Fig. 4.1], the RF frequency is $\nu_2 \simeq 1.33\,\mathrm{MHz}$, corresponding to a trap depth of about $h(\nu_2 - \nu_b) \sim k_B \times 12\,\mu\mathrm{K}$, and our sample is a cold atomic cloud in equilibrium at a temperature of the order of 1.3 T_c. Two sets of atomic ensembles have been studied, characterized by a different number of atoms, measured in point A:

- one set of ensembles is characterized by a high number of atoms $N_{\mathrm{high}} = 3.6(3) \times 10^7$ and initial temperature $T_{\mathrm{high}} = 1.14(3)\,\mu\mathrm{K} = 1.28(7) T_c$

- the other set has a lower initial atom number $N_{\text{low}} = 1.7(9) \times 10^7$ and temperature $T_{\text{low}} = 0.92(4)\,\mu\text{K} = 1.32(5)T_c$. For the low atom number ensembles, in order to keep the same initial relative temperature, and comparable conditions during the linear ramp, the latter starts at $\nu_i \equiv \nu_2 = 1.27\,\text{MHz}$ instead of $1.33\,\text{MHz}$.

At this point, a final evaporative stage, of interest for this work, takes place, where the RF frequency is further lowered at a tunable rate $q = d\nu/dt$ by means of a linear ramp, starting from an initial frequency $\nu_i \equiv \nu_2$, equal to the final frequency of the previous stage, and ending at a frequency $\nu_f = 1.11\,\text{MHz}$, which is reached at a time t_f, corresponding to the duration of the linear ramp (shaded region in Fig. 4.1). More details on the choice of the final frequency are provided below in Sec. 4.2.1. During this last evaporation ramp, the critical temperature for BEC onset is crossed. We change the rate q and study how this influences the dynamics of the BEC formation and growth.

The atomic cloud is imaged by means of resonant absorption imaging, using the `cam_y1` camera, after a time of flight $t_{\text{TOF}} = 50\,\text{ms}$ from the switch-off of the magnetic trap (see Sec. 2.8). Two different measurement schemes are interleaved for each quench rate:

- *Instantaneous* images capture the status of the system at different times t *during* the linear cooling ramp. They are taken by interrupting the evaporation ramp and immediately releasing the atoms [points B, B' in panel (a) of Fig. 4.1].
- *Equilibrium* images probe the system after it has reached its equilibrium condition. They are taken interrupting the evaporation at the same time t, but keeping the atom cloud in trap for an additional hold time of 1 s before releasing and imaging (points C, C').

During the hold time, RF shielding is used (see Sec. 2.6.3): we set the evaporation frequency to $\nu_{\text{hold}} = \nu_i + 400\,\text{kHz}$, corresponding to a trap depth of $\sim k_B \times 31\,\mu\text{K}$, to ensure thermalization without further loss of atoms. Using the shield, the number of atoms and the temperature after equilibration remain $\sim$ constant on timescales much longer than 10 s.

- *Instantaneous* images are also taken *after* the end of the ramp, for times $t > t_f$. In this case the evaporation frequency is raised to ν_{hold} after the ramp has ended at the final frequency ν_f, and the atom cloud is kept in trap to probe the post-quench relaxation dynamics.

For all images, we fit the OD of the atomic cloud with a Bose function (see Sec. 2.8), to measure the width and amplitude of the distribution, from which we extract the number of atoms in the thermal component N_{th}. In order to obtain an accurate measurement, not influenced by the eventual presence of a condensate in the center of the cloud, the Bose fit is performed only on the outer part of the distribution, corresponding to the area of the image outside a central ellipse of fixed dimensions, chosen to contain the whole BEC in the case of maximum number of condensed atoms. Subtracting the fitted Bose function from the data, we obtain an image of the condensate alone, that we integrate to obtain the number of atoms N_0 in the BEC. We do not perform a fit of the BEC to a Thomas-Fermi profile (see again Sec. 2.8), since this function properly describes the condensate profile only when the system is in its ground state and not in the presence of fluctuations. The Thomas-Fermi approximation, moreover, is valid only when the number of atoms in the

BEC is large enough. The total number of atoms N is then given by the sum of N_{th} and N_0.

As explained in Sec. 2.6.3, the evaporation process removes the most energetic atoms from the distribution and leads to a decrease in the total atom number. This causes the gas to be no longer in thermal equilibrium at the instantaneous times during the evaporation ramp, especially for the fastest ramps. This means that the temperature of the gas is instantaneously not well-defined in a thermodynamic sense. We introduce an effective temperature T, extracted from the fitted width of the thermal cloud in the direction z, according to Eq. 2.33:

$$T = \frac{m\omega_z^2\sigma_z^2}{(1+\omega_z^2 t_{\mathrm{TOF}}^2)k_B}, \tag{4.1}$$

where σ_z is the width of the fitted Bose distribution (Eq. 2.27) along the radial direction. This choice is motivated by the fact that $\omega_z \gg \omega_x$, which makes the distribution along z closer to the momentum distribution for $t = t_{\mathrm{TOF}}$ and therefore more reliable than that along x to estimate the temperature. The duration of the time of flight t_{TOF} was chosen in order to satisfy the condition $\omega_z t_{\mathrm{TOF}} \gg 1$.

Figure 4.1 (b) shows, for two different ramp rates q, the measured temperature T in units of the critical temperature for condensation T_c, estimated at each time t for the instantaneous atom number N measured at such time. We compute T_c as $T_c = T_c^0 + \delta T_c$, where T_c^0 is the critical temperature for an ideal Bose gas in our harmonic trap (Eq. 1.12) and δT_c is a correction taking the shift caused by the effect of interactions (Eq. 1.61) into account. For our experimental parameters, such correction is of the order of $|\delta T_c|/T_c^0 \sim 3\%$. We instead neglect finite-size corrections to the critical temperature (Eq. 1.62), since they are about one order of magnitude smaller.

In Fig. 4.1 (b-c), light blue circles correspond to instantaneous images taken before the end of the linear evaporation ramp, while orange diamonds are the corresponding equilibrium images. Dark blue circles are instantaneous pictures taken after the end of the ramp. Each point corresponds to the average of up to 10 repetitions of the same experimental shot, and error bars represent one standard deviation. The light red vertical line marks the critical time t_c, defined as the time at which $T/T_c = 1$, and obtained by means of a linear fit to the data in the region around the critical point (solid black line). The same linear fit yields also the characteristic quench time, defined as:

$$\tau_Q = \frac{T_c}{|(dT/dt)_{t_c}|}. \tag{4.2}$$

This allows for a direct comparison to theoretical models assuming a linear variation of the temperature across the transition [23].

Figure 4.1 (c) shows the evolution of the condensate fraction N_0/N, again comparing the instantaneous and equilibrium configurations. The insets show examples of TOF images taken before and after the transition point. If the ramp is sufficiently slow (left panels of Fig. 4.1), we observe that the condensate forms during the evaporation ramp. For a fast ramp, instead, no condensate fraction is present at the end of the ramp, but an order parameter emerges afterwards, during the post-quench relaxation, on a timescale independent of the evaporation rate q, but rather intrinsic of the system, as will be shown in Sec. 4.3.

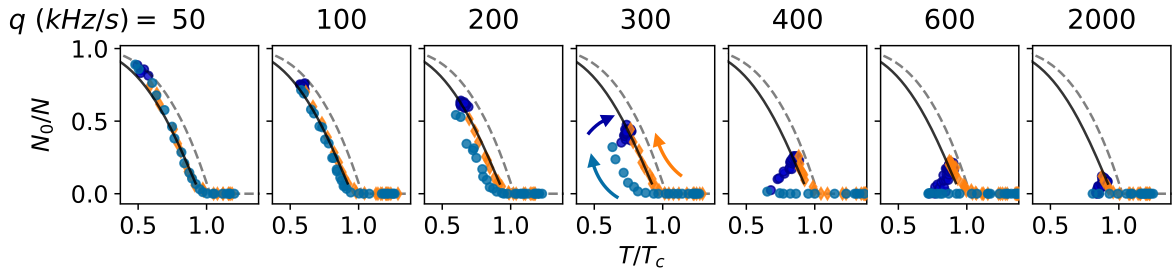

Figure 4.2: Evolution of the condensate fraction N_0/N as a function of the relative temperature T/T_c. Higher evaporation rates induce strong out-of-equilibrium dynamics, as can be seen comparing the instantaneous measurements (light and dark blue circles) with the equilibrium points (orange diamonds). The arrows shown in the $q = 300\,\mathrm{kHz/s}$ panel indicate the direction of the evolution. The dashed gray and solid black curves represent the theoretical predictions for an ideal and an interacting trapped Bose gas, respectively.

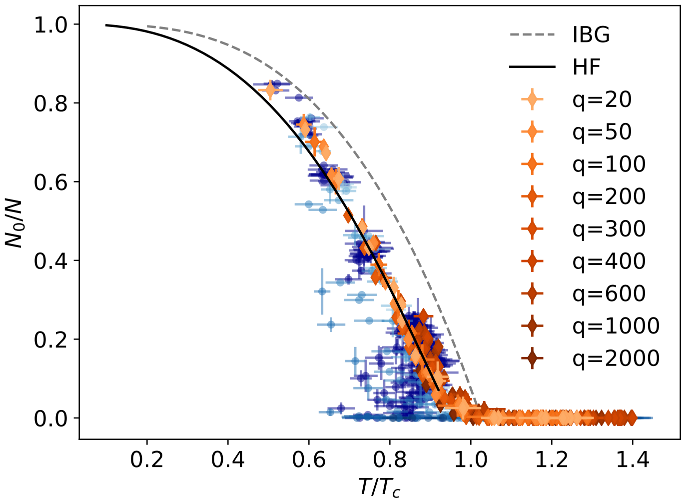

Figure 4.3: For all evaporation rates, the equilibrium data points (orange to red diamonds) for the condensate fraction as a function of the relative temperature follow the same curve for any q (the values reported in the legend are in kHz/s). This behavior is well described by the HF prediction for the interacting trapped Bose gas, represented by the solid black curve (see Eq. 1.63). The theoretical curve for the ideal Bose gas (IBG) is also shown (dashed gray). Light and dark blue dots show the system's status during and after the ramp, respectively, as in Fig. 4.2. These instantaneous points, for high evaporation rates, get far from the equilibrium curve.

The dynamical evolution of the gas across the transition can be observed, for different quench rates q, in Fig. 4.2, where the condensate fraction N_0/N is shown as a function of T/T_c. This plot gives a clear view of the out-of-equilibrium evolution related to the cooling process, by comparing the instantaneous data points (blue and dark blue) to the equilibrium ones (orange). The arrows mark the direction of the evolution in time for the two data sets.

For the lowest evaporation rates the gas cools down almost adiabatically, as pointed out by the overlap of the instantaneous and equilibrium curves for $q = 50\,\mathrm{kHz/s}$.

For higher evaporation rates, instead, the gas is driven in an increasingly out-of-equilibrium state, as shown for instance in the $q = 300\,\mathrm{kHz/s}$ panel. We observe that the instantaneous state of the gas strongly diverges from the equilibrium one while driven by the evaporation (the light blue points get further and further away from the orange curve), and it relaxes towards the final equilibrium state after the end of the ramp (the dark blue points gradually approach the orange ones, on which they finally collapse). The equilibrium points (orange) for the different values of q actually collapse on the same curve, as shown in Fig. 4.3. Making a quite long-ranged analogy, one could think of this curve as an analogue of the Hertzsprung-Russel diagram, describing stellar evolution [185], for the evolution of a condensate, discriminating between equilibrium and out-of-equilibrium conditions in the BEC growth process. For comparison, we also show the theoretical prediction given by Eq. 1.13 for the ideal Bose gas (gray dashed line) and the prediction given by the HF model Eq. 1.63 for the interacting Bose gas (solid black line)[1]. We observe a good agreement between the HF theoretical curve and the equilibrium data points, confirming earlier experimental observations for condensates at equilibrium [15, 138]. The agreement between the measured equilibrium condensate fraction and the HF prediction can also be used as a cross-check or as a stand-alone method [186] for the calibration of the absorption imaging parameters α and χ_{sat} that enter in the calculation of the OD, determining the number of atoms.

From these measurements, we find that the system reaches a stationary state, where the relative temperature and condensate fraction remain constant and most of the excitations have relaxed, already after $t \gtrsim 500\,\mathrm{ms}$, even for the highest evaporation rates (q up to $4000\,\mathrm{kHz/s}$). This means that, *a posteriori*, we can consider the images taken after 1 s waiting time as reliable equilibrium points.

4.2.1 Choice of final frequency for the linear ramps

The final frequency ν_f is the same for all measurements and has been chosen in order to lie enough above the trap bottom value to avoid the removal of atoms from the BEC. This is checked by performing a slow evaporation, ramping the frequency of the second exponential evaporation ramp down to different values $\nu_f \geq \nu_b$. The number of atoms in the condensate is measured as a function of the final evaporation frequency (see above for the measurement procedure), observing the behavior shown in Fig. 4.4 (a). Before these measurements, we tune the compensation magnetic fields in order to keep a constant bottom frequency $\nu_b = 1.076\,\mathrm{MHz}$ (see paragraph 2.6.4). Performing a slow evaporation until increasingly lower frequencies, a growth of the number of atoms in the condensate can be observed, until a $\sim 100\%$ condensate fraction is reached. Soon after, the number of atoms in the BEC rapidly drops, when the evaporation frequency approaches ν_b.

As a final frequency, we select the value $\nu_f = 1.11\,\mathrm{kHz}$ (black dashed line), for which the condensate fraction has almost completely reached its maximum. This final frequency is selected to stay well above the frequency where the RF field starts removing atoms from

---

[1] The approximation in which this curve is obtained holds only for temperatures enough below T_c, where a high number of atoms is present in the condensate, but not in the close vicinity of the critical point. For this reason the curve was plotted only for $T \leq 0.92 T_c$.

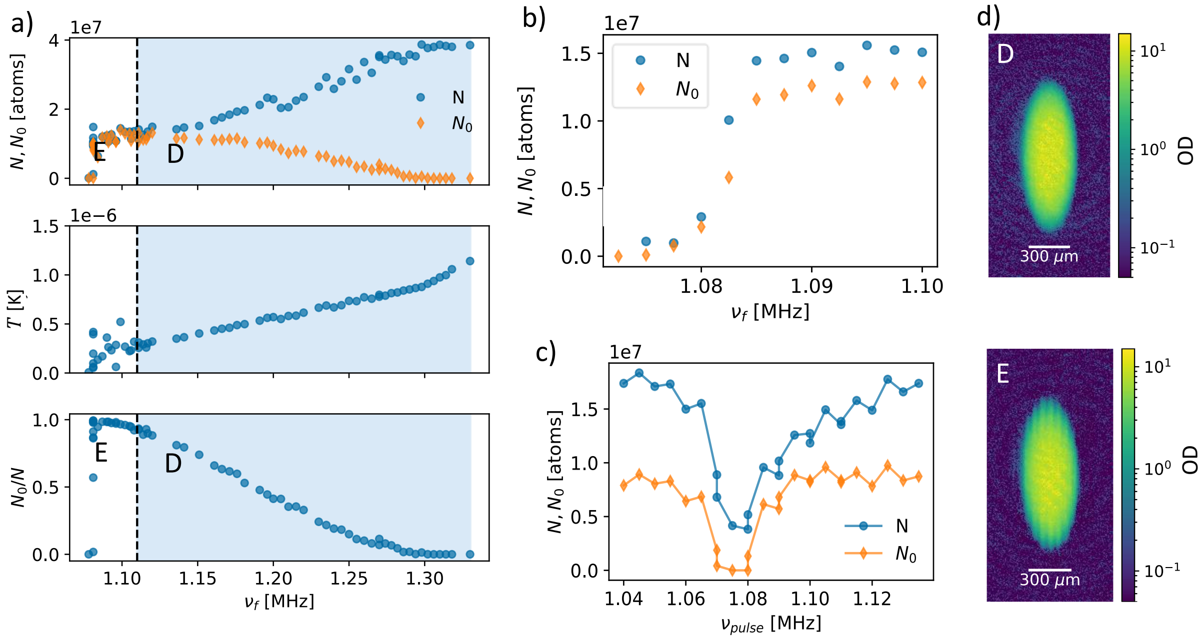

Figure 4.4: Measurements to define the best final frequency for the evaporation ramp. (a) As a function of the final frequency ν_f, reached by means of the continuation of the second exponential RF ramp, we measure: (top) the total number of atoms N (blue dots) and the number of atoms in the condensate N_0 (orange diamonds); (center) the effective temperature T; (bottom) the condensate fraction N_0/N. (Image E) For frequencies close to the bottom, corresponding to point E in panel (a), regular fringes are observed in the density profile after a 50 ms TOF expansion. (Image D) Such fringes are not present if the evaporation is interrupted before, well above the bottom frequency (point A). (b) Similar measurement performed with a $q = 50$ kHz/s linear RF ramp. For frequencies below 1.09 MHz we observe an abrupt decrease of the total (blue dots) and condensate (orange diamonds) atom number. (c) After producing a partially condensed equilibrium cloud, we turn on the evaporation RF field for a 5 ms pulse, with the same amplitude as used for the evaporation. We scan the frequency ν_{pulse} and measure again the number of atoms. The pulse depletes the BEC completely if the frequency is in the interval $1.06\,\text{MHz} \geq \nu_{pulse} \geq 1.09\,\text{MHz}$, centered on the bottom frequency. (d) Two images showing the OD of the atomic cloud (cropped to area containing the BEC), corresponding to points D ($\nu_f = 1.085\,\text{MHz}$) and E ($\nu_f = 1.13\,\text{MHz}$) indicated in (a). Image E shows the presence of regular fringe patterns, which do not appear in D. These results made us choose as final frequency for the main measurements $\nu_f = 1.11\,\text{MHz}$ [vertical black dashed line in (a)].

the condensate, since this causes collective excitations that result in the appearance of regular fringe patterns in the BEC density profile observed after a TOF expansion (image E of Fig. 4.4), that are not present if the final frequency remains higher (image D). The appearance of such fringes seems not to depend on the shape of the evaporation ramp, since it occurs also if the last part of the evaporation towards the bottom frequency is made by a slow linear evaporation ramp (e.g. with $q = 50$ kHz/s), instead of exponential. Panel (b) of Fig. 4.4 shows that, if such a linear evaporation ramp is continued until final frequencies $\nu_f < 1.09$ MHz, the number of atoms in the BEC (and in the whole system) gets depleted. For such low frequencies we again see the appearance of the same fringes.

To check the value of the bottom frequency ν_b and of the lowest final frequency ν_f where we should stop the evaporation to avoid the above effect, we also perform another experiment. We first obtain an equilibrium $\sim 50\%$ condensed atomic cloud by means of a slow exponential evaporation until $\nu_f = 1.2$ MHz, followed by a sufficiently long equilibration time without further evaporation. We then turn on the evaporation RF field, with the same amplitude used in the evaporation, for a 5 ms pulse at a frequency ν_{pulse}, which we scan in an interval around ν_b. We record the final number of atoms in the whole cloud (N) and in the BEC (N_0), measured as before from TOF images. As shown in panel (c), in agreement with the other two measurements, of panels (a)-(b), we see that the number of atoms significantly decreases for $1.06\,\mathrm{MHz} \geq \nu_{pulse} \geq 1.09\,\mathrm{MHz}$, with a minimum around the bottom frequency. In this interval we again notice the presence of the same fringes in the OD of the TOF images, which confirms that they are caused by collective excitations due to the forced removal of atoms from the BEC. All these results lead us to a choice of a final frequency $\nu_f = 1.11\,\mathrm{MHz}$, which is kept the same for all evaporation ramps to make an easier comparison between the different datasets.

4.3 Growth of the order parameter

In this section we give a closer look at the dynamical formation of the condensate order parameter, following the evaporative cooling.

In all experiments, while the critical point t_c always lies within the linear evaporation ramp, the time evolution of the condensate depends on the evaporation rate. Two distinct regimes can be observed, that we identify as high and low evaporation rates. The two regimes are distinguished by the fact that, for the chosen frequency-span of the evaporation ramp:

- for *low* evaporation rates (slow ramps) condensation is observed already in the instantaneous images taken during the ramp, as shown by the absorption images in the insets of Fig. 4.1c);
- for *high* evaporation rates, instead, no BEC is observed in the instantaneous images during the evaporation process, but the emergence of the condensate order parameter occurs instead after the end of the linear ramp, driven by thermalization at constant atom number.

The distinction between high and low evaporation rates is not determined only by the absolute value of the rate q, but also by the initial number of atoms in the system and on the choice of the initial and final RF frequency. To explore the dependence on the atomic density, for both evaporation rate regimes, the same measurements have been performed on two sets of atomic ensembles, having different atom number (see above) but the same initial relative temperature $T_i = 1.3T_c$ at the beginning of the linear ramp [point A of the experimental sequence, see Fig. 4.1 (a)].

4.3.1 High evaporation rate: post-quench dynamics

We first consider the formation and growth of the BEC order parameter for high evaporation rates.

Figure 4.5 (a) shows the growth of the BEC fraction in samples with N_{high}, for evaporation rates $q \geq 400\,\mathrm{kHz/s}$. For these ramps, although the critical temperature is crossed at a time t_c during the ramp, the order parameter forms only after the end of the ramp, after a finite *latency time* Δt past t_c (in literature also referred to as *initiation time* [14]). As can be observed in Fig. 4.5 (a-b), this latency time does not depend on q; its average value $\Delta t = 85(7)\,\mathrm{ms}$ is indicated by the gray area in (b). After the BEC onset, the condensate fraction grows and slowly reaches its final maximum value $(N_0/N)_f$, on a time-scale that

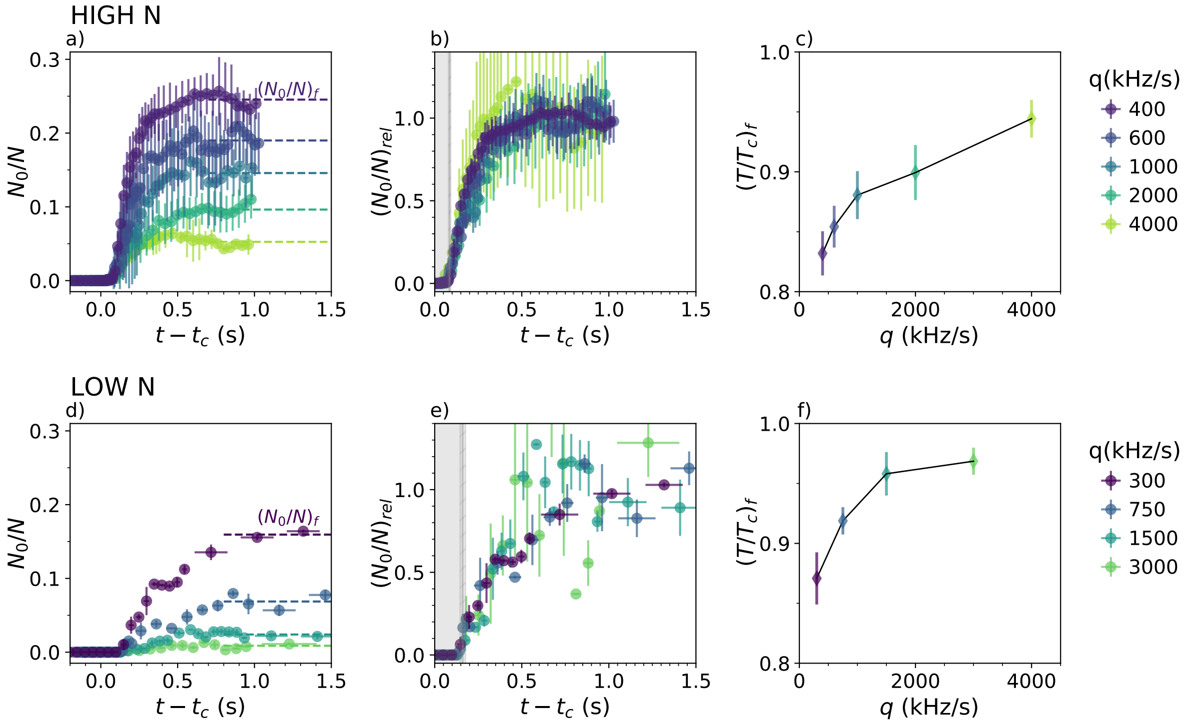

Figure 4.5: Post-quench growth dynamics of the BEC order parameter for high evaporation rates. (a) Condensate fraction as a function of time for atom number N_{high}, for different values of q. The time axes are shifted by t_c, defined in the text. The dashed lines indicate the equilibrium condensed fraction for each evaporation rate, which results to be lower for increasing evaporation rates. (b) Same as (a), but with the vertical axis normalized to the final condensed fraction that is reached for each evaporation rate q. The gray area highlights the latency time Δt (see text). (c) Final relative temperature T/T_c for the various rates q. T/T_c is higher for higher evaporation rates. [(d)-(f)] Equivalent results as [(a)-(c)] but for atomic samples with a lower initial number of atoms N_{low}.

again appears to be independent of q. This becomes more evident when rescaling, for each value of q, the condensate fraction of Fig. 4.5 (a) by its final value $(N_0/N)_f$, obtained by averaging the data for $(t-t_c) > 500$ ms, and marked by the dashed lines in (a). The rescaled curves, shown in (b), all overlap within the errorbars, indicating that also the growth dynamics of the order parameter is independent on q. For these reasons, these ramps are effectively a *quasi-instantaneous quench*.

The final temperature $(T/T_c)_f$ reached after the post-quench relaxation, as shown in Fig. 4.5 (c), increases with q, while the condensate fraction $(N_0/N)_f$ [see Fig. 4.5 (a)] decreases, meaning that the evaporation becomes less and less efficient for increasing quench rates. Indeed the maximum rate $q = 4000$ kHz/s was selected in order to still obtain a condensate after the post-quench equilibration, even if with a very low final BEC fraction (around 1%, close to the detection limit). Especially in these cases, our choice of measuring the number of atoms by integrating the residuals of the fitted Bose distribution appears to be much more reliable than performing a Thomas-Fermi fit on the condensed part. Our procedure, indeed, is not influenced by the choice of any fitting function for the condensate profile, and has a detection limit determined only by the average noise, allowing for a determination of the onset of condensation already from images with a few thousand atoms in the condensate. Such BEC images do not fit well to a Thomas-Fermi profile, being far from the high-atom number condition at the basis of the Thomas-Fermi approximation and in a strongly out-of-equilibrium condition (see Sec. 4.4).

Analogous results, shown in Figs. 4.5 (d)-(f), are obtained for the dataset with N_{low}, where the density of particles in the cloud is lower. Qualitatively, the behavior is the same as for the high atom number case, but, quantitatively, the delay in the onset of the order parameter becomes longer: $\Delta t = 161(16)\,\text{ms}$. Also the growth of the order parameter for less dense clouds occurs on longer timescales, with the final equilibrium BEC fraction being reached after $(t - t_c) \geq 750\,\text{ms}$. Both behaviors well agree with a model where the latency time and BEC growth timescale depend on the re-equilibration processes at constant atom number in the isolated post-quench system, which essentially depend on two-body atomic collisions. In this framework, the larger timescales observed for the ensembles with lower atom number well agree with the collisional time being larger in the case of lower atomic density. We estimate the classical collisional time according to [75], as

$$\tau_{\text{coll}} = (\bar{n}\sigma v)^{-1}, \tag{4.3}$$

where $\bar{n} = \int n^2(r)dr / \int n(r)dr$ is the average density of the thermal cloud, computed at the transition time t_c, $\sigma = 8\pi a^2$ is the s-wave scattering cross-section and $v = 4\sqrt{k_B T/(\pi m)}$ is the average velocity. This yields a collisional time of $\tau_{\text{coll}} \sim 18\,\text{ms}$ for the N_{high} dataset and $\tau_{\text{coll}} \sim 32\,\text{ms}$ for N_{low}, suggesting that the delay in the onset of condensation also obeys a universal behavior, resulting in $\Delta t \sim 5\tau_{\text{coll}}$. These observations are in good agreement with early works on the BEC formation after a sudden quench [13, 14], which clarified the role of interactions in the condensation process, leading to the development of a complete quantum kinetic theory [187], and indicating the existence of a latency time in the condensation process.

4.3.2 Low evaporation rate: growth dynamics during the ramp

In Sec. 4.3.1 we discussed the formation and growth of the BEC order parameter taking place after a fast evaporation ramp that can be considered as an almost instantaneous quench. In this section, instead, we consider lower evaporation rates, with $q \leq 400\,\text{kHz/s}$ in the case of N_{high} and $q \leq 200\,\text{kHz/s}$ for N_{low}. This makes the dynamics conceptually different, since the formation of the condensate occurs during the RF-driven evaporation, which implies that both the atom number and temperature are decreasing during the process, rather than staying constant as in the post-quench dynamics discussed before.

Figure 4.6 shows the evolution of the condensate fraction as a function again of $(t - t_c)$ for the case of slow ramps. The data for different ramp rates q fit well to a smooth step function, as shown in Fig. 4.6 (a). We fit the BEC growth data to the error function:

$$\frac{N_0}{N}(t) = \frac{1}{2}\left[1 + \text{erf}\left(\frac{t - t_c - t_{50\%}}{\sqrt{2}\tau_1}\right)\right], \tag{4.4}$$

which is centered at $t_{50\%}$ (where the condensate fraction reaches 50%) and is characterized by a growth time constant τ_1. The fit is performed only on the data points corresponding to $N_0/N < 0.5$ [solid lines in Fig. 4.6 (a)], since we focus on the initial part of the condensate formation process, and not on the final saturation of the condensate fraction. As expected, the condensate growth is slower for slower evaporation ramps, corresponding to smaller values of q (higher τ_Q). In Fig. 4.6 (b) the same data are shown as a function

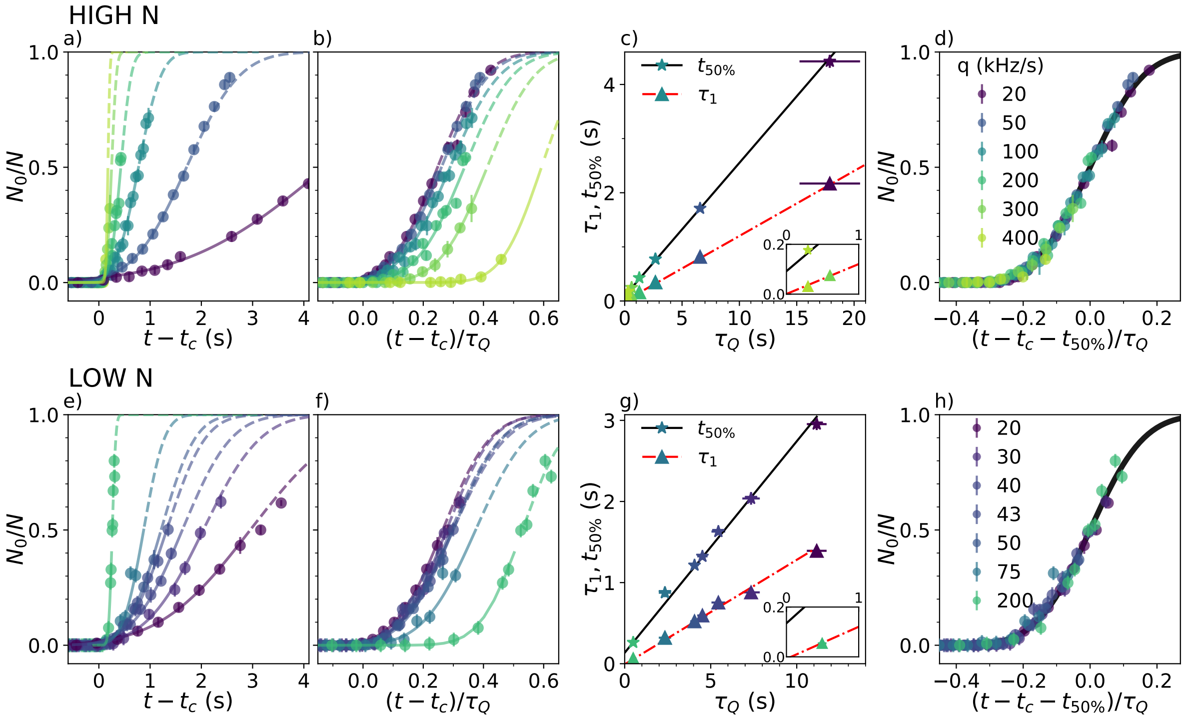

Figure 4.6: Growth of the BEC order parameter during cooling ramps with low evaporation rate. The condensate fraction is shown for different evaporation rates on gases with initial atom number N_{high}, as a function of $(t - t_c)$ (a) or $(t - t_c)/\tau_Q$ (b). The curves correspond to the fitted error functions, defined in the main text (solid lines represent the fitting functions in the interval where the fit is performed, while dashed lines outside). Panel (c) shows the dependence on the characteristic ramp time τ_Q of the sigmoidal fit parameters τ_1 (triangles) and $t_{50\%}$ (stars). The lines are linear fits of $\tau_1(\tau_Q$ (black solid) and $t_{50\%}(\tau_Q)$ (red dot-dashed). The inset shows a zoom of the region close to the origin, highlighting the presence of a finite offset for $t_{50\%}$, while $\tau_1 \to 0$ when $\tau_Q \to 0$. Panel (d) shows that all growth curves, when shifted by the $t_{50\%}$ parameter obtained from the fit and rescaled by the time τ_Q of each ramp, overlap onto a universal curve (in black). [(e)-(h)] Same as (a)-(d), but for a smaller initial number of atoms, N_{low}. The black curve in (h) is the same as in (d), showing that the universality holds also for different atom numbers.

of the normalized time $(t - t_c)/\tau_Q$. In these units, the curves have the same growth rate but are still relatively shifted in time. This highlights the fact that τ_Q is the timescale dominating the process of condensate growth, while the shift indicates again the presence of a delay in the condensate onset, having a dependence on τ_Q different than that of the growth timescale τ_1. The behavior of the timescales of condensate formation and of this delay becomes clear in Fig. 4.6 (c), which reports the results for τ_1 and $t_{50\%}$, obtained from the erf-function fits performed in (a). A linear scaling of both parameters with τ_Q clearly appears (the black solid and red dot-dashed lines represent linear fits of $\tau_1(\tau_Q)$ and $t_{50\%}(\tau_Q)$, respectively). While, however, τ_1 goes to zero in the limit of $\tau_Q \to 0$, i.e., for increasingly faster ramps, $t_{50\%}$ goes to a finite value. We find that the value of this finite offset is of the same order as the latency time Δt measured for the fast ramps (which are the actual case of $\tau_Q \to 0$). This is consistent with the presence of a minimum latency time required by the system, after the temperature has crossed the critical point at any rate q, before exhibiting the onset of condensation.

This is confirmed by performing the same analysis for N_{low} [see Figs. 4.6 (e)-(h)]. By comparing the linear fits of $t_{50\%}(\tau_Q)$ [panels (c) and (g)], we notice that the minimum delay

HIGH N	
τ_1	$0.120(5)\tau_Q - 1(4)$ ms
$t_{50\%}$	$0.246(4)\tau_Q + 92(3)$ ms
LOW N	
τ_1	$0.128(4)\tau_Q - 8(6)$ ms
$t_{50\%}$	$0.259(9)\tau_Q + 135(9)$ ms

Table 4.1: Results of the linear fits, reported in panels (c) and (g) of Fig. 4.6, for τ_1 and $t_{50\%}$ as a function of τ_Q, for high and low N, respectively.

increases when the atom number decreases. The characteristic time τ_1 appears instead again to be proportional to τ_Q, with a similar proportionality factor for both regimes of atom numbers.

The results of the linear fits on $t_{50\%}(\tau_Q)$ and $\tau_1(\tau_Q)$ are reported in Table 4.1.

Thanks to the above analysis, it is possible to identify a dimensionless *universal time* $(t - t_c - t_{50\%})/\tau_Q$. In panels (d) and (h) of Fig. 4.6, the same condensate growth data are plotted as a function of this new timescale, for N_{high} and N_{low}, respectively. Thanks to the observed linear scaling of both τ_Q and $t_{50\%}$ with τ_Q, all curves collapse on each other. This occurs not only at the origin of the new horizontal axis, where the curves overlap due to the definition of $t_{50\%}$, but also in any other point, indicating the presence of universality. The universal growth curve is the same for both atom number ranges that have been explored. In fact, the black line shown in Fig. 4.6 (h) corresponds to the best fit for the N_{high} data of Fig. 4.6 (d) and perfectly overlaps also on the low atom number data. This result goes beyond a simple interpretation in terms of instantaneous thermal equilibrium: indeed the overlap occurs for ramp rates in a rather broad range, from the quasi-adiabatic evaporation rates (e.g. $q \sim 20\,\text{kHz/s}$) to the higher ones ($q \sim 300\,\text{kHz/s}$), where the condensate formation clearly occurs in an out-of-equilibrium condition, as was observed in Fig. 4.2.

Conclusions & considerations on the formation of the BEC order parameter

Let us now draw some intermediate conclusions regarding the formation of the condensate order parameter. We analyzed the role of the cooling rate q in the BEC onset and growth dynamics, exploring a wide range of values of q, for two sets of atomic ensembles with different initial atom numbers ($N_{\text{high}} = 3.6(3) \times 10^7$, $N_{\text{low}} = 1.7(9) \times 10^7$). We found that for fast ramps ($q \geq 400\,\text{kHz/s}$ for N_{high} and $q \geq 300\,\text{kHz/s}$ for N_{low}) the condensate order parameter formation takes place after the end of the ramp, as a post-quench process during the equilibration at constant atom number. We observed the presence of a fixed delay in the BEC onset with respect to the time t_c, at which the critical temperature is crossed. This delay does not depend on the cooling rate but rather on the density, which determines the collisional time in the thermal cloud. Our observations are in agreement with earlier studies of condensate formation after sudden quenches, where such a delay was already identified as *latency time* [13, 14].

For linear evaporation ramps of lower rate q, we notice that the condensate formation in our system is characterized, during the evaporation, by a *universal exponential growth* taking place on a timescale $\tau_1 \simeq 0.125\tau_Q$, for both regimes of atom numbers that were investigated. A finite delay was also identified, corresponding, in the limit of $\tau_Q \to 0$, to the latency time observed for the post-quench dynamics.

The recent theoretical analysis of [23] pointed out the role of another timescale, associated with the Kibble-Zurek mechanism, the freeze-out time $\hat{t}$, which is predicted to affect the growth of the condensate at early stages and should scale with the square root of τ_Q. Our experimental observations, that at the beginning were actually aimed at the identification of effects related to this freeze-out time, however, do not show evidences of $\hat{t}$. This is likely caused by the effect of the latency time, associated with the finite collisional time in our samples, which is not included in the theoretical model of [23]. An effect of $\hat{t}$ on the condensate formation dynamics might be possibly observed performing similar experiments in samples with a much higher density, where the latency time is expected to be shorter.

4.4 Evolution of the order parameter fluctuations

In Sec. 4.3 we investigated the timescales that characterize the growth of the BEC order parameter as a function of the cooling rate.

We now focus on the evolution of the spatial fluctuations of the order parameter. In fact, as shown in the theoretical simulations of Ref. [22], when the condensate forms, the system is initially characterized by a turbulent regime, with strong spatial fluctuations of the phase of the order parameter. Then a coarse-graining dynamics leads to the formation of phase domains, that eventually evolve into isolated quantized vortices during the subsequent relaxation dynamics.

Different techniques can be used to detect spatial phase fluctuations in an ultracold gas. For instance, one can take absorption images after a ballistic expansion of the atomic cloud, and exploit the fact that spatial phase fluctuations present in situ evolve into density ripples after a long enough TOF. This technique was used to measure spatial phase fluctuations in Bose gases close to the 1D regime, where the reduced dimensionality limits the long-range coherence, enhancing the phase fluctuations [108, 188, 189]. Bragg spectroscopy techniques were also used in analogous systems, connecting the width of the momentum distribution to the average length of the original phase domains [189, 190].

Quantum turbulence [191] in ultracold gases was recently studied also by mechanically introducing it by rapid perturbations of the confining optical or magnetic potentials, and observing its relaxation phenomena [192, 193, 106, 194, 195, 196, 197, 198]. In these works, the turbulent regime was investigated by means of interferometric techniques or through the direct detection and counting of the quantized vortices that remain as late-time relics originating from the initial turbulence.

In our experiment, we investigate the phase fluctuations originated by a rapid cooling across the BEC critical point. After such a temperature quench, the generated turbulent regime typically relaxes towards the BEC ground state, sometimes leaving isolated topological excitations, such as vortices [25, 198] and transverse solitonic vortices in elongated systems [199, 56, 200]. These defects can be detected after timescales of the order of at least a few hundred of ms, and were used in previous experiments [19, 24, 25] to investigate the powerlaw scaling, predicted by the Kibble-Zurek mechanism, of the density of defects with the cooling rate.

The aim of this work is instead the investigation of the early-time turbulent phase, generated by the rapid cooling across the transition point, and the identification of its typical relaxation timescales.

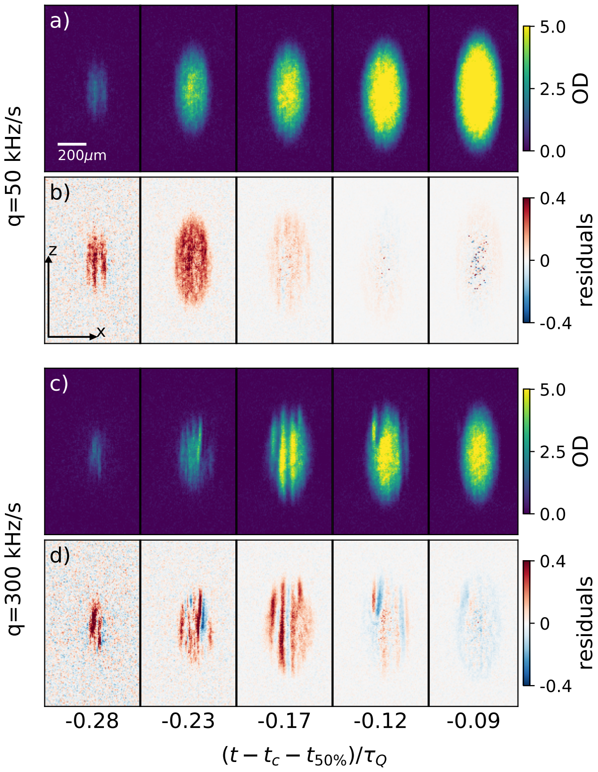

Figure 4.7: Relaxation dynamics of the fluctuations of the order parameter. (a) Pictures of the BEC component as a function of the universal timescale of the condensate growth defined in Sec. 4.3.2. (b) The residuals $h(x, z)$ between the OD shown in (a) and the average $\overline{\mathrm{OD}}$ at the same universal time, normalized by the peak $\overline{\mathrm{OD}}$ at each time, are larger shortly after the BEC onset and then decay when the initially turbulent system relaxes to the smooth final equilibrium state. Panels (a), (b) and (c), (d) correspond to evaporation rates of $q = 50\,\mathrm{kHz/s}$ and $q = 300\,\mathrm{kHz/s}$, respectively. All images are taken after the same time of flight $t_{\mathrm{tof}} = 50\,\mathrm{ms}$ and share the same spatial scale and coordinate axis indicated in (a) and (b).

To measure the fluctuations of the order parameter, we exploit the method used by [108, 188, 189], using the same TOF images that already allowed for the study of the timescales of the order parameter growth (see Sec. 4.3). For this analysis we consider the instantaneous images taken at times $t > t_c$. We subtract the thermal component resulting from the Bose fit to obtain the OD of the sole condensate. Panels (a) and (c) of Fig. 4.7 show the condensate OD of some of such images, in the dimensionless universal timeframe $(t - t_c - t_{50\%})/\tau_Q$ found in Sec. 4.3.2, shortly after the condensation onset and during the order parameter growth, for a low and a high evaporation rate, respectively. One can clearly observe the presence of density ripples, similar to the ones observed in the TOF expansion of nearly 1D clouds in [108], which were in that case caused by the reduced dimensionality of the system, while in our case they are due to the in situ turbulent phase originating from the finite-rate cooling.

In order to investigate the evolution of the fluctuations of the order parameter, we compare each BEC profile to the average over several repetitions in the same experimental conditions. Panels (b) and (d) of Fig. 4.7 show the residuals $h(x, z; t)$, calculated as the difference between the OD of each image in panels (a) and (c) and the average $\overline{\mathrm{OD}}$ at the

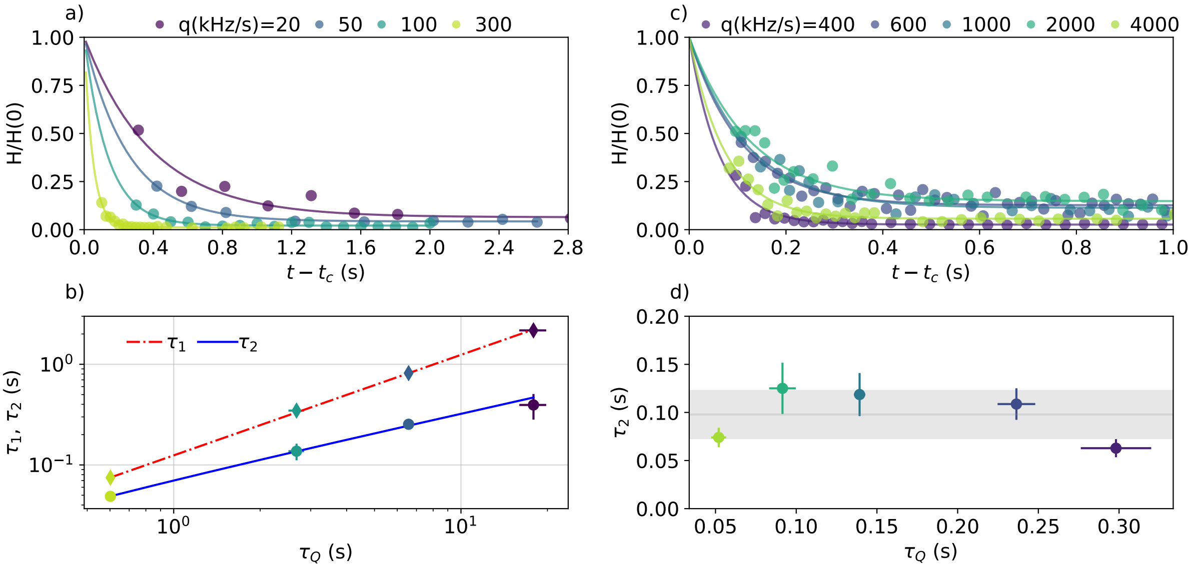

Figure 4.8: (a) Decay of the order parameter fluctuations $H(t-t_c)$ in the case of low evaporation rates, normalized to the initial value $H(0)$, as defined in the text. (b) Time constant τ_2 of the exponential fit of the decay of the fluctuations (dots), compared to the condensate growth rate τ_1, as a function of the ramp time τ_Q. Linear fits in the log-log scale highlight the power-law scaling of the two quantities, with an exponent 1 (linear scaling) for τ_1 (red, dot-dashed line) and an exponent 0.6 for τ_2 (blue, solid line). (c) Same as (a) but for high evaporation rates, notice the different scale of the $t-t_c$ axis. (d) In contrast to the low evaporation rates, there is no clear dependence of τ_2, extracted from the exponential fit, on the quench time τ_Q, with τ_2 resulting fairly constant at a value of (98 ± 25) ms (gray area)

corresponding time, normalized by the peak $\overline{\mathrm{OD}}$:

$$h(x,z) = \frac{(\mathrm{OD} - \overline{\mathrm{OD}})}{\overline{\mathrm{OD}}_{\mathrm{max}}}. \tag{4.5}$$

In the early stages after the appearance of the BEC, a large amount of fluctuations is present, both at large and small scale, which then decay during the growth of the condensate. Comparing the two evaporation rates, we notice the formation of a larger amount of fluctuations for the higher cooling rate, which then decay on a longer timescale in the universal time that characterizes the BEC growth. This means that for a higher cooling rate, at the same stage of the BEC growth (i.e. for the same condensate fraction), the order parameter presents a larger amount of fluctuations.

We quantify the total amount of fluctuations at each time by calculating the quantity:

$$H(t) = \frac{\int \sigma_{\mathrm{OD}}(x,z;t)dxdz}{\int \overline{\mathrm{OD}}(x,z;t)dxdz}, \tag{4.6}$$

where $\sigma_{\mathrm{OD}}(x,z;t)$ is the root mean squared (RMS) deviation of the set of ODs at time t and the integration is performed over the whole area of the image. In Fig. 4.8 the amount of fluctuations $H(t)$, normalized by its initial value $H(0)$, is shown as a function of the absolute time $(t-t_c)$ for different low [(a), $q < 400$] and high [(c), $q \geq 400$] evaporation rates, for the dataset with N_{high}. An exponential decay of the amount of fluctuations clearly appears for all evaporation rates. By fitting $H(t)$ to an exponential, we obtain the time constant τ_2 that characterizes such decay, as a function of τ_Q. Figure 4.8 (b) shows $\tau_2(\tau_Q)$

in log-log scale: the observed linear behavior corresponds to a power-law dependence, with $\tau_2 \propto \tau_Q^{0.63(5)}$. The BEC formation characteristic timescale τ_1, which scales linearly with τ_Q (with a power law of exponent 1), is shown for comparison. The timescales τ_1 and τ_2 clearly scale differently with the characteristic ramp time. This highlights a nontrivial relation between the characteristic time for the BEC order parameter formation and the relaxation timescale of its fluctuations. Figure 4.8 (d) shows the quantities of panel (b) but for high evaporation rates (quasi-instantaneous quenches), where the growth of the condensate and the relaxation of the fluctuations occur after the end of the evaporation ramp. In this case, the decay time τ_2 is fairly constant and on the order of 100 ms, as shown in panel (d) of Fig. 4.8. We notice that this value is similar to that of the latency time for the same range of atom numbers, suggesting also in this case a relation with the collisional rate in the atomic cloud.

The parameters extracted from our analysis are reported in Table 4.2 for all the combinations of atom numbers and evaporation rates that were explored. The large atom number is particularly important for carefully studying the turbulence dynamics in the condensate. Indeed, the atom number that we consider as "low" is actually still larger than typical condensate atom numbers in the literature, especially if one considers other atomic species.

N_{high}							
q (kHz/s)	t_f	τ_Q	t_c	τ_1	t_{50}	τ_2	Δt
20	11	18(3)	3.41 (12)	2.17 (6)	4.43(5)	0.45 (9)	-
50	4.4	6.6(3)	1.85 (2)	0.82 (2)	1.711 (11)	0.25 (3)	-
100	2.2	2.7(2)	1.231 (16)	0.347 (13)	0.774 (7)	0.14 (3)	-
300	0.73	0.602(15)	0.516 (3)	0.075 (2)	0.248 (2)	0.043 (9)	-
400	0.55	0.30(2)	0.453 (5)	0.031 (2)	0.177 (3)	0.069 (4)	0.087 (10)
600	0.37	0.236(12)	0.307 (2)	-	-	0.109 (16)	0.090 (11)
1000	0.22	0.139(4)	0.193 (1)	-	-	0.12 (2)	0.088 (10)
2000	0.11	0.091(8)	0.0940 (9)	-	-	0.13 (3)	0.085 (15)
4000	0.055	0.052(5)	0.0525 (4)	-	-	0.061 (4)	0.083 (17)

N_{low}							
q (kHz/s)	t_f	τ_Q	t_c	τ_1	t_{50}	τ_2	Δt
20	7.5	11.0 (6)	3.87 (9)	1.41 (3)	2.74 (3)	0.80 (11)	-
30	5	7.3 (5)	2.68 (10)	0.88 (6)	1.87(4)	-	-
40	3.84	5.4 (4)	2.39 (4)	0.75 (5)	1.57 (4)	0.23 (4)	-
43	3.5	4.5 (3)	2.10(6)	0.60 (5)	1.28 (4)	-	-
50	3.0	4.0 (2)	1.98 (3)	0.54 (3)	1.17 (3)	0.19 (9)	-
75	2.0	1.7 (4)	1.35 (4)	0.22 (4)	0.66 (3)	-	-
200	0.96	0.48 (5)	0.681 (7)	0.054 (3)	0.242 (2)	-	-
300	0.50	0.353 (8)	0.438 (9)	-	-	-	0.140 (2)
750	0.20	0.17 (3)	0.192 (5)	-	-	-	0.14 (2)
1500	0.10	0.06(1)	0.101 (11)	-	-	-	0.20 (3)
3000	0.05	-	0.07 (2)	-	-	-	0.18 (4)

Table 4.2: Relevant timescales for the different ramps for N_{high} (above) and N_{low} (below). All timescales are in seconds. Δt is the latency time measured for fast ramps where condensation occurs as a post-quench process.

4.5 Conclusions and further perspectives

In the work presented in this chapter, the growth of the order parameter and the temporal evolution of its spatial phase fluctuations were investigated. This was done by evaporatively cooling the gas across the critical point for Bose-Einstein condensation by means of radio-frequency ramps of different rates. We studied the evolution of the atomic system, by measuring the effective temperature and condensate fraction from time-of-flight images, capturing the state of the system during and after the end of the cooling ramp. An increasing out-of-equilibrium condition was observed when crossing the critical point at higher rates, which was highlighted by comparing the instantaneous and steady-state condition at each point of the cooling process.

The main focus of this work was the study of the timescales of order parameter formation. We found that the condensate starts forming with a finite delay with respect to the time at which the temperature crosses the critical point. This delay, observed already earlier in rapidly cooled Bose gases, and defined in literature as latency time, is likely to be determined by the finite collisional time of the gas. The comparison of measurements performed in systems of different density, suggests, indeed, an inverse proportionality between the delay and the classical collision rate.

As a consequence of this finite latency time, we observed that, for high evaporation rates, the onset of condensation occurs after the end of the cooling ramp, although the critical temperature is crossed during the ramp. The formation of the condensate follows in this case a universal curve, with an intrinsic growth rate, that does not depend on the quench time τ_Q. These ramps can thus be considered as quasi-instantaneous quenches. In this regime, other works pointed out a break-down of the Kibble-Zurek scaling laws, with the saturation of the number of defects. This is consistent with our results, where the evolution timescales of the system appear not to depend on τ_Q for fast cooling ramps.

For slower evaporation ramps, instead, a condensate starts forming during the ramp. We found that, also in this case, the order parameter follows a universal growth curve, but with a characteristic timescale τ_1 proportional to the quench time τ_Q, as predicted in Ref.[23] for the late-time evolution. Interestingly, the proportionality factor between τ_1 and τ_Q does not seem to depend on the system's density, since identical growth curves were observed, upon rescaling the time-axis by τ_Q, for ensembles with different initial atom numbers. After rescaling the time-axis, we identified, also for the slow ramps, the presence of a constant delay, consistent with the one observed in the high evaporation rate regime, that we attributed to the effect of the finite collisional rate. We could, instead, not find evidence of a quench-dependent delay following the scaling expected for $\hat{t}$ (as $\sim \tau_Q^{0.5}$), as predicted by [23].

We also studied the evolution of the spatial fluctuations of the order parameter formed at the early stage of condensation. A different dependence on the quench time was in this case observed, compared to the condensate density evolution. The decay time of the fluctuations was indeed shown to scale as $\sim \tau_Q^{0.6}$ for the ramps where condensate formation occurs during the evaporative cooling. In the case of fast ramps, instead, a fairly constant decay time of the amount of fluctuations was observed, consistent with the idea that in these cases the timescales of the post-quench dynamics do not depend on the previous cooling rate.

The measurements reported in this chapter regard the cooling at finite rate of a sodium Bose gas, in experimental conditions (trapping potential, temperature, number of atoms, ramp duration) very similar to those of previous studies made in our laboratory [19, 24]. In these works the presence of spontaneously generated topological defects was observed by imaging the system at late times after the critical time, and the Kibble-Zurek scaling was verified for slow enough quench rates. The KZ mechanism should therefore be valid also for our measurements, as suggested by the formation of more pronounced phase fluctuations for faster ramps, as observed in Fig. 4.8. However, further investigations would be important to draw conclusions about the formation and evolution of defects within the system.

A more detailed investigation of the order parameter fluctuations could in this sense be important, for instance studying the evolution of the system correlation length as a function of the cooling rate [76, 190] and comparing it with the timescales found in this work for the order parameter growth and fluctuation decay. An investigation on the evolution of the momenta and energy distributions during the different ramps and in the subsequent relaxation could also be performed, following Ref. [179], in order to study the evolution of the fluctuations spectrum [23].

The deeper understanding of the BEC formation timescales, obtained thanks to this work, could be used as a benchmark for future studies in the same experimental setting. For instance, the knowledge of the characteristic scaling of the BEC growth time with the quench time could be used as a reference to study in real-time the dynamics during the formation of the condensate within an initially thermal cloud. To this aim, one could take multiple images of the out-of-equilibrium system, using a partial transfer imaging technique similar to the one described in Sec. 2.9 or in Ref.[71], where it allowed to follow the dynamics of vortex lines. In particular, it would be interesting to study in real time the first stages of condensate formation, looking for evidence of the early-time coarsening and studying how topological defects emerge out of the initial tangle of phase fluctuations [22]. While for an equilibrium, well-defined condensate, the extraction of a small fraction of atoms only minimally perturbs the system, as shown in Sec. 2.9, for the early stages of condensate formation it is more challenging to apply the same technique. The main challenge is represented by the fact that the outcoupling of atoms can act like an additional evaporation process, modifying the PSD of the system, although minimally. This can lead to modifications of the time at which the critical point is crossed, as well as of the condensation onset time. Such modifications depend on the extraction parameters, making the understanding of the evolution dynamics more difficult. The present work could be used, in this context, to perform a comparison between the dynamics observed in a cloud that is probed using the PTAI multi-frame technique during a cooling ramp and the expected evolution for the same cooling rate.

Other perspectives involve the use of the DMD that I implemented in the experimental apparatus (see Sec. 2.7.2), to study in a deterministic way the effect of local quenches, performing sudden modifications of the optical potential by changing the light patterns projected by the device.

Another important perspective of this work is the development of more efficient cooling procedures, for the production of defect-free equilibrium condensates with a high number of atoms, possibly in a short experimental time. This is particularly relevant in the perspective of using ultracold degenerate quantum gases for quantum simulation, for which systems with a clean and well-controlled state are highly desired. To this regard, the observed different scaling with τ_Q of the timescales for BEC growth and fluctuations decay is particularly relevant. The present work could be, indeed, extended, performing not only linear ramps across the phase transition, but also ramps where the RF evaporation frequency has a more complicated time-dependence. Preliminary measurements were already performed in this direction, implementing, instead of the single linear ramp of this work, three linear ramps: the first one is used to bring the system in the close vicinity of the critical point, the central one to cross the critical region, and the last one to further cool the system and increase the condensate fraction. Such a cooling protocol allows for an independent control of the evaporation rate in the various stages of the condensate formation, providing the possibility of optimally tuning each part of the cooling process. This could be a starting point for the implementation, for instance, of cubic ramps or in general for changing the evaporation frequency in time following *ad-hoc* designed functions.

Bibliography

[1] K. B. Davis et al. “Bose-Einstein Condensation in a Gas of Sodium Atoms”. In: *Phys. Rev. Lett.* **75**.22 (1995), pp. 3969–3973. DOI: `10.1103/PhysRevLett.75.3969` (cit. on pp. 1, 25).

[2] M. H. Anderson et al. “Observation of Bose-Einstein condensation in a dilute atomic vapor”. In: *Science* **269**.5221 (1995), pp. 198–201. DOI: `10.1126/science.269.5221.198` (cit. on p. 1).

[3] S. Nascimbène et al. “The equation of state of ultracold Bose and Fermi gases: a few examples”. In: *New Journal of Physics* **12**.10 (2010), p. 103026. DOI: `10.1088/1367-2630/12/10/103026` (cit. on pp. 1, 77, 78, 80, 91).

[4] C. Mordini et al. “Single-shot reconstruction of the density profile of a dense atomic gas”. In: *Opt. Express* **28**.20 (2020), pp. 29408–29418. DOI: `10.1364/OE.397567` (cit. on pp. 2, 4, 65, 67, 68, 71, 72, 78, 92).

[5] C. Mordini et al. “Measurement of the Canonical Equation of State of a Weakly Interacting 3D Bose Gas”. In: *Phys. Rev. Lett.* **125**.15 (2020), p. 150404. DOI: `10.1103/PhysRevLett.125.150404` (cit. on pp. 2, 4, 56, 58, 65, 88, 92).

[6] T. W. B. Kibble. “Topology of cosmic domains and strings”. In: *J. Phys. A* **9**.8 (1976), p. 1387. DOI: `https://doi.org/10.1088/0305-4470/9/8/029` (cit. on pp. 2, 17).

[7] W. H. Zurek. “Cosmological experiments in superfluid liquid helium?” In: *Nature* **317** (1985), pp. 505–508. DOI: `10.1038/317505a0` (cit. on pp. 2, 17, 20).

[8] C. Bäuerle et al. “Laboratory simulation of cosmic string formation in the early Universe using superfluid ^{3}He”. In: *Nature* **382** (1996), pp. 332–334. DOI: `10.1038/382332a0` (cit. on pp. 3, 20).

[9] R. Carmi and E. Polturak. “Search for spontaneous nucleation of magnetic flux during rapid cooling of $YBa_2Cu_3O_{7-\delta}$ films through T_c”. In: *Phys. Rev. B* **60**.10 (1999), pp. 7595–7600. DOI: `10.1103/PhysRevB.60.7595` (cit. on pp. 3, 20).

[10] R. Monaco et al. “Zurek-Kibble Mechanism for the Spontaneous Vortex Formation in Nb-Al/Al_{ox}/Nb Josephson Tunnel Junctions: new Theory and Experiment”. In: *Phys. Rev. Lett.* **96**.18 (2006), p. 180604. DOI: `10.1103/PhysRevLett.96.180604` (cit. on p. 3).

[11] K. Pyka et al. “Topological defect formation and spontaneous symmetry breaking in ion Coulomb crystals”. In: *Nature Communications* **4**.1 (2013), p. 2291. DOI: `10.1038/ncomms3291` (cit. on pp. 3, 20).

[12] S. Ulm et al. “Observation of the Kibble–Zurek scaling law for defect formation in ion crystals”. In: *Nature Communications* **4**.1 (2013), p. 2290. DOI: `10.1038/ncomms3290` (cit. on pp. 3, 20).

[13] H.-J. Miesner et al. “Bosonic Stimulation in the Formation of a Bose-Einstein Condensate”. In: *Science* **279**.5353 (1998), pp. 1005–1007. DOI: `10.1126/science.279.5353.1005` (cit. on pp. 3, 23, 102, 104).

[14] M. Köhl et al. “Growth of Bose-Einstein Condensates from Thermal Vapor”. In: *Phys. Rev. Lett.* **88**.8 (2002), p. 080402. DOI: `10.1103/PhysRevLett.88.080402` (cit. on pp. 3, 23, 100, 102, 104).

[15] J. R. Ensher et al. “Bose-Einstein Condensation in a Dilute Gas: Measurement of Energy and Ground-State Occupation”. In: *Phys. Rev. Lett.* **77**.25 (1996), pp. 4984–4987. DOI: `10.1103/PhysRevLett.77.4984` (cit. on pp. 3, 98).

[16] L. E. Sadler et al. “Spontaneous symmetry breaking in a quenched ferromagnetic spinor Bose-Einstein condensate”. In: *Nature* **443**.7109 (2006), pp. 312–315. DOI: `10.1038/nature05094` (cit. on pp. 3, 21).

[17] T. Donner et al. “Critical Behavior of a Trapped Interacting Bose Gas”. In: *Science* **315**.5818 (2007), pp. 1556–1558. DOI: `10.1126/science.1138807` (cit. on pp. 3, 20).

[18] N. Navon et al. “Critical dynamics of spontaneous symmetry breaking in a homogeneous Bose gas”. In: *Science* **347**.6218 (2015), pp. 167–170. DOI: `10.1126/science.1258676` (cit. on pp. 3, 20).

[19] G. Lamporesi et al. “Spontaneous creation of Kibble–Zurek solitons in a Bose-Einstein condensate”. In: *Nature Physics* **9**.10 (2013), pp. 656–660. DOI: `10.1038/nphys2734` (cit. on pp. 3, 20, 21, 105, 110).

[20] L. Corman et al. “Quench-Induced Supercurrents in an Annular Bose Gas”. In: *Phys. Rev. Lett.* **113**.13 (2014), p. 135302. DOI: `10.1103/PhysRevLett.113.135302` (cit. on pp. 3, 20).

[21] L. Chomaz et al. “Emergence of coherence via transverse condensation in a uniform quasi-two-dimensional Bose gas”. In: *Nature Communications* **6**.1 (2015), p. 6162. DOI: `10.1038/ncomms7162` (cit. on pp. 3, 20).

[22] I.-K. Liu et al. “Dynamical equilibration across a quenched phase transition in a trapped quantum gas”. In: *Communications Physics* **1**.1 (2018), p. 24. DOI: `10.1038/s42005-018-0023-6` (cit. on pp. 3, 19, 105, 110).

[23] I.-K. Liu et al. “Kibble-Zurek dynamics in a trapped ultracold Bose gas”. In: *Phys. Rev. Research* **2**.3 (2020), p. 033183. DOI: `10.1103/PhysRevResearch.2.033183` (cit. on pp. 3, 17, 19, 22, 96, 105, 109, 110).

[24] S. Donadello et al. “Creation and counting of defects in a temperature-quenched Bose-Einstein condensate”. In: *Phys. Rev. A* **94**.2 (2016), p. 023628. DOI: `10.1103/PhysRevA.94.023628` (cit. on pp. 3, 19–22, 105, 110).

[25] J. Goo, Y. Lim, and Y. Shin. “Defect Saturation in a Rapidly Quenched Bose Gas”. In: *Phys. Rev. Lett.* **127**.11 (2021), p. 115701. DOI: `10.1103/PhysRevLett.127.115701` (cit. on pp. 3, 20–22, 105).

[26] J. Goo et al. "Universal Early Coarsening of Quenched Bose Gases". In: *Phys. Rev. Lett.* **128**.13 (2022), p. 135701. DOI: `10.1103/PhysRevLett.128.135701` (cit. on pp. 3, 20–22).

[27] L. Wolswijk et al. "Measurement of the order parameter and its spatial fluctuations across Bose-Einstein condensation". In: *Phys. Rev. A* **105**.3 (2022), p. 033316. DOI: `10.1103/PhysRevA.105.033316` (cit. on pp. 4, 93).

[28] W. Ketterle, D. S. Durfee, and D. M. Stamper-Kurn. *Making, probing and understanding Bose-Einstein condensates.* 1999 (cit. on pp. 5, 6, 30, 31, 39, 42, 56, 60).

[29] L. Pitaevskii and S. Stringari. *Bose–Einstein Condensation and Superfluidity.* 2nd ed. Oxford University Press, 2016. DOI: `10.1093/acprof:oso/9780198758884.001.0001` (cit. on pp. 6–8, 10, 13–15, 89).

[30] L. P. Pitaevskii. "Vortex lines in an imperfect Bose gas". In: *Sov. Phys. JETP* **13**.2 (1961), pp. 451–454 (cit. on p. 8).

[31] E. P. Gross. "Structure of a quantized vortex in boson systems". In: *Il Nuovo Cimento (1955-1965)* **20**.3 (1961), pp. 454–477. DOI: `10.1007/BF02731494` (cit. on p. 8).

[32] F. J. Poveda-Cuevas et al. "Isothermal compressibility determination across Bose-Einstein condensation". In: *Phys. Rev. A* **92**.1 (2015), p. 013638. DOI: `10.1103/PhysRevA.92.013638` (cit. on p. 13).

[33] S. Giorgini, L. P. Pitaevskii, and S. Stringari. "Condensate fraction and critical temperature of a trapped interacting Bose gas". In: *Phys. Rev. A* **54**.6 (1996), R4633–R4636. DOI: `10.1103/PhysRevA.54.R4633` (cit. on pp. 15, 87).

[34] F. Dalfovo et al. "Theory of Bose-Einstein condensation in trapped gases". In: *Rev. Mod. Phys.* **71**.3 (1999), pp. 463–512. DOI: `10.1103/RevModPhys.71.463` (cit. on p. 15).

[35] G. Jaeger. "The Ehrenfest Classification of Phase Transitions: Introduction and Evolution". In: *Archive for History of Exact Sciences* **53**.1 (1998), pp. 51–81. DOI: `10.1007/s004070050021` (cit. on p. 16).

[36] A. del Campo and W. H. Zurek. "Universality of phase transition dynamics: Topological defects from symmetry breaking". In: *International Journal of Modern Physics A* **29**.08 (2014), p. 1430018. DOI: `10.1142/S0217751X1430018X` (cit. on pp. 17, 19, 22).

[37] J. Beugnon and N. Navon. "Exploring the Kibble-Zurek mechanism with homogeneous Bose gases". In: *J. Phys. B: At. Mol. Opt. Phys.* **50**.022002 (2017). URL: `https://iopscience.iop.org/article/10.1088/1361-6455/50/2/022002` (cit. on pp. 17, 20, 22).

[38] L. Dai et al. "Generic Indicators for Loss of Resilience Before a Tipping Point Leading to Population Collapse". In: *Science* **336**.6085 (2012), pp. 1175–1177. DOI: `10.1126/science.1219805` (cit. on p. 17).

[39] M. Gomez, D. E. Moulton, and D. Vella. "Critical slowing down in purely elastic 'snap-through' instabilities". In: *Nature Physics* **13**.2 (2017), pp. 142–145. DOI: `10.1038/nphys3915` (cit. on p. 17).

[40] V. Dakos et al. “Slowing down as an early warning signal for abrupt climate change”. In: *Proceedings of the National Academy of Sciences* **105**.38 (2008), pp. 14308–14312. DOI: `10.1073/pnas.0802430105` (cit. on p. 17).

[41] A. J. Veraart et al. “Recovery rates reflect distance to a tipping point in a living system”. In: *Nature* **481**.7381 (2012), pp. 357–359. DOI: `10.1038/nature10723` (cit. on p. 17).

[42] Y. Zhu et al. “Unconventional slowing down of electronic recovery in photoexcited charge-ordered La1/3Sr2/3FeO3”. In: *Nature Communications* **9**.1 (2018), p. 1799. DOI: `10.1038/s41467-018-04199-4` (cit. on p. 17).

[43] T. Kibble. “Some implications of a cosmological phase transition”. In: *Phys. Rep.* **67**.1 (1980), pp. 183–199. DOI: `10.1016/0370-1573(80)90091-5` (cit. on p. 17).

[44] W. Zurek. “Cosmological experiments in condensed matter systems”. In: *Physics Reports* **276**.4 (1996), pp. 177–221. DOI: `https://doi.org/10.1016/S0370-1573(96)00009-9` (cit. on pp. 17, 20).

[45] A. Das, J. Sabbatini, and W. H. Zurek. “Winding up superfluid in a torus via Bose Einstein condensation”. In: *Scientific Reports* **2**.1 (2012), p. 352. DOI: `10.1038/srep00352` (cit. on p. 19).

[46] D. Sadhukhan et al. “Sonic horizons and causality in phase transition dynamics”. In: *Phys. Rev. B* **101**.14 (2020), p. 144429. DOI: `10.1103/PhysRevB.101.144429` (cit. on p. 19).

[47] I. Chuang et al. “Cosmology in the Laboratory: Defect Dynamics in Liquid Crystals”. In: *Science* **251**.4999 (1991), pp. 1336–1342. DOI: `10.1126/science.251.4999.1336` (cit. on p. 20).

[48] M. J. Bowick et al. “The Cosmological Kibble Mechanism in the Laboratory: String Formation in Liquid Crystals”. In: *Science* **263**.5149 (1994), pp. 943–945. DOI: `10.1126/science.263.5149.943` (cit. on p. 20).

[49] P. C. Hendry et al. “Generation of defects in superfluid ^{4}He as an analogue of the formation of cosmic strings”. In: *Nature* **368**.6469 (1994), pp. 315–317. DOI: `10.1038/368315a0` (cit. on p. 20).

[50] V. M. H. Ruutu et al. “Vortex formation in neutron irradiated ^{3}He as an analogue of cosmological defect formation”. In: *Nature* **382** (1996), pp. 334–336. DOI: `doi:10.1038/382334a0` (cit. on p. 20).

[51] R. Carmi, E. Polturak, and G. Koren. “Observation of Spontaneous Flux Generation in a Multi-Josephson-Junction Loop”. In: **84**.21 (2000), pp. 4966–4969. DOI: `10.1103/PhysRevLett.84.4966` (cit. on p. 20).

[52] R. Monaco et al. “Spontaneous fluxoid formation in superconducting loops”. In: *Phys. Rev. B* **80**.18 (2009), p. 180501. DOI: `10.1103/PhysRevB.80.180501` (cit. on p. 20).

[53] S. Ejtemaee and P. C. Haljan. “Spontaneous nucleation and dynamics of kink defects in zigzag arrays of trapped ions”. In: *Phys. Rev. A* **87**.5 (2013), p. 051401. DOI: `10.1103/PhysRevA.87.051401` (cit. on p. 20).

[54] T. Kibble. “Phase-transition dynamics in the lab and the universe”. In: *Physics Today* **60**.9 (2007), pp. 47–52. DOI: `10.1063/1.2784684` (cit. on p. 20).

[55] C. N. Weiler et al. “Spontaneous vortices in the formation of Bose-Einstein condensates”. In: *Nature* **455** (2008), pp. 948–952. DOI: `10.1038/nature07334` (cit. on pp. 20, 21).

[56] S. Donadello et al. “Observation of Solitonic Vortices in Bose-Einstein Condensates”. In: *Phys. Rev. Lett.* **113**.6 (2014), p. 065302. DOI: `10.1103/PhysRevLett.113.065302` (cit. on pp. 20, 21, 105).

[57] J. Dziarmaga. “Dynamics of a quantum phase transition and relaxation to a steady state”. In: *Advances in Physics* **59**.6 (2010), pp. 1063–1189. DOI: `10.1080/00018732.2010.514702` (cit. on p. 21).

[58] D. Chen et al. “Quantum Quench of an Atomic Mott Insulator”. In: *Phys. Rev. Lett.* **106**.23 (2011), p. 235304. DOI: `10.1103/PhysRevLett.106.235304` (cit. on p. 21).

[59] S. Braun et al. “Emergence of coherence and the dynamics of quantum phase transitions”. In: *Proceedings of the National Academy of Sciences* **112**.12 (2015), pp. 3641–3646. DOI: `10.1073/pnas.1408861112` (cit. on p. 21).

[60] B. Damski and W. H. Zurek. “How to fix a broken symmetry: quantum dynamics of symmetry restoration in a ferromagnetic Bose–Einstein condensate”. In: *New Journal of Physics* **10**.4 (2008), p. 045023. DOI: `10.1088/1367-2630/10/4/045023` (cit. on p. 21).

[61] B. Damski and W. H. Zurek. “Quantum phase transition in space in a ferromagnetic spin-1 Bose–Einstein condensate”. In: *New Journal of Physics* **11**.6 (2009), p. 063014. DOI: `10.1088/1367-2630/11/6/063014` (cit. on p. 21).

[62] J. Sabbatini, W. H. Zurek, and M. J. Davis. “Phase Separation and Pattern Formation in a Binary Bose-Einstein Condensate”. In: *Phys. Rev. Lett.* **107**.23 (2011), p. 230402. DOI: `10.1103/PhysRevLett.107.230402` (cit. on p. 21).

[63] T. Świsłocki et al. “Double Universality of a Quantum Phase Transition in Spinor Condensates: Modification of the Kibble-Żurek Mechanism by a Conservation Law”. In: *Phys. Rev. Lett.* **110**.4 (2013), p. 045303. DOI: `10.1103/PhysRevLett.110.045303` (cit. on p. 21).

[64] S. De et al. “Quenched binary Bose-Einstein condensates: Spin-domain formation and coarsening”. In: *Phys. Rev. A* **89**.3 (2014), p. 033631. DOI: `10.1103/PhysRevA.89.033631` (cit. on p. 21).

[65] M. Anquez et al. “Quantum Kibble-Zurek Mechanism in a Spin-1 Bose-Einstein Condensate”. In: *Phys. Rev. Lett.* **116**.15 (2016), p. 155301. DOI: `10.1103/PhysRevLett.116.155301` (cit. on p. 21).

[66] S. Kang et al. “Crossover from weak to strong quench in a spinor Bose-Einstein condensate”. In: *Phys. Rev. A* **101**.2 (2020), p. 023613. DOI: `10.1103/PhysRevA.101.023613` (cit. on p. 21).

[67] B. Ko, J. W. Park, and Y. Shin. “Kibble–Zurek universality in a strongly interacting Fermi superfluid”. In: *Nature Physics* **15**.12 (2019), pp. 1227–1231. DOI: `10.1038/s41567-019-0650-1` (cit. on p. 21).

[68] X.-P. Liu et al. “Dynamic formation of quasicondensate and spontaneous vortices in a strongly interacting Fermi gas”. In: *Phys. Rev. Research* **3**.4 (2021), p. 043115. DOI: `10.1103/PhysRevResearch.3.043115` (cit. on p. 21).

[69] S. Donadello. “Observation of the Kibble-Zurek mechanism in a bosonic gas”. PhD thesis. Università di Trento, 2016. URL: `http://eprints-phd.biblio.unitn.it/1694/1/Donadello_Thesis_.pdf` (cit. on pp. 21, 35, 40).

[70] S. Serafini. “Dynamics of Vortices and their Interactions in Bose-Einstein Condensates”. PhD thesis. Università di Trento, 2017. URL: `http://eprints-phd.biblio.unitn.it/1946/2/Serafini_PhD_Thesis.pdf` (cit. on pp. 21, 31–33, 39, 40).

[71] S. Serafini et al. “Dynamics and Interaction of Vortex Lines in an Elongated Bose-Einstein Condensate”. In: *Phys. Rev. Lett.* **115**.17 (2015), p. 170402. DOI: `10.1103/PhysRevLett.115.170402` (cit. on pp. 21, 110).

[72] P. M. Chesler, A. M. García-García, and H. Liu. “Defect Formation beyond Kibble-Zurek Mechanism and Holography”. In: *Phys. Rev. X* **5**.2 (2015), p. 021015. DOI: `10.1103/PhysRevX.5.021015` (cit. on p. 21).

[73] J. Sonner, A. del Campo, and W. H. Zurek. “Universal far-from-equilibrium dynamics of a holographic superconductor”. In: *Nature Communications* **6**.1 (2015), p. 7406. DOI: `10.1038/ncomms8406` (cit. on p. 22).

[74] H.-B. Zeng, C.-Y. Xia, and A. del Campo. *Universal breakdown of Kibble-Zurek scaling in fast quenches across a phase transition*. 2022. DOI: `10.48550/ARXIV.2204.13529` (cit. on p. 22).

[75] J. Dalibard. “Collisional dynamics of ultra-cold atomic gases”. In: *Bose-Einstein Condensation in Atomic Gases*. IOS Press, 1999, pp. 321–349 (cit. on pp. 23, 102).

[76] M. Hugbart et al. “Population and phase coherence during the growth of an elongated Bose-Einstein condensate”. In: *Phys. Rev. A* **75**.1 (2007), p. 011602. DOI: `10.1103/PhysRevA.75.011602` (cit. on pp. 23, 110).

[77] K. M. R. van der Stam et al. “Large atom number Bose-Einstein condensate of sodium”. In: *Review of Scientific Instruments* **78**.1 (2007), p. 013102. DOI: `10.1063/1.2424439` (cit. on p. 25).

[78] D. A. Steck. *Sodium D Line Data*. 2019. URL: `https://steck.us/alkalidata/sodiumnumbers.pdf` (cit. on pp. 26, 30, 39).

[79] G. Lamporesi et al. “Compact high-flux source of cold sodium atoms”. In: *Review of Scientific Instruments* **84**.6 (2013), p. 063102. DOI: `10.1063/1.4808375` (cit. on pp. 26, 29, 30).

[80] G. Colzi et al. “Production of large Bose-Einstein condensates in a magnetic-shield-compatible hybrid trap”. In: *Phys. Rev. A* **97**.5 (2018), p. 053625. DOI: `10.1103/PhysRevA.97.053625` (cit. on p. 26).

[81] G. Camy, C. Bordé, and M. Ducloy. “Heterodyne saturation spectroscopy through frequency modulation of the saturating beam”. In: *Optics Communications* **41**.5 (1982), pp. 325–330. DOI: `https://doi.org/10.1016/0030-4018(82)90406-0` (cit. on p. 27).

[82] Thorlabs. *Diaphragm Shutters with Controller*. URL: `https://www.thorlabs.com/newgrouppage9.cfm?objectgroup_id=6619#6918` (cit. on p. 27).

[83] A. Franzen. *ComponentLibrary; a free vector graphics library for optics*. 2006. URL: `http://www.gwoptics.org/ComponentLibrary/` (cit. on p. 28).

[84] R. Grimm, M. Weidemüller, and Y. B. Ovchinnikov. *Optical dipole traps for neutral atoms*. 1999 (cit. on pp. 29, 51).

[85] C. Mordini. “Measurement of the density profile of quantized vortices and of the equation of state in a 3D interacting Bose gas”. PhD thesis. Università di Trento, 2019. URL: `http://eprints-phd.biblio.unitn.it/3728/` (cit. on pp. 32, 40, 45, 56, 60, 61).

[86] A. L. Migdall et al. “First Observation of Magnetically Trapped Neutral Atoms”. In: *Phys. Rev. Lett.* **54**.24 (1985), pp. 2596–2599. DOI: `10.1103/PhysRevLett.54.2596` (cit. on p. 30).

[87] P. Zeeman. “Over de invloed eener magnetisatie op den aard van het door een stof uitgezonden licht”. In: *Verslagen en Mededeelingen der Kon. Academie van Wetenschappen, Afd. Natuurkunde* **5** (1896), pp. 181–184 (cit. on p. 30).

[88] D. E. Pritchard. “Cooling Neutral Atoms in a Magnetic Trap for Precision Spectroscopy”. In: *Phys. Rev. Lett.* **51**.15 (1983), pp. 1336–1339. DOI: `10.1103/PhysRevLett.51.1336` (cit. on p. 31).

[89] E. Majorana. “Atomi orientati in campo magnetico variabile”. In: *Il Nuovo Cimento (1924-1942)* **9**.2 (1932), pp. 43–50. DOI: `10.1007/BF02960953` (cit. on p. 31).

[90] S. Serafini. “Realization of a magnetic trap for sodium Bose-Einstein condensates”. Master Thesis. Università di Trento, 2012 (cit. on pp. 31, 33, 39).

[91] E. Fava. “Static and dynamics properties of a miscible two-component Bose-Einstein condensate”. PhD thesis. Università di Trento, 2018. URL: `http://eprints-phd.biblio.unitn.it/2789/1/PhD_Fava.pdf` (cit. on p. 33).

[92] *Marconi Instruments 2024 Operation Manual*. URL: `http://manuals.repeater-builder.com/te-files/MARCONI/MARCONI` (cit. on pp. 34, 66).

[93] *Mini-Circuits ZHL-100W-272+ High Power Amplifier*. URL: `https://www.minicircuits.com/WebStore/dashboard.html?model=ZHL-100W-272%2B` (cit. on pp. 34, 66).

[94] P. T. Starkey et al. “A scripted control system for autonomous hardware-timed experiments”. In: *Review of Scientific Instruments* **84**.8 (2013), p. 085111. DOI: `10.1063/1.4817213` (cit. on p. 35).

[95] *the labscript suite*. 2020. URL: `https://labscriptsuite.org/` (cit. on p. 35).

[96] T. H. group. *HDF5*. URL: `https://portal.hdfgroup.org/display/HDF5/Introduction+to+HDF5` (cit. on p. 36).

[97] W. Ketterle et al. “High densities of cold atoms in a dark spontaneous-force optical trap”. In: *Phys. Rev. Lett.* **70**.15 (1993), pp. 2253–2256. DOI: `10.1103/PhysRevLett.70.2253` (cit. on p. 36).

[98] M. Inguscio and L. Fallani. *Atomic Physics: Precise Measurements and Ultracold Matter*. Oxford University Press, 2013. DOI: `DOI:10.1093/acprof:oso/9780198525844.001.0001` (cit. on pp. 36, 39).

[99] E. L. Raab et al. “Trapping of Neutral Sodium Atoms with Radiation Pressure”. In: *Phys. Rev. Lett.* **59**.23 (1987), pp. 2631–2634. DOI: `10.1103/PhysRevLett.59.2631` (cit. on p. 36).

[100] G. Colzi et al. “Sub-Doppler cooling of sodium atoms in gray molasses”. In: *Phys. Rev. A* **93**.2 (2016), p. 023421. DOI: `10.1103/PhysRevA.93.023421` (cit. on p. 38).

[101] M. S. Shahriar et al. “Continuous polarization-gradient precooling-assisted velocity-selective coherent population trapping”. In: *Phys. Rev. A* **48**.6 (1993), R4035–R4038. DOI: `10.1103/PhysRevA.48.R4035` (cit. on p. 38).

[102] M. Weidemüller et al. “A Novel Scheme for Efficient Cooling below the Photon Recoil Limit”. In: *Europhysics Letters (EPL)* **27**.2 (1994), pp. 109–114. DOI: `10.1209/0295-5075/27/2/006` (cit. on p. 38).

[103] G. Grynberg and J.-Y. Courtois. “Proposal for a Magneto-Optical Lattice for Trapping Atoms in Nearly-Dark States”. In: *Europhysics Letters (EPL)* **27**.1 (1994), pp. 41–46. DOI: `10.1209/0295-5075/27/1/008` (cit. on p. 38).

[104] G. Colzi. “A new apparatus to simulate fundamental interactions with ultracold atoms”. PhD thesis. Università di Trento, 2018. URL: `http://eprints-phd.biblio.unitn.it/2869/2/PhDthesis_Colzi.pdf` (cit. on pp. 38, 40).

[105] W. Ketterle and N. V. Druten. “Evaporative Cooling of Trapped Atoms”. In: ed. by B. Bederson and H. Walther. Vol. 37. Advances In Atomic, Molecular, and Optical Physics. Academic Press, 1996, pp. 181–236. DOI: `https://doi.org/10.1016/S1049-250X(08)60101-9` (cit. on p. 39).

[106] E. A. L. Henn et al. “Evaporation in atomic traps: A simple approach”. In: *American Journal of Physics* **75**.10 (2007), pp. 907–910. DOI: `10.1119/1.2752823` (cit. on pp. 39, 105).

[107] T. Shobu et al. “Optimized evaporative cooling for sodium Bose-Einstein condensation against three-body loss”. In: *Phys. Rev. A* **84**.3 (2011), p. 033626. DOI: `10.1103/PhysRevA.84.033626` (cit. on p. 40).

[108] S. Dettmer et al. “Observation of Phase Fluctuations in Elongated Bose-Einstein Condensates”. In: *Phys. Rev. Lett.* **87**.16 (2001), p. 160406. DOI: `10.1103/PhysRevLett.87.160406` (cit. on pp. 41, 105, 106).

[109] L. Chomaz et al. “Absorption imaging of a quasi-two-dimensional gas: a multiple scattering analysis”. In: *New Journal of Physics* **14**.5 (2012), p. 055001. DOI: `10.1088/1367-2630/14/5/055001` (cit. on p. 42).

[110] M. Horikoshi et al. “Appropriate Probe Condition for Absorption Imaging of Ultracold 6Li Atoms”. In: *Journal of the Physical Society of Japan* **86**.10 (2017), p. 104301. DOI: `10.7566/JPSJ.86.104301` (cit. on pp. 42, 56, 58, 59, 70).

[111] G. Reinaudi et al. “Strong saturation absorption imaging of dense clouds of ultracold atoms”. In: *Opt. Lett.* **32**.21 (2007), pp. 3143–3145. DOI: `10.1364/OL.32.003143` (cit. on pp. 42, 56, 58, 59, 65).

[112] *Stingray technical manual*. URL: `https://www.alliedvision.com/fileadmin/content/documents/products/cameras/Stingray/techman/Stingray_TechMan_en.pdf` (cit. on pp. 42, 75).

[113] D. S. Goodman. “Magnification equations for a two-lens system”. In: *Appl. Opt.* **24**.12 (1985), pp. 1732–1732. DOI: `10.1364/AO.24.001732` (cit. on p. 43).

[114] G. Hollows and N. James. *The Airy disk and diffraction limit.* 2022. URL: https://www.edmundoptics.com/knowledge-center/application-notes/imaging/limitations-on-resolution-and-contrast-the-airy-disk/ (cit. on p. 45).

[115] C. Sheppard. "MICROSCOPY — Overview". In: *Encyclopedia of Modern Optics.* Ed. by R. D. Guenther. Oxford: Elsevier, 2005, pp. 61–69. DOI: https://doi.org/10.1016/B0-12-369395-0/00823-X (cit. on p. 45).

[116] P. Baranowski et al. *Testing and design of a lens system for atom trapping and fluorescence detection.* 2004. DOI: 10.48550/ARXIV.PHYSICS/0412126 (cit. on pp. 47, 50).

[117] M. W. Gempel et al. "An adaptable two-lens high-resolution objective for single-site resolved imaging of atoms in optical lattices". In: *Review of Scientific Instruments* **90**.5 (2019), p. 053201. DOI: 10.1063/1.5086539 (cit. on p. 47).

[118] L. R. Corporation. *OSLO: Optics Software for Layout and Optimization.* URL: https://www.lambdares.com/wp-content/uploads/support/oslo/oslo_edu/oslo-optics-reference.pdf (cit. on p. 47).

[119] W. B. King. "Dependence of the Strehl Ratio on the Magnitude of the Variance of the Wave Aberration". In: *J. Opt. Soc. Am.* **58**.5 (1968), pp. 655–661. DOI: 10.1364/JOSA.58.000655 (cit. on p. 48).

[120] A. Farolfi. "Spin dynamics in two-component Bose-Einstein condensates". PhD thesis. Università di Trento, 2021. URL: https://iris.unitn.it/retrieve/handle/11572/299835/434395/phd_unitn_Arturo_Farolfi.pdf (cit. on p. 48).

[121] A. Farolfi et al. "Design and characterization of a compact magnetic shield for ultracold atomic gas experiments". In: *Review of Scientific Instruments* **90**.11 (2019), p. 115114. DOI: 10.1063/1.5119915 (cit. on p. 48).

[122] Thorlabs. *Optical cage systems.* URL: https://www.thorlabs.com/navigation.cfm?guide_id=2002 (cit. on p. 49).

[123] T. Instruments. *DLP7000 DLP 0.7 XGA 2x LVDS Type A DMD - Datasheet.* 2019. URL: https://www.ti.com/document-viewer/DLP7000/datasheet/revision-history-slvscf26802#SLVSCF26802 (cit. on pp. 51, 52).

[124] G. Del Pace. "Tailored optical potentials for experiments with atomic superfluids". Master Thesis. Università degli studi di Firenze, 2018. URL: https://quantumgases.lens.unifi.it/theses/thesis_delpace_master.pdf (cit. on p. 51).

[125] A. Amico. "Measurement of the equation of state of superfluid Fermi gases of ^{6}Li atoms". Master Thesis. Università degli studi di Firenze, 2015. URL: http://quantumgases.lens.unifi.it/theses/thesis_amico_master.pdf (cit. on pp. 51, 82).

[126] G. Gauthier et al. "Direct imaging of a digital-micromirror device for configurable microscopic optical potentials". In: *Optica* **3**.10 (2016), pp. 1136–1143. DOI: 10.1364/OPTICA.3.001136 (cit. on p. 51).

[127] Y.-Q. Zou et al. "Optical control of the density and spin spatial profiles of a planar Bose gas". In: *Journal of Physics B: Atomic, Molecular and Optical Physics* **54**.8 (2021), 08LT01. DOI: 10.1088/1361-6455/abf298 (cit. on p. 51).

[128] T. Instruments. *Using Lasers with DLP® DMD technology.* 2008. URL: `https://www.ti.com/pdfs/dlpdmd/Using_Lasers_with_DLP(r)_Technology.pdf` (cit. on p. 52).

[129] A. K. Ghatak and K. Thyagarajan. “Fourier Optics I. Spatial Frequency Filtering”. In: *Contemporary Optics.* Boston, MA: Springer US, 1978, pp. 187–222. DOI: `10.1007/978-1-4684-2358-7_6` (cit. on p. 54).

[130] J. W. Goodman. “Introduction to Fourier optics”. In: *Introduction to Fourier optics* **1** (2005) (cit. on p. 54).

[131] H. Helmholtz. “Über integrale der hydrodynamischen Gleichungen welche den Wirbelbewegungen entsprechen”. In: *Journal für die reine und angewandte Mathematik* **55** (1858) (cit. on p. 56).

[132] A. Love. “On the motion of paired vortices with a common axis”. In: *Proceedings of the London Mathematical Society* **1**.1 (1893), pp. 185–194 (cit. on p. 56).

[133] L. Galantucci et al. “Classical and quantum vortex leapfrogging in two-dimensional channels”. In: *Journal of Fluid Mechanics* **912** (2021), A9. DOI: `10.1017/jfm.2020.1094` (cit. on p. 56).

[134] O. Morice, Y. Castin, and J. Dalibard. “Refractive index of a dilute Bose gas”. In: *Phys. Rev. A* **51**.5 (1995), pp. 3896–3901. DOI: `10.1103/PhysRevA.51.3896` (cit. on p. 60).

[135] P. B. Wigley et al. “Non-destructive shadowgraph imaging of ultra-cold atoms”. In: *Opt. Lett.* **41**.20 (2016), pp. 4795–4798. DOI: `10.1364/OL.41.004795` (cit. on pp. 60, 61).

[136] Y. Castin and R. Dum. “Bose-Einstein Condensates in Time Dependent Traps”. In: *Phys. Rev. Lett.* **77**.27 (1996), pp. 5315–5319. DOI: `10.1103/PhysRevLett.77.5315` (cit. on p. 63).

[137] F. Gerbier et al. “Critical Temperature of a Trapped, Weakly Interacting Bose Gas”. In: *Phys. Rev. Lett.* **92**.3 (2004), p. 030405. DOI: `10.1103/PhysRevLett.92.030405` (cit. on p. 64).

[138] F. Gerbier et al. “Experimental study of the thermodynamics of an interacting trapped Bose-Einstein condensed gas”. In: *Phys. Rev. A* **70**.1 (2004), p. 013607. DOI: `10.1103/PhysRevA.70.013607` (cit. on pp. 64, 98).

[139] K. Hueck et al. “Calibrating high intensity absorption imaging of ultracold atoms”. In: *Opt. Express* **25**.8 (2017), pp. 8670–8679. DOI: `10.1364/OE.25.008670` (cit. on p. 65).

[140] M. R. Andrews et al. “Propagation of Sound in a Bose-Einstein Condensate”. In: *Phys. Rev. Lett.* **79**.4 (1997), pp. 553–556. DOI: `10.1103/PhysRevLett.79.553` (cit. on p. 65).

[141] C. C. Bradley, C. A. Sackett, and R. G. Hulet. “Bose-Einstein Condensation of Lithium: Observation of Limited Condensate Number”. In: *Phys. Rev. Lett.* **78**.6 (1997), pp. 985–989. DOI: `10.1103/PhysRevLett.78.985` (cit. on p. 65).

[142] M. Gajdacz et al. “Non-destructive Faraday imaging of dynamically controlled ultracold atoms”. In: *Review of Scientific Instruments* **84**.8 (2013), p. 083105. DOI: `10.1063/1.4818913` (cit. on p. 65).

[143] L. D. Turner, K. F. E. M. Domen, and R. E. Scholten. "Diffraction-contrast imaging of cold atoms". In: *Phys. Rev. A* **72**.3 (2005), p. 031403. DOI: `10.1103/PhysRevA.72.031403` (cit. on p. 65).

[144] D. V. Freilich et al. "Real-Time Dynamics of Single Vortex Lines and Vortex Dipoles in a Bose-Einstein Condensate". In: *Science* **329**.5996 (2010), pp. 1182–1185. DOI: `10.1126/science.1191224` (cit. on p. 65).

[145] A. Ramanathan et al. "Partial-transfer absorption imaging: A versatile technique for optimal imaging of ultracold gases". In: *Review of Scientific Instruments* **83**.8 (2012), p. 083119. DOI: `10.1063/1.4747163` (cit. on p. 65).

[146] S. Mann and R. Picard. "On being 'undigital' with digital cameras: extending dynamic range by combining differently exposed pictures". In: *Proc. IS & T Annual Meeting* **48** (1996) (cit. on p. 66).

[147] R. Bryant, G. Troup, and R. Turner. "The use of a high intensity-range photographic film for recording extended diffraction patterns and for spectrographic work". In: *J.Sci.Instrum.* 42 (1965), pp. 116–117 (cit. on p. 66).

[148] G. Le Gray. URL: `http://www.getty.edu/art/exhibitions/le_gray/` (cit. on p. 66).

[149] W. Gerlach and O. Stern. "Der experimentelle Nachweis der Richtungsquantelung im Magnetfeld". In: *Zeitschrift für Physik* **9**.1 (1922), pp. 349–352. DOI: `10.1007/BF01326983` (cit. on p. 68).

[150] L. Chomaz et al. "Quantum-Fluctuation-Driven Crossover from a Dilute Bose-Einstein Condensate to a Macrodroplet in a Dipolar Quantum Fluid". In: *Phys. Rev. X* **6**.4 (2016), p. 041039. DOI: `10.1103/PhysRevX.6.041039` (cit. on p. 76).

[151] C. R. Cabrera et al. "Quantum liquid droplets in a mixture of Bose-Einstein condensates". In: *Science* **359**.6373 (2018), pp. 301–304. DOI: `10.1126/science.aao5686` (cit. on p. 76).

[152] G. Semeghini et al. "Self-Bound Quantum Droplets of Atomic Mixtures in Free Space". In: *Phys. Rev. Lett.* **120**.23 (2018), p. 235301. DOI: `10.1103/PhysRevLett.120.235301` (cit. on p. 76).

[153] T. Yefsah et al. "Exploring the Thermodynamics of a Two-Dimensional Bose Gas". In: *Phys. Rev. Lett.* **107**.13 (2011), p. 130401. DOI: `10.1103/PhysRevLett.107.130401` (cit. on p. 77).

[154] R. Desbuquois et al. "Determination of Scale-Invariant Equations of State without Fitting Parameters: Application to the Two-Dimensional Bose Gas Across the Berezinskii-Kosterlitz-Thouless Transition". In: *Phys. Rev. Lett.* **113**.2 (2014). DOI: `10.1103/PhysRevLett.113.020404` (cit. on p. 77).

[155] R. Meppelink et al. "Thermodynamics of Bose-Einstein-condensed clouds using phase-contrast imaging". In: *Phys. Rev. A* **81**.5 (2010), p. 053632. DOI: `10.1103/PhysRevA.81.053632` (cit. on p. 77).

[156] N. Navon et al. "Dynamics and Thermodynamics of the Low-Temperature Strongly Interacting Bose Gas". In: *Phys. Rev. Lett.* **107**.13 (2011), p. 135301. DOI: `10.1103/PhysRevLett.107.135301` (cit. on p. 77).

[157] M. J. H. Ku et al. “Revealing the Superfluid Lambda Transition in the Universal Thermodynamics of a Unitary Fermi Gas”. In: *Science* **335**.6068 (2012), pp. 563–567. DOI: `10.1126/science.1214987` (cit. on pp. 77, 82, 88, 89).

[158] D. J. Papoular et al. “Increasing Quantum Degeneracy by Heating a Superfluid”. In: *Phys. Rev. Lett.* **109**.8 (2012), p. 084501. DOI: `10.1103/PhysRevLett.109.084501` (cit. on pp. 78, 88).

[159] C.-H. Cheng and S.-K. Yip. “Trapped resonant fermions above the superfluid transition temperature”. In: *Phys. Rev. B* **75**.1 (2007), p. 014526. DOI: `10.1103/PhysRevB.75.014526` (cit. on p. 80).

[160] T.-L. Ho and Q. Zhou. “Obtaining the phase diagram and thermodynamic quantities of bulk systems from the densities of trapped gases”. In: *Nature Physics* **6**.2 (2010), pp. 131–134. DOI: `10.1038/nphys1477` (cit. on pp. 80, 81).

[161] S. Nascimbène et al. “Exploring the thermodynamics of a universal Fermi gas”. In: *Nature* **463**.7284 (2010), pp. 1057–1060. DOI: `10.1038/nature08814` (cit. on p. 80).

[162] N. Navon et al. “The Equation of State of a Low-Temperature Fermi Gas with Tunable Interactions”. In: *Science* **328**.5979 (2010), pp. 729–732. DOI: `10.1126/science.1187582` (cit. on p. 80).

[163] F. Chevy et al. “Thermodynamics of the unitary Fermi gas”. In: *Journal of Physics: Conference Series* **264** (2011), p. 012012. DOI: `10.1088/1742-6596/264/1/012012` (cit. on p. 80).

[164] P. Perrot. *A to Z of thermodynamics.* Oxford University Press, 1998 (cit. on p. 80).

[165] D. D. Hickstein et al. “A direct comparison of high-speed methods for the numerical Abel transform”. In: *Review of Scientific Instruments* **90**.6 (2019), p. 065115. DOI: `10.1063/1.5092635` (cit. on pp. 82, 83).

[166] N. Abel. “Auflösung einer mechanischen Aufgabe.” ger. In: *Journal für die reine und angewandte Mathematik* **1** (1826), pp. 153–157. URL: `http://eudml.org/doc/183021` (cit. on p. 82).

[167] L. Montgomery Smith, D. R. Keefer, and S. Sudharsanan. “Abel inversion using transform techniques”. In: *Journal of Quantitative Spectroscopy and Radiative Transfer* **39**.5 (1988), pp. 367–373. DOI: `https://doi.org/10.1016/0022-4073(88)90101-X` (cit. on p. 82).

[168] S. Gibson et al. *PyAbel/PyAbel: v0.8.3.* Version v0.8.3. 2019. DOI: `10.5281/zenodo.3370021` (cit. on pp. 82, 83).

[169] D. W. Chandler and P. L. Houston. “Two-dimensional imaging of state-selected photodissociation products detected by multiphoton ionization”. In: *The Journal of Chemical Physics* **87**.2 (1987), pp. 1445–1447. DOI: `10.1063/1.453276` (cit. on p. 82).

[170] C. Bordas et al. “Photoelectron imaging spectrometry: Principle and inversion method”. In: *Review of Scientific Instruments* **67**.6 (1996), pp. 2257–2268. DOI: `10.1063/1.1147044` (cit. on p. 82).

[171] J. Glasser, J. Chapelle, and J. C. Boettner. "Abel inversion applied to plasma spectroscopy: a new interactive method". In: *Appl. Opt.* **17**.23 (1978), pp. 3750–3754. DOI: 10.1364/AO.17.003750 (cit. on p. 82).

[172] R. K. Paul. "Novel approach to Abel inversion". In: *Review of Scientific Instruments* **78**.9 (2007), p. 093701. DOI: 10.1063/1.2777159 (cit. on p. 82).

[173] D. R. Snelling et al. "Two-dimensional imaging of soot volume fraction in laminar diffusion flames". In: *Appl. Opt.* **38**.12 (1999), pp. 2478–2485. DOI: 10.1364/AO.38.002478 (cit. on p. 82).

[174] J. A. H. Dreyer et al. "Improved methodology for performing the inverse Abel transform of flame images for color ratio pyrometry". In: *Appl. Opt.* **58**.10 (2019), pp. 2662–2670. DOI: 10.1364/AO.58.002662 (cit. on p. 82).

[175] G. R. Gladstone et al. "The atmosphere of Pluto as observed by New Horizons". In: *Science* **351**.6279 (2016), aad8866. DOI: 10.1126/science.aad8866 (cit. on p. 82).

[176] B. Hubert et al. "Analytic and numerical methods for the Abel transform of exponential functions for planetary and cometary atmospheres". In: *Icarus* **371** (2022), p. 114654. DOI: https://doi.org/10.1016/j.icarus.2021.114654 (cit. on p. 82).

[177] Y. Shin et al. "Observation of Phase Separation in a Strongly Interacting Imbalanced Fermi Gas". In: *Phys. Rev. Lett.* **97**.3 (2006), p. 030401. DOI: 10.1103/PhysRevLett.97.030401 (cit. on p. 82).

[178] Y. Shin et al. "Phase diagram of a two-component Fermi gas with resonant interactions". In: *Nature* **451**.7179 (2008), pp. 689–693. DOI: 10.1038/nature06473 (cit. on p. 82).

[179] J. A. P. Glidden et al. "Bidirectional dynamic scaling in an isolated Bose gas far from equilibrium". In: *Nature Physics* **17**.4 (2021), pp. 457–461. DOI: 10.1038/s41567-020-01114-x (cit. on pp. 82, 110).

[180] P. Holoborodko. *Smooth Noise Robust Differentiators.* 2008. URL: http://www.holoborodko.com/pavel/numerical-methods/numerical-derivative/smooth-low-noise-differentiators/ (cit. on p. 83).

[181] E. W. Hansen and P.-L. Law. "Recursive methods for computing the Abel transform and its inverse". In: *J. Opt. Soc. Am. A* **2**.4 (1985), pp. 510–520. DOI: 10.1364/JOSAA.2.000510 (cit. on p. 83).

[182] F. Dalfovo, L. Pitaevskii, and S. Stringari. "Order parameter at the boundary of a trapped Bose gas". In: *Phys. Rev. A* **54**.5 (1996), pp. 4213–4217. DOI: 10.1103/PhysRevA.54.4213 (cit. on p. 87).

[183] I. Reyes-Ayala et al. "Critical properties of weakly interacting Bose gases as modified by a harmonic confinement". In: *Journal of Statistical Mechanics: Theory and Experiment* **2017**.7 (2017), p. 073101. DOI: 10.1088/1742-5468/aa728a (cit. on p. 88).

[184] M. Ota and S. Giorgini. "Thermodynamics of dilute Bose gases: Beyond mean-field theory for binary mixtures of Bose-Einstein condensates". In: *Phys. Rev. A* **102**.6 (2020), p. 063303. DOI: 10.1103/PhysRevA.102.063303 (cit. on p. 91).

[185] D. H. DeVorkin. “Steps toward the Hertsprung–Russell Diagram”. In: *Physics Today* **31**.3 (1978), pp. 32–39. DOI: `10.1063/1.2994966` (cit. on p. 98).

[186] J. Szczepkowski et al. “Analysis and calibration of absorptive images of Bose–Einstein condensate at nonzero temperatures”. In: *Review of Scientific Instruments* **80**.5 (2009), p. 053103. DOI: `10.1063/1.3125051` (cit. on p. 98).

[187] C. W. Gardiner et al. “Kinetics of Bose-Einstein Condensation in a Trap”. In: *Phys. Rev. Lett.* **79**.10 (1997), pp. 1793–1796. DOI: `10.1103/PhysRevLett.79.1793` (cit. on p. 102).

[188] A. Imambekov et al. “Density ripples in expanding low-dimensional gases as a probe of correlations”. In: *Phys. Rev. A* **80**.3 (2009), p. 033604. DOI: `10.1103/PhysRevA.80.033604` (cit. on pp. 105, 106).

[189] N. Fabbri et al. “Momentum-resolved study of an array of one-dimensional strongly phase-fluctuating Bose gases”. In: *Phys. Rev. A* **83**.3 (2011), p. 031604. DOI: `10.1103/PhysRevA.83.031604` (cit. on pp. 105, 106).

[190] S. Richard et al. “Momentum Spectroscopy of 1D Phase Fluctuations in Bose-Einstein Condensates”. In: *Phys. Rev. Lett.* **91**.1 (2003), p. 010405. DOI: `10.1103/PhysRevLett.91.010405` (cit. on pp. 105, 110).

[191] N. G. Parker et al. “Quantum Turbulence in Atomic Bose-Einstein Condensates”. In: *Universal Themes of Bose-Einstein Condensation*. Ed. by N. P. Proukakis, D. W. Snoke, and P. B. Littlewood. Cambridge University Press, 2017, pp. 348–370. DOI: `10.1017/9781316084366.019` (cit. on p. 105).

[192] V. I. Yukalov, E. P. Yukalova, and V. S. Bagnato. “Nonlinear coherent modes of trapped Bose-Einstein condensates”. In: *Phys. Rev. A* **66**.4 (2002), p. 043602. DOI: `10.1103/PhysRevA.66.043602` (cit. on p. 105).

[193] N. G. Parker and C. S. Adams. “Emergence and Decay of Turbulence in Stirred Atomic Bose-Einstein Condensates”. In: *Phys. Rev. Lett.* **95**.14 (2005), p. 145301. DOI: `10.1103/PhysRevLett.95.145301` (cit. on p. 105).

[194] T. W. Neely et al. “Characteristics of Two-Dimensional Quantum Turbulence in a Compressible Superfluid”. In: *Phys. Rev. Lett.* **111**.23 (2013), p. 235301. DOI: `10.1103/PhysRevLett.111.235301` (cit. on p. 105).

[195] W. J. Kwon et al. “Relaxation of superfluid turbulence in highly oblate Bose-Einstein condensates”. In: *Phys. Rev. A* **90**.6 (2014), p. 063627. DOI: `10.1103/PhysRevA.90.063627` (cit. on p. 105).

[196] N. Navon et al. “Emergence of a turbulent cascade in a quantum gas”. In: *Nature* **539**.7627 (2016), pp. 72–75. DOI: `10.1038/nature20114` (cit. on p. 105).

[197] M. C. Tsatsos et al. “Quantum turbulence in trapped atomic Bose-Einstein condensates”. In: *Physics Reports* **622** (2016), pp. 1–52. DOI: `https://doi.org/10.1016/j.physrep.2016.02.003` (cit. on p. 105).

[198] A. J. Groszek et al. “Onsager vortex formation in Bose-Einstein condensates in two-dimensional power-law traps”. In: *Phys. Rev. A* **93**.4 (2016), p. 043614. DOI: `10.1103/PhysRevA.93.043614` (cit. on p. 105).

[199] M. J. H. Ku et al. “Motion of a Solitonic Vortex in the BEC-BCS Crossover”. In: *Phys. Rev. Lett.* **113**.6 (2014), p. 065301. DOI: `10.1103/PhysRevLett.113.065301` (cit. on p. 105).

[200] M. Tylutki et al. “Solitonic vortices in Bose–Einstein condensates”. In: *The European Physical Journal Special Topics* **224**.3 (2015), pp. 577–583. DOI: `10.1140/epjst/e2015-02389-7` (cit. on p. 105).